Università degli Studi di Milano - Bicocca
Facoltà di Scienze Matematiche, Fisiche e Naturali
Corso di Dottorato di Ricerca in Scienza dei Materiali
XXII ciclo

Oxide ultra–thin films on metals

A.A. 2008/2009

Ph.D. dissertation
Umberto Martinez Pozzoni

Supervisor
Prof. Gianfranco Pacchioni

Contents

Acknowledgements

I would like to thank my supervisor Prof. Gianfranco Pacchioni for the guide, the support and for giving me the possibility to perform part of my Ph.D. experience abroad and to collaborate directly with many other groups in Europe. Thanks to Dr. Livia Giordano, for supporting and following me in this experience from the beginning.
The work presented in this thesis is largely based on a collaborative effort with the Department of Chemical Physics of the Fritz–Haber Institut (FHI) der Max Planck Gesellschaft directed by Prof. Hans–Joachim Freund. Some of the results presented and discussed in the chapters of the thesis have been obtained in the groups of Dr. Martin Sterrer, Dr. Thomas Risse, Dr. Markus Heyde and Dr. Shamil Shaikhutdinov at the FHI and I am grateful to them for this. I would also like to thank in particular Dr. Niklas Nilius and his group, again at the FHI in Berlin, for all the stimulating discussions and the support during my visit at his laboratories. Our joint work on ultra–thin oxide films has resulted in a number of research papers on which parts of this thesis are based.
During my Ph.D. I also had the opportunity to collaborate directly with other theoretical groups in Europe.
I am indebted to Prof. Francesc Illas at the Department of Physical Chemistry of the Universitat de Barcelona for the support during my stay in Barcelona and for the fruitful collaboration. I also wish to thank Prof. Konstantin Neyman and Prof. Ste-

fan Bromley for all the scientific discussions we had during my visit and the other members of the group for the beautiful experience.
In a similar way I want to thank Prof. Alex Shluger and Dr. Matthew Watkins at the University College London for the work performed together on the nature of the defects on the MgO films.
Many thank to all members (or ex–members) of my research group for the scientific and non–scientific discussions and in particular to Dr. Cristiana Di Valentin, Dr. Sabrina Sicolo, Dr. Fabrizio Cinquini and Dr. Emanuele Finazzi.
I wish to thank Dr. Luca Maini for useful discussions and for the help that he gave me in the first part of my thesis trying to simulate STM images.
Last but not least, I wish to thank my family (three amazing women) and my friends for the constant support. This work wouldn't have been possible without the guide of one person, behind every day of these three years. Many thanks to Giada.

CHAPTER 1

Introduction

1.1 Thin oxide films as advanced materials

Insulating oxide films are widely applied in material science and have played a fundamental role in microelectronics,[1] electrical properties of oxide–semiconductor interfaces and are of significance in devices such as transistors.[2] As reported in the next section, oxide films are of fundamental importance in strucural applications and the use of stainless steels as structural materials is continuosly growing. Oxide films are also very important as support materials in heterogeneous catalysis where they are used to stabilize small metal particles as the chemically–active species.

When the insulating oxide film consists of just few atomic layers[3] it is possible to obtain a new class of systems with tunable properties and several potential and actual applications: magnetic tunnel junctions, dielectrics in miniaturized electronic devices, magnetic devices based on oxide nanostructures, plasma display panels,[4] modified supports for metal nanocatalysts, etc. For example, a thin oxide layer formed in between two ferromagnetic electrodes is a crucial part of a tunnel junction used in various electronic devices. In particular if the insulating layer is thin enough, tipically few atomic layers, electrons can tunnel through the insulating barrier into avaliable electron states on the ferromagnetic electrodes resulting

in electrical conduction. This effect is the basis of magnetic tunnel junctions (MTJ) developed in 1991[5] based on the giant magnetoreisstive (GMR) effect discovered in 1988.[6] Amorphous AlO_x and TiO_x based MTJs can be faricated by sputtering techniques. However, more recently MgO crystalline MTJ barriers of few nanometers have been employed, Figure 1.1.

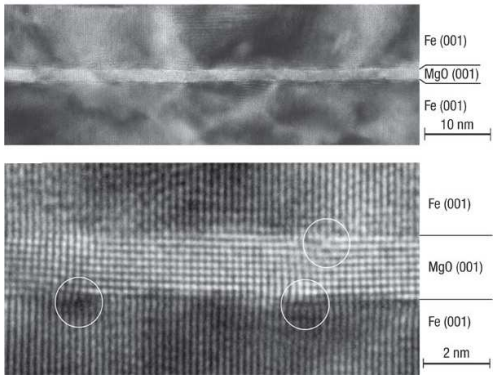

Figure 1.1: Cross–sectional trasmission electron microscope images of an epitaxial Fe(001)/MgO(001)(1.8nm)/Fe(001) magnetic tunnel junction. Reproduced from Ref.[7].

In the next two sections are described in details two important applications that present strong connection with the work of this thesis: thin films for corrosion protection (passive films) and new phenomena related to ultra–thin oxide films as model for cataysis.

1.2 Thin oxide films for corrosion protection: passive films

In this section we want to focus on the properties of thin oxide films that can be used for protection from the corrosion of metals and steels. This kind of films is of enormous technological significance, since the dissolution rate often determines the lifetime of structural materials.

Passivation of metals results from the formation of a condensed phase of continuous oxide layer on the metal surface. The electrochemical stability of passivated metals depends not only on the chemical property but also on the electronic property of the passive films.

In Table 1.1 are reported some important properties of selected oxide passive films that are in the range of 1 to 6 nm thick.

Table 1.1: Typical data for thin passive films:[8] band gap energy E_g, dielectric permettivity ϵ, donor concentration N, initial oxide thickness d_0.

Metal	Oxide	E_g (eV)	ϵ	N (cm^{-3})	d_0 (nm)
Al	Al_2O_3	7–9.5	7.5–15		2–4.3
Be	BeO		16–120		0.65
Fe	Fe_2O_3/Fe_3O_4	1.9		10^{20}	
Mo	MoO_3				3.1
Ta	Ta_2O_5	4–4.6	12–27		1–2
Ti	TiO_2	3.2–3.8	7–114	10^{20}	1.3–5.4

A particular class of materials with an excellent resistance in a large number of atmospheres is that of stainless steels, also very important as a structural materials. Indeed, the high corrosion resistance of stainless steels is due to the phenomenon of passivity. In this case the passive film also has the advantage, compared for example to paint layer, to be self–healing. Mechanical or chemical damage to the passive film will repassivate in oxidising environments.

1.2.1 Formation of passive films

Metals dissolve by active corrosion in many solutions. They become "passive" if they substantially resist corrosion under conditions where the bare metal would react significantly. When a metal is exposed to a solution or air the difference in red/ox potential of the two phases in contacts leads to a driving force for metal oxidation. The enviromental conditions then can either favor dissolution of the oxidized metal cation (active corrosion) or the formation of a second phase film (passivation) according to:

$$\mathrm{x\,M} \quad + \quad \mathrm{y/2\,O_2} \quad \longrightarrow \quad \mathrm{M_xO_y} \tag{1.1}$$

Figure 1.2 represents the growth of an oxide film under open–circuit condition. The anodic current density may be supplied from an outer circuit or is compensated by cathodic currents like hydrogen evolution or oxygen reduction at open circuit conditions.

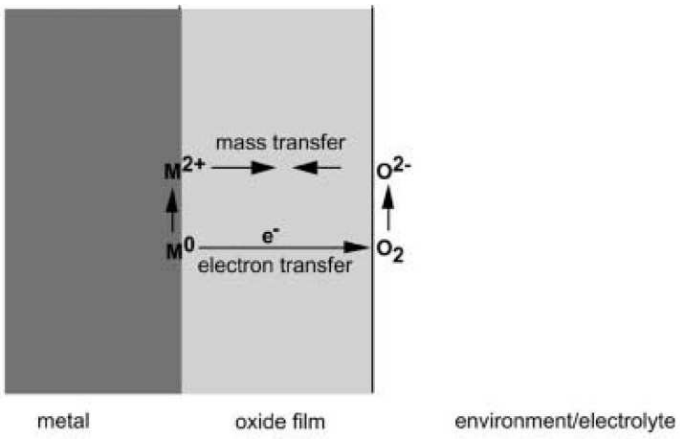

Figure 1.2: Growth of an oxide film on a metal surface. Reproduced from Ref.[9].

Passivation is best illustrated by a tipical polarization curve, Figure 1.3, where a dramatic decrease in current at a particular onset potential occurs. On increasing the voltage the current at first increases more or less exponentially in the active region, where the predominant reaction is metal dissolution. The passivation potential is reached when a thin oxide film forms and prevents further dissolution. The current decreases to a plateau that defines the passive state. At still higher voltages, the current again increases due to oxygen evolution.

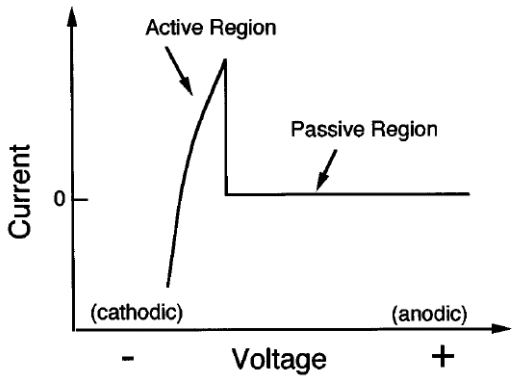

Figure 1.3: Tipical anodic polarization curve for a metal elecrode exhibiting passivation at a distinct anodic potential. Reproduced from Ref.[10].

Numerous attempts to model film growth based on different concepts have been made and are summarized in Ref.[11]. In particular, here we want to cite the Cabrera and Mott model[12] because this theory is valid also for thin passive films and can be applied to some of the new phenomena described in the thesis (see in particular Part I).

Since the two steps of the reaction 1.1 (oxidation and reduction) are separated, either oxygen or metal atoms have to migrate through the oxide layer (Figure 1.2). The initial reaction rates observed at low temperatures are too fast to be activated by the slow diffusion of the two species. An explenation of this phenomenon has been given by Cabrera and Mott.[12] According to this model, for a thin oxide film, electrons tunnel from the metal to an adsorbed oxygen atom through the dielectric film in order to equalize the electrochemical potential. The positive surface charge on the metal and a negative one from excess of oxygen ions create an electric field across the oxide film, which leads to a shift in the Fermi level of the oxide (Figure 1.4). The potential E_b (the so called Mott potential) formed across the oxide is responsible for field–assisted diffusion of the ionic species across the oxide films so that a thin films can grow even at ambient or low temperature. The electrons are assumed to pass through the film via tunneling restricting the model to very thin films, less than 3 nm. For thicker films the transport of electron by thermionic emission (of electron via the conduction band, or holes via the valence band) has to be considered.[14]

Because of the simplicity of the Cabrera and Mott model, it is possible to find discrepancies between theory and experiment, in particular for prolonged oxidation process. For example the model does not take into consideration the current tunnel attenuation in the thickening oxide, is insensitive to the parameters of the oxidative enviromental and other number of processes. Different models have been later developed which improve the Cabrera and Mott description in order to predict the physical properties of the oxide films grown.[14–16] For example Martin *et. al.*[16] suggest a model of low–temperature oxidation of the metal surface based on Cabrera and Mott theory (tunneling of electrons from the metal to the oxide surface). In this case O_2^- ions are the charged particles at the interface between oxide and gas, and interstitial ions are the migrating defects. Depending on the type of migrating defects (metal interstitial or oxygen interstitial), the reaction front lies either at the interface between gas and oxide or at the interface between oxide and metal according to the picture in Figure 1.5.

In any case, the main point remains the field–assisted diffusion process of the species involved by the potential due to the tunneling of the electrons from the metal

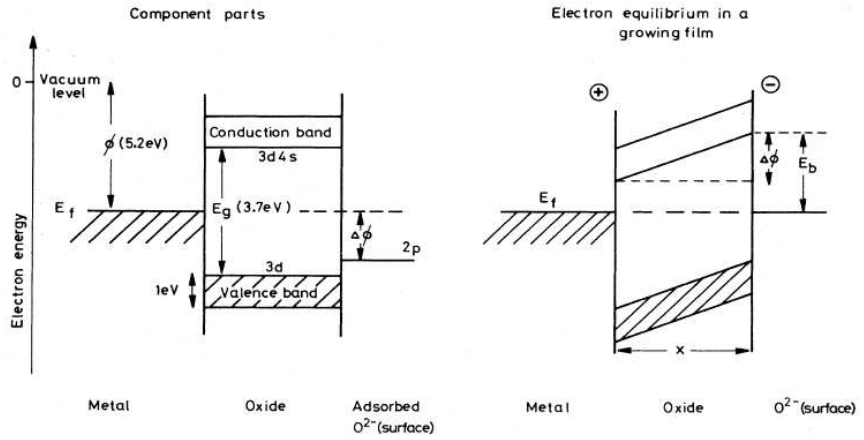

Figure 1.4: Electron energy–level diagrams illustrating how the transfer of electrons from the metal to the oxygen adsorbed on the surface of a thin, growing oxide film generates a uniform electric field. The energy and band level are for Ni and NiO. Reproduced from Ref.[13].

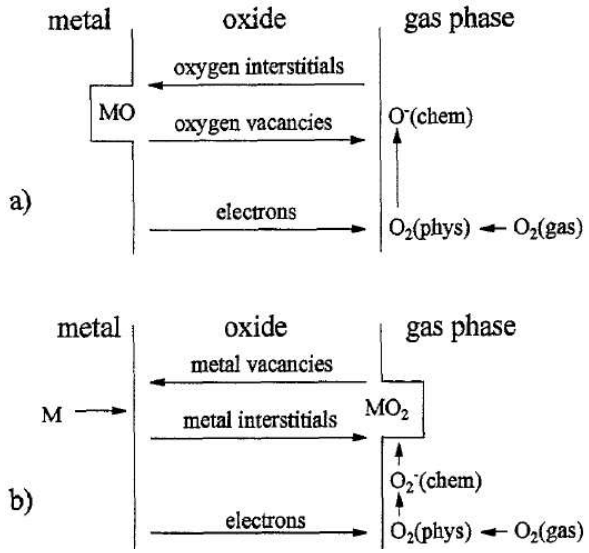

Figure 1.5: The two different mechanisms of oxide film growth according to the model described in Ref.[16]. (a) transport of oxygen ions or vacancies, reaction front at the metal–oxide interface. (b) transport of the metal ions or vacancies, reaction front at the oxide surface.

to the adsorbed species. The presence of Mott potential was established experimentally by Papova *et. al.* in 2002.[10] The experiment has shown that irradiating with electrons an aluminum oxide film on Al(111), surface charging occurs. This negative electrostatic charge at the surface of the Al_2O_3 thin film induces an electric field ($\sim 10^7$ V/cm) across the film. The oxidation rate an 90 K increases dramatically due to the increased Mott potential that enhances the ion diffusion process, the rate limiting step of the Al oxidation process, as predicted by the Cabrera and Mott theory.

1.2.2 Structure and composition

The structure and the composition of the passive films are vital parameters that influence the corrosion resistance. There are several techniques that one can use in order to study the structure of passive films. Especially for thick oxide films the structure can be accessed by X–ray diffraction techniques, optical microscopy, atomic force microscopy (AFM), or laserprofilometry.

The situation is different and more difficult for ultra–thin passive films formed at low temperatures. Moreover, one main problem of ex situ measurement is whether the structre of a thin film may change after removal from the electrolyte, or in general from the electrochemical condition under which it was formed. In particular the film may have been altered through crystallization and/or removal of OH groups. Therefore, new in situ techniques have been developed in the last years to study the structure of ultra–thin passive films. For example scanning tanneling microscopy,[17] X–ray scattering[18] also using synchrotron radiation and extended X–ray adsorption fine structure (EXAFS).[19]

With these techniques is possible to establish if the passive film is amorphous or crystalline. As discussed below, the degree of crystallinity is of fundamental importance for the electron properties of the passive films and so for the corrosion resistance. Many oxide films show an increase of oxidation state from metal to the electrolyte[20] and are usually non-stoichiometric due to an excess of metal ions or a deficiency of oxygen ions. In general the passive film forms a bilayer structure consisting of a defective oxide (also called barrier layer) at the metal interface and an outer layer that forms from the reaction of metal cations with species in the solution.[21]

Besides these aspects one have also to consider the so–called “aging” process of passive films. This results in a change of the properties of the passive film, such as composition and structure, with time. As a consequence, film stability or corro-

sion resistance will change during long term application of the material. Therefore, film aging is of great practical interest, in particular for structural materials. This phenomena however have been much less investigated mostly because of the complexity of the mechanism and the extended time scales involved.

1.2.3 Electronic properties

Electron transfer through the passive film can be a crucial point for corrosion resistance of a metal. Oxide passive films can be metallic (IrO_2, RuO_2, PbO_2), semiconductors (oxides on Ti, Fe or Ni) or insulators (oxide on Si, Al or Ta). Most of the electronic properties can be derived from photocurrent and capacitance mesaurements. As reported above, passive films are likely to be highly defective. Defect concentrations are usually in the range of 10^{19} to 10^{21} cm^{-3} and, if the film presents insulator properties, defects can bring to localized states in the gap. Reducing the number of localized electronic states is expected to improve the resistance to corrosion.[22]

In Figure 1.6 is reported a schematic diagram that correlates the electronic structure with the crystal structure of a passive film. In Figure 1.6a is reported the situation for a typical crystalline n–type or p–type semicondutive thin film. In case of amorphous oxide films the band gap has to be substitued by the mobility gap E_m[23] accompanied with a tail of localized states into the gap, Figure 1.6b. Finally, interstitials, vacancies and surface states yeld well defined and localized states in the band gap, Figure 1.6c.

We also have to consider the thickness of the passive oxide film. In fact the band structure of ultra–thin oxide films can be very different with respect to the corresponding ideal thick film or bulk surfaces. In general a smaller band gap is observed due to the lower dimensionality of the system.

1.2.4 Breakdown

The passive state of the metal is susceptible to various forms of localized corrosion, including pitting corrosion, stress corrosion cracking, corrosion fatigue, and crevice corrosion. An initial breakdown of the passivity, in which the oxide film is ruptured and the underlying metal is exposed to the enviromental is necessary in order to initialize one of the breakdown phenomena listed above. The reason of this local destruction may be due to a dielectric breakdown (the oxide lattice cannot

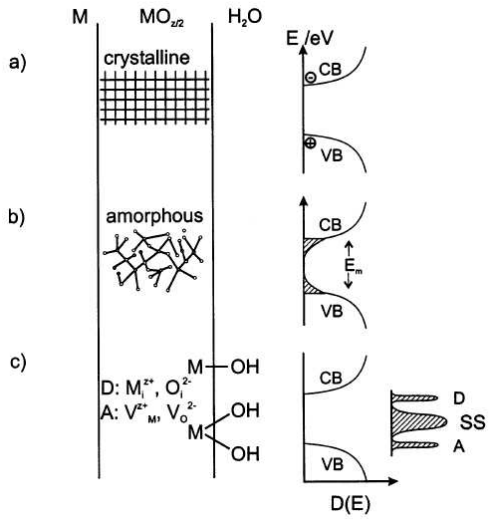

Figure 1.6: Schematic diagram of crystal structures and electronic states in the oxide film. Reproduced from Ref.[8].

withstand the high field strength) or to aggressive halogen ions, like chloride, that may penetrate into the films. In an electrochemical polarizaion experiment (Figure 1.3) the onset of localized dissolution can be detected by a steep current increase at a distinct anodic potential.

Different theories and models have been proposed for passivity breakdown.[24–26] It is interesting to cite the Point Defect Model (PDM)[24] because consider vacancy condensation at the metal interface. Vacancy segregation at the metal/oxide interface or in general at line defects, such as steps and kinks, is an important process that can have consequences also in other fields (see next Section and Chapter 8). In the PDM passivity breakdown occurs as a results of cation vacancy condensation at the metal oxide interface at sites in the passive films that are characterized by high cation vacancy flux (grain boundaries, dislocations, inclusions, ...). According to the PDM the processes that are involved in passivity breakdown are shown in Figure 1.7.

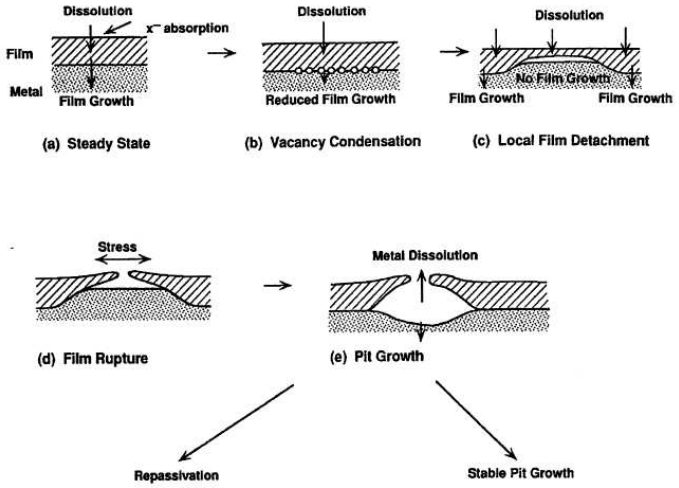

Figure 1.7: The figure shows different stages of pit nucleation according to the Point Defect Model. Reproduced from Ref.[11].

1.3 Thin oxide films as model of supported catalysis: new phenomena

Oxide surfaces are of fundamental importance in heterogeneous catalysis as active catalysts and as support for metal clusters. Oxide films grown on metal substrates have been initially used because as opposed to oxide single crystals rely on the electrical conductivity of the samples allowing the use of different surface science techniques. These particualr systems offer some advantages typically found for single oxide crystals and have been shown to mimic chemical and physycal properties of the coresponding bulk oxides.

However if the oxide film is thin enough (just very few atomic layers) a completely different system may be found showing different properties from the correspondent thick film or bulk material. These systems are a new class of materials whose properties are determined by the combination of properties of the film together with those of their support. In particular ultrathin oxide films show a large number of parameters that is possible to modify in order to have the desired behaviour. A key aspect of the elucidation of the film properties is the detailed knowledge of the film structure and morphology.

Different reviews about the preparation and the properties on ultrathin oxide

films are published,[27–33] this section focuses on recent results of some of the new effects observed on well ordered ultrathin oxide films.

1.3.1 Charge transfer effects

Having ultimate control, as available today, over the thickness and structure of the oxide films, the new properties of ultrathin oxide films may be used to control the charge state and, thus, the catalytic properties of a metal deposited onto them, an idea related to those proposed by Cabrera and Mott in connection with metal oxidation, see section 1.2.1 pag. 3.

Particular sites of a thin oxide film support can provide means to alter the properties of deposited metals. DFT calculations have shown a strong binding of gold atoms and dimers at defects with the highest binding energies found for gold on singly charged (F^+) and neutral (F^0) color centers,[34] and has been proposed the mechanism of a charge tranfer from the defect site to the gold adsorbates. Diamagnetic F centers and paramagnetic F^+ centers can be generated by electron bombardment preferentially at low–coordinated sites, such as steps or edges,[35,36] where the cost of creating an oxygen vacancy is lower, as predicted by theory.[37,38] Scanning tunneling spectroscopy measurements have demonstrated that F centers create energy levels within the band gap of MgO.[36] An additional level of complexity is introduced by the fact that the thin oxide film is deposited onto a metal substrate.

The importance of such binding mechanism has been pointed out by a combined experimental and theoretical investigation of gold clusters on MgO surfaces that shows the catalytic properties of deposited Au clusters,[39] Figure 1.8. The correlation between the presence of color centers and the nucleation of Au has been directly proven and verified by a combination of electron paramagnetic resonance (EPR) and scanning tunneling microscopy.[40]

Charghing of adsorbed metals must not necesarily involve the presence of defects on the oxide surface. One very interesting phenomena that can occur is the charge transfer of one electron from the metal substrate directly to an adsorbed species (atoms, clusters or even molecueles). On the basis of density functional theory (DFT) calculations it was proposed that charge transfer may occur provided that the adsorbate exhibits a high electron affinity and the film thickness does not exceed a few monolayers.[41–43] In particular, Au atoms adsorbed on a thin MgO film grown on Mo(100) and Ag(100) are expected to be negatively charged in contrast to their counterparts on bulk MgO (or thick MgO films), which were proven to be

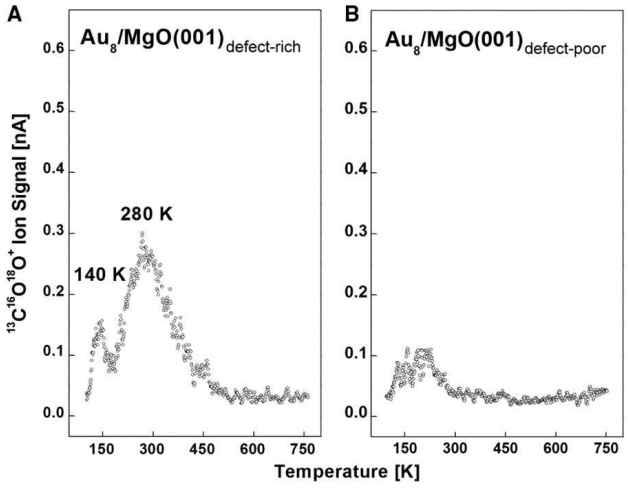

Figure 1.8: Mass spectrometric signals pertaining to the formation of CO_2 on Au_8 clusters deposited on (a) defect–poor and (b) defect–rich MgO(100) films. Reproduced from Ref.[39].

essentially neutral.[44] The evidence of the transfer of one electron from the metal to the adsorbed gold atom is given inside the thesis (Chapter 3) where a series of observable evidences for the formations of Au^- species are discussed.

An interesting consequence of the spontaneous charge transfer is the possibility to change the properties of adsorbed particles on ultrathin films with respect to that on bulk surface or on thicker film. In fact increaring the thickness of the film a behavior more similar to that of a bulk oxide surface is expected, typically around 10 ML. This effect has been studied both theoretically[42] and experimentally.[45] In particular an increase in binding energy was found for clusters deposited on MgO films of thickness up to about 1 nm, or 4 to 5 MgO layers, originating from the metal-induced excess electronic charge accumulated at the cluster interface with the oxide film.[42] The charge localized at the oxide–metal interface strongly reinforces the Au–O interaction favoring a dimensionality crossover from three–dimensional optimal cluster geometries on MgO(100) to two–dimensional structures.

The effect has been also observed experimentally.[45] The STM images of gold particles deposited on an ultrathin (3 ML) and on a thicker (8 ML) MgO film on Ag(100) clearly show two different growing regimes. On the 3 ML film extended 2D gold islands are formed, whereas 3D Au particles appear on the 8 ML films,

Figure 1.9.

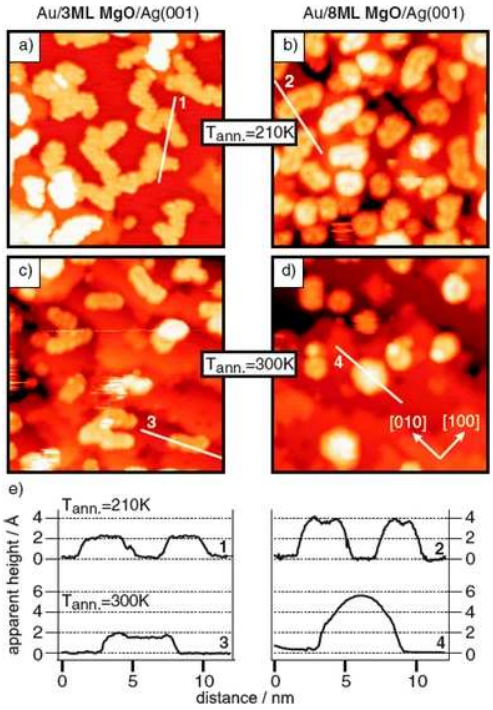

Figure 1.9: STM images of Au clusters formed after annealing Au atoms deposited on 3 ML and 8 ML thin MgO films, respectively to T=210 K (a-b) and T=300 K (c-d). (e) Height profiles of the Au clusters marked with a solid line. Reproduced from Ref.[45].

Ultrathin oxide films are thus unique systems whose properties can be tailored in a desired way. The occurrence or not of a spontaneous charging strongly depends several parameters which can be in principle modified: the oxide material (ionic or covalent, reducible or non-reducible, etc.), the nature of metal/oxide interface (strong or weak adhesion, lattice mismatch, position of metal Fermi level with respect to valence and conduction band of the oxide, charge transfer at the interface, etc.), or the thickness of the oxide film (from one to several ML). One important and essential aspect that comprises several of these factors is the work function of the metal/oxide interface. The understanding of the mechanism involved is crucial to know how the properties of ultrathin films can be tuned.

1.3.2 Work function change

An important consequence of the deposition of a thin insulating film on a metal substrate is the induced change in work function of the metal support which can be lowered or increased depending on the nature of the interface. For example, modulation of the work function of a FeO/Pt(111) film provides the basis for using these supports to induce spatial ordering and self–assembling of supported nanoparticles.[46]

The model proposed by Schottky[47] states that when a metal and a dielectric are combined, there is no charge transfer across the interface and the Schottky barrier height is given by the difference between the work function of the metal and the top of valence band of the dielectric. However, the Schottky model is not generally obeyed. In fact, the metal wave function decays into the dielectric in the energy range where the metal conduction band overlaps with the band gap of the insulator.[48] This gives rise to metal–induced gap states (MIGS)[49–52] which can be simply due to the spatial penetration of the tails of the metal wave function into the dielectric or to the formation of a true chemical bond at the interface.[53] These latter MIGS can have donorlike or acceptorlike character.

The presence of other states at the interface induces a charge transfer (CT) across the interface creating a dipole μ, which shifts the position of the metal Fermi energy E_F, Figure 1.10a. In particular, a dipole which corresponds to negative charge above the metal results in a work function increase, while a reverse dipole contributes to lower the work function. As a result, the effective work function of the metal/dielectric system differs from the work function of the pure metal.

Examples of changes in work function by deposition of thin insulating layers have been reported in the literature. Based on the Anderson method it has been found that a monolayer of Al_2O_3 grown on Mo(110) lowers the work function by 0.7 eV.[54] Kelvin probe force microscopy or scanning tunneling microscopy studies of alkali chloride thin films on Au(111) and Ag(100) have shown work function reductions of 0.5–1.2 eV.[55,56] A more recent work based on field–emission resonance has found for NaCl islands of up to 3 ML a work function reduction of 1.3 eV.[57] Sometimes, the lattice mismatch between the dielectric film and the metal results in the modulation of the surface potential and the local work function, a phenomenon which can be used to induce self–assembling of deposited metals atoms.[58] Theoretical calculations have predicted a reduction in Φ for NaCl and MgO on various metals.[53,56,59–62]

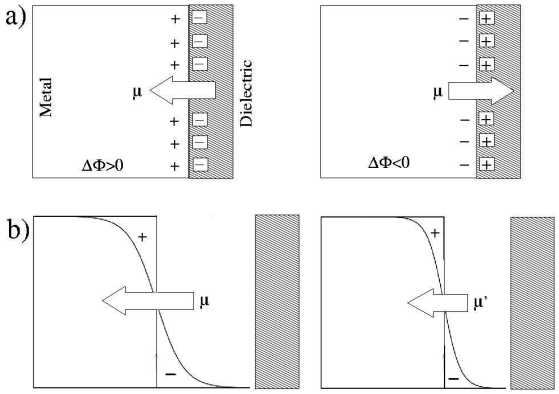

Figure 1.10: Schematic representation of the two major contributions to the change in work function induced by the deposition of an ultrathin dielectric layer on a metal support. (a) Charge transfer at the interface and (b) compressive electrostatic effect. Both terms lead to a change in surface dipole μ, and hence in metal work function.

However the work function change ($\Delta\Phi$) for a dielectric thin film on a metal cannot be explained only with the CT model. Recently, it has been shown that MgO/metal interfaces give rise to substantial changes in work function despite a relatively small almost negligible CT.[59,61] The effect has been attributed to the substrate–induced polarization of the metal electrons, a basically electrostatic mechanism which has been proposed also for adsorbates on metal surfaces.[59,63–65] In particular, a recent work has emphasized the role of the exchange (or Pauli) repulsion in determining work function changes induced by rare gases on metals.[66] The "rigid wall" represented by the dielectric top layer pushes the electronic charge that spills over from the metal surface back into the metal, thus changing the surface dipole even in the absence of charge transfer between the metal and the insulating film, Figure 1.10b. While the CT mechanism dominates the work function changes for films with strong chemical interaction with the metal, the electrostatic or compression effect is important for films of highly ionic materials (e.g., NaCl). However, the two terms can act together or can have different signs, thus leading to an additive or a canceling global effect, respectively. Furthermore, the final change in work function can be rather different for different metals even in the presence of the same dielectric.

The work funtion of an oxide/metal interface is a central quantity in this thesis

and a way to tune this property is reported in Part III.

1.3.3 Silica ultrathin films

The preparation of crystalline thin silica films was reported in 2000 by the group of Freund.[67–70] The procedure consists of repeated cycles of silicon deposition and subsequent oxidation, followed by a final annealing at temperature up to 1100–1250 K. Low energy electron diffraction (LEED) shows an hexagonal, crystalline SiO_2 overlayer of less than 10 Å thickness with a $c(2\times2)$ commensurate relationship to the Mo(112) substrate. In Figure 1.11 are reported high–resolution STM images and the LEED pattern of the silica film.

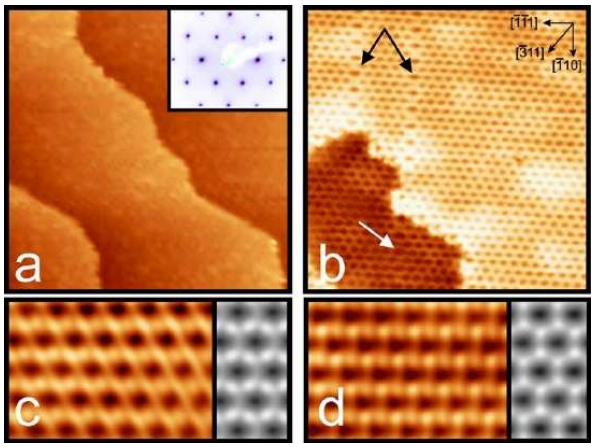

Figure 1.11: STM images of the crystalline silica ultrathin film growth on Mo(112) substrate. The inset in (a) shows the LEED pattern. In (b) the line defects along the [$\bar{1}$10] direction are indicated by arrows. (c–d) High resolution STM images. (a) 75×75 nm^2, V_s=2 V; (b) 14×14 nm^2, V_s=1.3 V; (c) 5×2.5 nm^2, V_s=0.65 V; (d) 5×2.5 nm^2, V_s=1.2 V. Reproduced from Ref.[71].

Numerous studies have been addressed to clarify the exact crystalline structure of the silica layer and different models have been proposed,[71–87] Figure 1.12. In particular. a model consisting of isolated SiO_4 clusters has been suggested by Chen and Goodman,[73,84] supported by the work of Yakovkin,[76] and a two–dimensional honeycomblike network of SiO_4 connected thetrahedra proposed by the groups of Freund[74,78] and Pacchioni.[75] Here we don't want to go into the details of the discussion and the reader can refer to the critical review on this topic reported in Ref.[88].

It has been now well established that the film consists of a monolayer of corner sharing SiO_4 tetrahedra as a two–dimensional network, with one corner oxygen bonded to the Mo atoms. In this context will be cited just the very recent and indipendent work of Seifert *et al.*[89,90] that again supports the 2D structural model. Besides, this thesis itself provides more and more evidences for this structure (see chapters 5, 6, 7, 9 , 10 and 11).

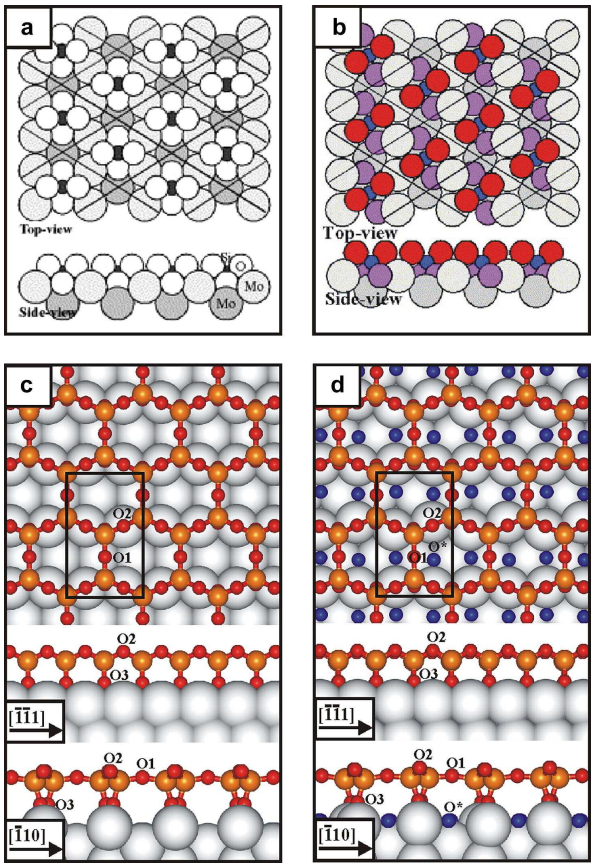

Figure 1.12: Different model proposed for the crystalline silica film on Mo(112). (a–b) Cluster models and (c–d) two–dimensional network models. Reproduced from Ref.[88].

The work of Seifert *et al.* is based on ion beam triangulation (IBT) method performed with fast hydrogen atoms scattered under a grazing angle of incidence from the thin film oxide surface. This technique gives informations on the geometrical ar-

rangement of the atoms in the topmost layer of the film and a direct comparison of the experimental results with classical trajectory computer simulations is possible. Comparing the simulations for the two structural models with the experimental angular distributions for scattered projectiles an almost perfect correspondence with the two–dimensional model has been found, see Figure 1.13.

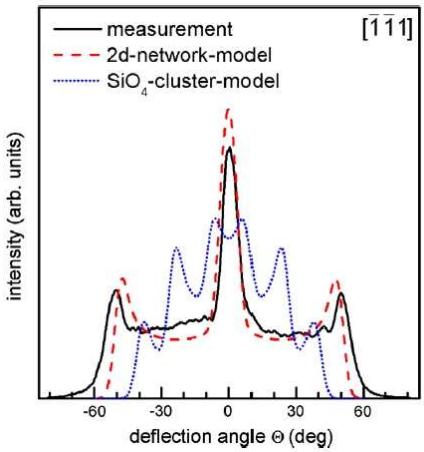

Figure 1.13: Comparison between experimental and simulated projected intensity distributions as a function of deflection angle along the $[\bar{1}\bar{1}1]$ direction. These results provide clear evidence in favor of the the two–dimensional silica model. Reproduced from Ref.[90].

At elevated oxygen pressures the calculations predict formation of a different structure of the 2D silica film.[78] In addition to the network of corner sharing tetrahedra this structure contains different oxygen atoms adsorbed directly on the Mo(112) metal surface, Figure 1.12d. This new phase that does not change the symmetry of the film has been also confimed by infrared reflection adsorption spectroscopy and X–ray photoelectron spectroscopy. This particular structure will be discussed in Chapter 6 providing additional results in favor of this model.

Finally, experimental high resolution STM images reveal surface dislocations in a form of antiphase domain boundaries (ADB), Figure 1.11. A first model of ADB has been reported in Ref.[71] and consists of a chain of interchanging octaedral and square rings containing 8 and 4 Si atoms respectively. This defects play a determinant role in the adsorption properties of the substrate as it will be described in Part II of the thesis.

Bibliography

[1] K.J. Bachmann, *The Materials Science of Microelectronics* (1995) VCH, New York.

[2] J. Robertson, *Rep. Prog. Phys.* **69** (2006), p. 327.

[3] S. Schintke, S. Messerli, M. Pivetta, F. Patthey, L. Libioulle, M. Stengel, A. De Vita, and W.–D. Schneider, *Phys. Rev. Lett.* **87** (2001), p. 276801.

[4] Y. Motoyama, H. Matsuzaki, and H. Murakami, *IEEE Trans. Electron Devices* **48** (2001), p. 1568.

[5] T. Miyazaki, T. Yaoi, and S. Ishio, *J. Magn. Magn. Mater* **98** (1991), p. L7.

[6] M.N. Baibich, J.M. Broto, A. Fert, F. Nguyen Van Dau, F. Petroff, P. Etienne, G. Creuzet, A. Friederich, and J. Chazelas *Phys. Rev. Lett.* **61** (1988), p. 2472.

[7] S. Yuasa, T. Nagahama, A. Fukushima, Y. Suzuki and K. Ando, *Nature Mater.* **3** (2004), p. 868.

[8] J. W. Schultze, M. M. Lohrengel, *Electrochim. Acta* **45** (2000), p. 2499.

[9] P. Schmuki, *J. Solid State Electrochem* **6** (2002), p. 145.

[10] I. Papova, V. Zhukov, J. T. Yates Jr., *PRL* **89** (2002), p. 276101.

[11] D. D. Macdonald, *Pure Appl. Chem.* **71** (1999), p. 951.

[12] N. Cabrera, N. F. Mott, *Report Progr. Phys.* **12** (1948), p. 163.

[13] A. Atkinson, *Reviews of Mod. Phys.* **57** (1985), p. 437.

[14] A. T. Fromhold, *Theory of Metal Oxidation – Volume I, Fundamentals* (North–Holland, Amsterdam), Vol. 9.

[15] V. P. Parkhutik, *J. Phys. D: Appl. Phys.* **25** (1992), p. 256.

[16] M Martin, E. Fromm, *J. of Alloids and Compounds* **258** (1997), p. 7.

[17] M. P. Ryan, R. C. Newmann, G. E. Thompson, *J. Electrochem. Soc.* **142** (1995), p. L177.

[18] M. F. Toney *et al*, *PRL* **79** (1997), p. 4282.

[19] J. Kruger, *Mater. Sci. Forum* **185–188** (1995), p. 367.

[20] M. M. Lohrengel, J. W. Schultze, H. D. Speckmann, H.–H. Strehblow, *Electrochim. Acta* **32** (1987), p. 733.

[21] D. D. Macdonald, *J. Electrochem. Soc.* **139** (1992), p. 3434.

[22] I. Serebrennikova, H. S. White, *Electrochem. Solid–State Lett.* **4** (2001), p. B4.

[23] N. F. Mott, E. A. Davis, *Electronic process in non-crystalline Solids* (1979), Clarendon, Oxford.

[24] L.–F. Lin, C.–Y. Cheo, D. D. Macdonald, *J. Electrochem Soc.* **128** (1981), p. 1194.

[25] G. S. Frankel, *J. Electrochem Soc.* **145** (1998), p. 2186.

[26] M. Fromont, ed. *Passivity of Metals and Semicondutors.* Elsevier, Amsterdam (1983).

[27] D.W. Goodman, *J. Ohys. Chem.* **100** (1996), p. 13090.

[28] C. R. Henry, *Surf. Sci. Rep.* **31** (1998), p. 231.

[29] H.-J. Freund, M. Bumer, J. Libuda, T. Risse, G. Rupprechter and S. Shaikhutdinov, *J. Catal.* **216** (2003), p. 223.

[30] H.-J. Freund, *Surf. Sci.* **500** (2002), p. 271.

[31] M.S. Chen, D.W. Goodman, *J. Phys. Condens. Matter.* **20** (2008), p. 264013.

[32] H.–J. Freund, G. Pacchioni, *Chem. Soc. Rev.* **37** (2008), p. 2224.

[33] N. Nilius, *Surf. Sci. Rep.* **64** (2009), p. 595.

[34] A. Del Vitto, G. Pacchioni, F. Delbecq, P. Sautet, *J. Phys. Chem. B* **109** (2005), p. 8040.

[35] M. Sterrer, E. Fischbach, T. Risse, H.–J. Freund, *Phys. Rev. Lett.* **94** (2005), p. 186101.

[36] M. Sterrer, M. Heyde, M. Novicki, N. Nilius, T. Risse, H. P. Rust, G. Pacchioni, H.–J. Freund, *J. Phys. Chem. B* **110** (2006), p. 46.

[37] G. Pacchioni, P. Pescarmona, *Suf. Sci.* **412/413** (1998), p. 657.

[38] H.–J. Freund, *Surf. Sci.* **601** (2007), p. 1438.

[39] B. Yoon, H. Häkkinen, U. Landman, A. S. Wörz, J-M. Antonietti, S. Abbet, K. Judai, U. Heiz, *Sience* **307** (2005), p. 403.

[40] M. Sterrer, M. Yulikov, E. Fischbach, M. Heyde, H.-P. Rust, G. Pacchioni, T. Risse, and H.-J. Freund, *Angew. Chem. Int. Ed.* **45** (2006), p. 2630.

[41] G. Pacchioni, L. Giordano, and M. Baistrocchi, *Phys. Rev. Lett.* **94** (2005), p. 226104.

[42] D. Ricci, A. Bongiorno, G. Pacchioni, and U. Landman, *Phys. Rev. Lett.* **97** (2006), p. 036106.

[43] L. Giordano and G. Pacchioni, *Phys. Chem. Chem. Phys.* **8** (2006), p. 3335.

[44] M. Yulikov *et al.*, *Phys. Rev. Lett.* **96** (2006), p. 146804.

[45] M. Sterrer, T. Risse, M. Heyde, H.-P. Rust and H.-J. Freund, *Phys. Rev. Lett.* **98** (2006), p. 206103.

[46] N. Nilius, E.D.L. Rienks, H.P. Rust, H.–J. Freund, *Phys. Rev. Lett.* **95** (2005), p. 066101.

[47] W. Schottky, *Phys. Z* **41** (1940), p. 570.

[48] V. Heine, *Phys. Rev.* **138** (1965), p. A1689.

[49] S. G. Louie and M. L. Cohen, *Phys. Rev. B* **13** (1976), p. 2461.

[50] G. Bordier and C. Noguera, *Phys. Rev. B* **44** (1991), p. 6361.

[51] S. Glaus, G. Calzaferri, and R. Hoffman, *Chem.–Eur. J.* **8** (2002), p. 1785.

[52] Y.-C. Yeo, T.-J. King, and C. Hu, *J. Appl. Phys.* **92** (2002), p. 7266.

[53] L. Giordano, F. Cinquini, and G. Pacchioni, *Phys. Rev. B* **73** (2006), p. 045414.

[54] T. T. Magkoev and G. G. Vladimirov, *J. Phys.: Condens. Matter* **13** (2001), p. L655.

[55] C. Loppacher, U. Zerweck, and L. M. Eng, *Nanotechnology* **15** (2004), p. S9.

[56] M. Pivetta, F. Patthey, M. Stengel, A. Baldereschi, and W.-D. Schneider, *Phys. Rev. B* **72** (2005), p. 115404.

[57] H. C. Ploigt, C. Brun, M. Pivetta, F. Patthey, and W.-D. Schneider, *Phys. Rev. B* **76** (2007), p. 165404.

[58] N. Nilius, E. D. L. Rienks, H.-P. Rust, and H.-J. Freund, *Phys. Rev. Lett.* **95** (2005), p. 066101.

[59] J. Goniakowski and C. Noguera, *Interface Sci.* **12** (2004), p. 93.

[60] M. Sgroi, C. Pisani, and M. Busso, *Thin Solid Films* **400** (2004), p. 64.

[61] L. Giordano, J. Goniakowski, and G. Pacchioni, *Phys. Rev. B* **67** (2003), p. 045410.

[62] G. Butti, M. I. Trioni, and H. Ishida, *Phys. Rev. B* **70** (2004), p. 195425.

[63] L. G. M. Pettersson and P. S. Bagus, *Phys. Rev. Lett.* **56** (1986), p. 500.

[64] A. Michaelides, P. Hu, M.-H. Lee, A. Alavi, and D. A. King, *Phys. Rev. Lett.* **90** (2003), p. 246103.

[65] V. De Renzi, R. Rousseau, D. Marchetto, R. Biagi, S. Scandolo, and U. del Pennino, *Phys. Rev. Lett.* **95** (2005), p. 046804.

[66] P. S. Bagus, V. Staemmler, and C. Wöll, *Phys. Rev. Lett.* **89** (2002), p. 096104.

[67] T. Schroeder, M. Adelt, B. Richter, M. Naschitzki, M. Bäumer and H.-J. Freund, *Phys. Rev. Lett.* **7** (2000), p. 7.

[68] T. Schroeder, M. Adelt, B. Richter, M. Naschitzki, M. Bäumer and H.-J. Freund, *Microelectr. Rel.* **40** (2000), p. 841.

[69] T. Schroeder, A. Hammoudeh, M. Pykavy, N. Magg, M. Adelt, M. Bäumer and H.-J. Freund, *Solid State Electron.* **45** (2001), p. 1471.

[70] T. Schroeder, J.B. Giorgi, M. Bumer and H.-J. Freund, *Phys. Rev. B* **66** (2002), p. 165422.

[71] T.K. Todorova, M. Sierka, J. Sauer, S. Kaya, J. Weissenrieder, J.-L. Lu, H.-J. Gao, S. Shaikhutdinov and H.-J. Freund, *Phys. Rev. B* **73** (2006), p. 165414.

[72] D. Ricci and G. Pacchioni, *Phys. Rev. B* **69** (2004), p. 161307.

[73] M. Chen, A.K. Santra and D.W. Goodman, *Phys. Rev. B* **69** (2004), p. 155404.

[74] J. Weissenrieder, S. Kaya, J.-L. Lu, H.-J. Gao, S. Shaikhutdinov, H.-J. Freund, M.M. Sierka, T.K. Todorova and J. Sauer, *Phys. Rev. Lett.* **95** (2005), p. 076103.

[75] L. Giordano, D. Ricci, G. Pacchioni and P. Ugliengo, *Surface Science* **584** (2005), p. 225.

[76] I.N. Yakovkin, *Surf. Rev. Lett.* **12** (2005), p. 449.

[77] S. Wendt, E. Ozensoy, T. Wei, M. Frerichsr, Y. Cai, M. Chen and D.W. Goodman, *Phys. Rev. B* **72** (2005), p. 115409.

[78] M. Sierka, T.K. Todorova, S. Kaya, D. Stacchiola, J. Weissenrieder, J.-L. Lu, H.-J. Gao, S. Shaikhutdinov, H.-J. Freund and J. Sauer, *Chem. Phys. Lett.* **424** (2006), p. 115.

[79] B.K. Min, W.T. Wallace and D.W. Goodman, *Surf. Sci.* **600** (2006), p. L7.

[80] L. Giordano, A. Del Vitto and G. Pacchioni, *J. Chem. Phys.* **124** (2006), p. 034701.

[81] J.-L. Lu, S. Kaya, J. Weissenrieder, T.K. Todorova, M. Sierka, J. Sauer, H.-J. Gao, S. Shaikhutdinov and H.-J. Freund, *Surf. Sci.* **600** (2006), p. L164.

[82] J.-L. Lu, S. Kaya, J. Weissenrieder, H.-J. Gao, S. Shaikhutdinov and H.-J. Freund, *Surf. Sci.* **600** (2006), p. L153.

[83] U. Martinez, L. Giordano and G. Pacchioni, *J. Chem. Phys. B* **110** (2006), p. 17015.

[84] M. Chen and D.W. Goodman, *Surf. Sci.* **600** (2006), p. L255.

[85] L. Giordano, D. Ricci, G. Pacchioni and P. Ugliendo, *Surf. Sci.* **601** (2007), p. 588.

[86] M. Chen and D.W. Goodman, *Surf. Sci.* **601** (2007), p. 591.

[87] C. Freysoldt, P. Rinke, M. Sheffler, *Phys. Rev. Lett.* **99** (2007), p. 086101.

[88] S. Kaya, M. Baron, D. Stacchiola, J. Weissenrieder, S. Shaikhutdinov, T.K. Todorova, M. Sierka, J. Sauer and H.-J. Freund, *Surf. Sci.* **601** (2007), p. 4849.

[89] J. Seifert, D. Blauth and H. Winter, *Phys. Rev. Lett.* **103** (2009), p. 017601.

[90] J. Seifert and H. Winter, *Surf. Sci.* **603** (2009), p. L109.

CHAPTER 2

Methods

2.1 Theory

2.1.1 Computational methods and models

Periodic supercell approach

In order to simulate a physical system two strategies are tipically possible: cluster and periodic approach. In this thesis will be used and described only the periodic approach that is implemented in the VASP (Vienna ab–initio simulation package) code.[1,2]

Because the electronic structure of solids is usually described in terms of band structure, a possible approach widely adopted is to use a unit cell containing a given number of atoms, periodically repeated in three-dimensions to account for the infinite nature of the crystalline solid. The Schrödinger equation is thus solved for the atoms in the unit cell, subject to periodic boundary conditions (PBC).

This model can also be extended to the study of point defects in the bulk or at the surface. However the application of this approach in presence of one defect in the unit cell results in a periodic repetition of it in the three directions of space, and thus in an extremely high concentration of defects in the simulated material. A pos-

sible way to avoid this problem is the use of a *supercell*: an increase of the size of the unit cell results in a decrease of the defects concentration. Even for large supercells containing several hundreds of atoms the defects concentration is orders of magnitude larger than in real systems where 10^{16}–10^{18} defects/cm^3 are usually present. At these concentrations one can reasonably assume that the defects are isolated and do not interact with each other. The supercell approach is therefore based on the assumption, largely verified, that neutral defects do not interact appreciably except when they are very close to each other, so that rapid convergence is achieved with increasing size of the supercell.

To simulate surfaces, the supercell approach is combined with the *slab* model (figure 2.1). Here the initial supercell is constituted by a sufficient number of atomic layers and a certain amount of vacuum along the z direction (~ 10 Å). If the vacuum spacer is wide enough, the periodic repetition of the cell in the three directions will generate a system with non interacting slabs which simulates a surface.

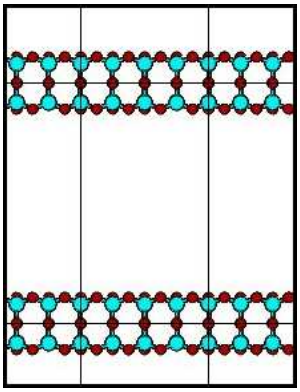

Figure 2.1: Schematic illustration of a slab model used to simulate a surface in the periodic supercell approach.

Density functional theory and plane waves

The VASP code implements the Density Functional Theory (DFT) and the wave funtion of the system is thus described in terms of Kohn-Sham orbitals.[3,4] In the framework of the supercell approach (periodic system) the Bloch theorem describes the single electron wavefunction in the Kohn-Sham equation. The theorem states that for a periodic system the electronic wave function can be written as a product

of a wavelike part an a cell–periodic part:[5]

$$\psi_{n,\mathbf{k}}(\mathbf{r}) = e^{i\mathbf{k}\cdot\mathbf{r}} u_{n,\mathbf{k}}(\mathbf{r}) \tag{2.1}$$

where $u_{n,\mathbf{k}}(\mathbf{r})$ is the periodic function, with n band index. There are different methods to choose in order to expand the periodic function (basis set). In periodic system is useful to use a plane wave basis set and thus each electronic wave function can be written as a sum of plane waves:

$$u_{n,\mathbf{k}}(\mathbf{r}) = \sum_{\mathbf{G}} c_{n,G}\, e^{i\mathbf{G}\cdot\mathbf{r}} \tag{2.2}$$

Given $\mathbf{l}$ a lattice vector of the crystal and m an integer, $\mathbf{G}$ is the reciprocal lattice vector defined as $\mathbf{G}\cdot\mathbf{l} = 2\pi m$ for all $\mathbf{l}$. In principle an infinite plane-wave basis set is required to expand the electronic wave function. Actually, it is possible to truncate the expansion, being sure to include only the wave function with a kinetic energy under a fixed threshold. In fact, the coefficients $c_{n,\mathbf{k}+G}$ for the plane waves with small kinetic energy are more important than those with higher kinetic energy. In practice only those plane waves $|\mathbf{G}+\mathbf{k}|$ for which

$$\frac{\hbar^2}{2m_e}|\mathbf{G}+\mathbf{k}|^2 < \mathrm{E}_{\mathrm{cut}} \tag{2.3}$$

are included. Hence, the introduction of a kinetic cut-off, combined with the Bloch theroem, allows to have a finite basis set to describe the system. However, this leads to a computational error in the representation of the total energy; clearly this can be reduced by increasing the value of $\mathrm{E}_{\mathrm{cut}}$ until the energy is converged.

The electronic states are allowed only for a given set of $\mathbf{k}$ vectors in the reciprocal lattice. These vectors constitute a subspace of points, called k–points, which can sample in a significative way the first Brillouin zone (BZ).[6] In VASP this discrete BZ sampling is based on the so–called Monkhorst-Pack.[7] To obtain a precise description of metals, for example, a denser grid of k–points is needed in order to precisely define the Fermi surface. Note that the larger the supercell the smaller the corresponding BZ becomes. For sufficently large supercell this BZ sampling becomes less critical and using just the Γ– point might be a resonable approximation.

Projector augmented wave method

In 1994 Blöchl proposed a new method to determine the electron-ion interaction, called *projector augmented wave* (PAW).[8,9] The PAW method describes the wave

function as an overlap of different terms. The first part is a plane wave (the pseudo–wavefunction) and the second is an expansion on pseudoorbitals and atomic orbitals for each atom. The plane wave possesses the right flexibility to describe the bonds and the external regions of the wave function, and the correct behavior of the nodal structure of the nuclei is granted by the expansion through atomic orbitals. The PAW method combines the advantages of both representations in a well defined basis set to find the all electron wave function, the energy functional and all the other phisycal quantities of interest. This method is often referred to as an all-electron method, not in the sense that all the electrons are treated explicitly, but in the sense that the valence electronic wave functions are kept orthogonal to the core states.

2.1.2 Properties studied

All the theoretical results presented in this work concern the study of different properties of ultra–thin oxide films on metal substrates often interacting with supported metal atoms or clusters. In particualr vibrational, structural, energetic, magnetic and electonic properties are studied and most of the times are directly compared to experiments (briefly described in the next section). In the present section a general description of how the work function of the systems has been calculated and how STM images have been simulated is reported. All other quantities have been obtained by standard methods.

Work function

The work function of the metal or oxide/metal surfaces is defined as the energy of the vacuum level E_V (determined as the self–consistent potential in the vacuum) with respect to the Fermi level of the metal or of the metal/oxide interface E_F, and is given by the expression:

$$\Phi = E_V - E_F \tag{2.4}$$

As described above, because of the periodic supercell approach (slab), there are two surfaces inside the supercell that usually have different work functions (asymmetry of the system) so the total potential must converge in two different vacuum levels (there is only one Fermi level in the system). But because of the PBC (the potential must be continuos along the direction perpendicular to the slabs) this is not possible and an unphysical electric field is created in the vacuum regions between the slabs (dashed line in Figure 2.2). In order to calculate the two vacuum levels in VASP code

an artificial dipole sheet is indroduced in the middle of the vacuum, Figure 2.2. It is important to note that this field is not an external field but a self–consistent quantity determined by the charge distribution at the slab surfaces. With this correction the artificial electrostatic interaction between the surfaces through the vacuum region is canceled making possible the use of equation 2.4 to evaluate the two work functions inside the supercell (Φ_1 and Φ_2 in figure 2.2).

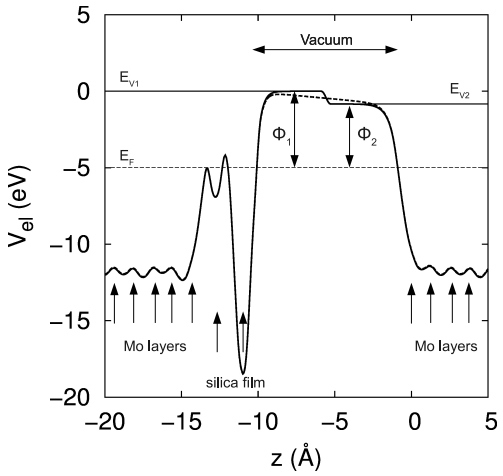

Figure 2.2: Plane avaraged electrostatic potential plotted along the direction perpendicular to a SiO_2/Mo(112) slab. In figure are indicated the Fermi energy E_F, the work function Φ_1 of a SiO_2/Mo(112) interface and of the clean Mo(112) surface Φ_2. The dipole correction is visible as a potential jump in the middle of the vacuum region. The dashed line rapresent the potential without a dipole correction.

Simulated STM images

In this thesis a large number of experimental results from Scanning Tunneling Mycroscopy (STM) and Spectroscopy (STS) are reported. In order to understand and interpretate these data we need to be able to simulate these features (STM images and STS spectra) from DFT calculations.

There are several theories that one can use to simulate STM images that depend on the system studied and on the level of approximation desired: the Tersoff–Hamann approach,[10,11] the transfer Hamiltonian or the Bardeen approach,[12] the scattering or Landauer–Bütticker approach,[13] and the Keldysh or non–equilibrium

Greens function approach.[14]

In this thesis the simplest and most common approach due to Tersoff and Hamman will be used. This is based on the properties of the surface only and assumes the tip to be spherical. In particular the current is proportional to the local density of states of the surface:

$$I(\mathbf{r}_0) = CV_{bias} \sum_{E_n<E_F-eV_{bias}}^{E_n<E_F} |\psi_v(\mathbf{r}_0, E_n)|^2 \tag{2.5}$$

where V_{bias} is the potential of the sample with respect to the tip, $\mathbf{r}_0$ is the position of the tip's center, and C is a prefactor that depends on the work function of the surface, density of states of the tip and radius of the tip.[10] Within this approach we need to calculate the partial electron density at the position $\mathbf{r}_0$ above the surface due to the electronic states in the energy window between E_F and $E_F + V_{bias}$.

In the Tersoff–Hamman framework the differential conductance probes the density of states of the (isolated) sample, evaluated at the centre of the tip apex. With this assumption we can direclty compare the density of states of the surface calculated from DFT to the dI/dV spectra. Again we want to stress that this is an approximations and only qualitative results can be obtained. However for the systems discussed inside the thesis we found very good agreement with the experimental results, as described in the results sections.

2.2 Experimental

The work of this thesis has been done in close collaboration with different experimental groups and a lot of experimental results are discussed. In the present section a brief overview of the main techniques employed to grow and characterize ultra–thin oxide films is reported.

The experiments have been done in custom–built systems capable of performing a variety of procedures in Ultrahigh Vacuum (UHV) at very low temperature, 5–10 K. A picture and a simplified scheme of the machine used by the group of Dr. Niklas Nilius at the FHI is reported in figure 2.3.

The method used to grow oxide thin films in UHV conditions is by metal atoms deposition in an oxygen atmosphere. Here a metal is vaporized (e.g. in a Knudsen cell) and deposited onto a metal substrate in a given background O_2 pressure. One grows in this way films of various thickness on the substrate whose quality is strongly dependent on a number of parameters (e.g. temperature of the substrate, flux of metal vapor, O_2 pressure, etc.). Usually an annealing step in the growth process is done after the oxidation one. This step consists of an heating treatment (usually around 700–1100 K) for a well defined period of time and allows surface diffusion processes that favors order and crystallinity the oxide film.

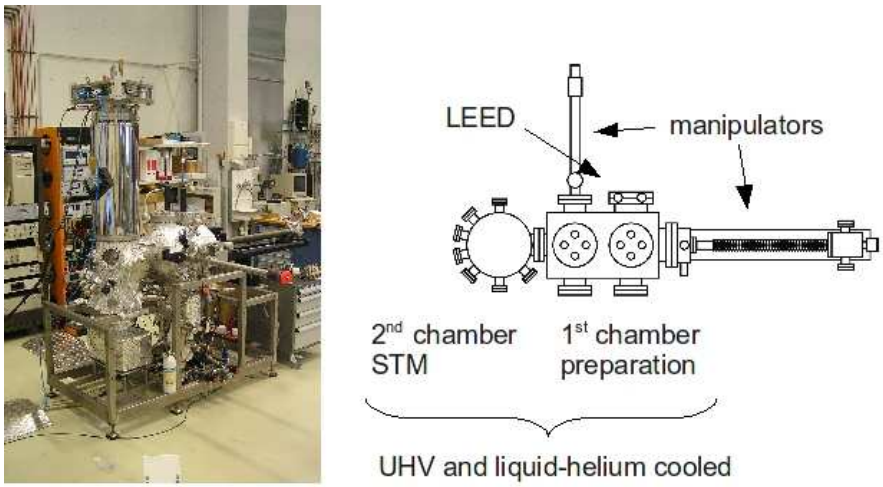

Figure 2.3: One of the experimental setup used in the Scanning Probe Spectroscopy Group of Dr. N. Nilius at the FHI.

The use of thin oxide films allows to use a variety of surface science techniques that require a conductive sample. For example scanning tunneling microscopy (STM) is very important for the structural and electronic characterization of surfaces and of adsorbed metal atoms, clusters or molecules. STM is based on the measurement of the tunneling current flowing from a metal tip to the sample; it provides an image either of the empty or of the filled states of the atoms on the surface, depending of the relative sign of the applied voltage. When one is dealing with insulating materials, like for instance MgO or SiO_2 the use of STM is not possible unless one makes use of ultra–thin films of a few layers thickness. In this way the direct tunneling of electrons between the tip and the metal substrate through the thin oxide layer is not only possible but permits to obtain good STM images even with atomic resolution. Imaging single atoms and clusters with a STM tip generally requires atomically clean surfaces and an extreme stability at the tip–sample junction. Therefore, ultra-high vacuum environments and low substrate temperatures are needed.

Another very useful tool that provides informations about the structure of the surface sample is the low energy electron diffraction (LEED) technique. In particular LEED gives informations about long range order and because of the low energy of the electron beam used to bombard the surface is sensitive only to the first few layers of the surface that in our case is the thin oxide film.

Besides structural properties of the surface also electronic properties have been characterized. Ultra–violet photoemission spectroscopy (UPS) provides a way to investigate the valence band structure of the oxide films. In this work of thesis a large number of experimental results concerning scanning tunneling spectroscopy (STS) are described. STS probes the conduction properties of the surface and gives tipical dI/dV spectra. As described in the previous section an approximation often adopted of STS spectra is the calculated LDOS of the sample allowing the characterization of the unoccupied and occupied electronic states and in particular on local and on the atomic scales.

Bibliography

[1] G. Kresse, J. Hafner, *Phys Rev. B* **47**(1993) p. R558.

[2] G. Kresse, J. Furthmüller, *Phys. Rev. B* **54** (1996) p. 11169.

[3] P. Hohenberg, W. Kohn, *Phys. Rev. B* **136** (1964) p. 864.

[4] W. Kohn, L.J. Sham *Phys. Rev. A* **140** (1965) p. 1133.

[5] N. Ashcroft, N. Mermin, *Solid State Physics* International Thomson Publishing, (Philadelphia 1976)

[6] M.C. Payne, M.P. Teter, D.C. Allan, T.A. Arias, J.D. Joannopoulos, *Rev. Mod. Phys.* **64** (1992) p. 1047.

[7] H. Monkorst, J. Pack, *Phys. Rev. B* **13** (1976) p. 5188.

[8] P.E. Blöchl, *Phys Rev. B* **50** 17953 (1994)

[9] O. Bengone, M. Alouani, P.E. Blöchl, J. Hugel, *Phys Rev. B* **62** 16392 (2000)

[10] J. Tersoff, D. R. Hamann, *Phys. Rev. Lett.* **50** (1985), p. 1998.

[11] J. Tersoff, D. R. Hamann, *Phys. Rev. B* **31** (1985), p. 805.

[12] J. Bardeen, *Phys. Rev. Lett.* **6** (1961), p. 57.

[13] M. Bütticker, Y. Imry, R. Landauer, S. Pinhas, *Phys. Rev. B* **31** (1985), p. 6207.

[14] Y. Meir, N.S. Wingreen, *Phys. Rev. Lett.* **68** (1992), p. 2512.

Part I

Charging of metal atoms and clusters on ultra–thin films

CHAPTER 3

Control of charge state of Au atoms on MgO/Ag(100)[†]

As reported in the introduction (Section 1.3) it has been recognized that the thickness of the oxide films, as they are grown on metal substrates, may be used as a design principle to create materials of potential in catalysis. One very interesting phenomena that can occur is the charge transfer of one electron from the metal substrate directly to an adsorbed species (atoms, clusters or even molecueles). On the basis of density functional theory (DFT) calculations it was proposed that charge transfer may occur for metal atoms and clusters adsorbed on a supported thin–oxide film, provided that the adsorbed metal exhibits a high electron affinity and the film thickness does not exceed a few monolayers.[3–5] In particular, Au atoms adsorbed on a thin MgO film grown on Mo(100) and Ag(100) are expected to be negatively charged in contrast to their counterparts on bulk MgO (or thick MgO films), which were proven to be essentially neutral.[6]

The formation of anions on the surface remains difficult to prove experimentally. Also theoretically, the discrimination between neutral and charged adsorbed species is not straightforward. In this chapter we perform an accurate analysis of the observable consequences of the formation of Au anions on an oxide surface. To this end

[†]The results described in this Chapter have been reported in: M. Sterrer, T. Risse, *U. Martinez*, L. Giordano, M. Heyde, H-P Rust, G. Pacchioni and H-J Freund, *Physical Review Letter* **98** 096107 (2007) and L. Giordano, *U. Martinez*, S. Sicolo, G. Pacchioni, *The Journal of Chemical Physics* **127** 144713 (2007)

we consider the following properties: scanning tunneling microscopy images, spin distribution, density of states, Bader charges, substrate relaxation, work function changes, CO vibrational frequency, electric field effects, and core level shifts. In the case of STM images a direct comparison with low–temperature scanning tunneling microscope has been possible. Most of the other properties are accessible experimentally, at least in principle. Taken individually, these properties do not necessarily provide conclusive evidence about the charged nature of the adsorbate. Taken together, they offer a complete and unambiguous characterization of the formation of Au anions.

3.1 Computational and Experimental Details

Computational Details

The calculations has been performed with the VASP code (see Sec. 2.1.1, pag. 25). The kinetic energy cutoff has been set to 400 eV. A vacuum of at least 10 Å separates the slabs and a dipole correction has been applied. The Ag(100) substrate has been modeled by four metal layers (three for the study of the effect of an electric field). A two–layer (2L) MgO film has been deposited on the metal substrate. The MgO(100) single crystal surface has been represented by a three–layer MgO slab.

The Ag lattice constant (a_0=4.16 Å) is 2% smaller than the MgO one (a_0=4.25 Å). Therefore, the MgO layers are slightly contracted with respect to their bulk distance when supported on the Ag metal. During geometry optimization of the MgO/metal interface, all atoms in the MgO film and in the two surface nearest Ag layers were relaxed while the remaining two metal layers were frozen at bulk positions. On the MgO(100) surface the optimization is restricted to the two top layers of the film.

For the calculations we used 3×3 or 4×4 supercells containing 9 Ag and 18 Mg+O or 16 Ag and 32 Mg+O atoms per layer, respectively. Spin polarized calculations have been performed to account for the presence of an unpaired electron in the valence shell of Au atoms. We notice that this is an important aspect which is often neglected in the calculations of supported metal atoms or clusters. Brillouin–zone integrations have been performed on a grid of 4×4×1 (3×3 cell), 2×2×1 (4×4 cell) Monkhorst–Pack points. The calculations in the presence of an external electric field and for CO adsorption have been performed at Γ point.

Experimental Details

Magnesium oxide thin films were prepared by reactive deposition of Mg in an oxygen ambient using a Ag(100) substrate. The Ag(100) single crystal was cleaned by repeated sputter (Ar^+, 10 $\mu A \cdot cm^{-2}$)/anneal (700 K) cycles. Mg was deposited on Ag(100) from a UHV evaporator at an oxygen pressure of 1×10^{-6} mbar and a substrate temperature of 570 K. The MgO growth rate was 1 ML·min^{-1}. The experiments were performed in a custom–built low–temperature STM operating at 5 K. Au and Pd atoms were evaporated from a hot filament (T≈1000 K) at a deposition rate of 0.1 ML·min^{-1} and a sample temperature of 5 to 10 K.

3.2 Results and Discussion

3.2.1 STM images of Au and Pd atoms on MgO/Ag(100)

Figures 3.1a and 3.1b show STM images (30 nm×30 nm) of Au and Pd atoms, respectively, evaporated on a 3 ML thin MgO film at a substrate temperature of 5–10 K. For the coverage of θ=2–3$\times 10^{-2}$ ML single metal atoms, imaged as bright protrusions for the given tunneling conditions, are the predominant species on the surface, while aggregates and clusters play only a minor role. The bright squarelike features in the STM images originate from MgO ad–islands. A qualitative inspection of Figure 3.1a reveals that Au atoms are evenly distributed on the surface with rather well defined nearest–neighbor distances, which is an indication for strong adatom interactions. In contrast, Pd atoms (Figure 3.1b) deposited at the same conditions exhibit a more or less random distribution. Thus, the electronic properties of the adsorbed metal atoms and their interaction with the thin MgO film play an important role for the observed nucleation behavior. To ensure that the ordering of Au atoms on thin MgO films is not mediated by interactions with the metal substrate, such as coupling to surface states or Friedel oscillations,[7,8] Au atoms were also deposited on bare Ag(001). This situation, shown in Figure 3.1c, reveals a random distribution of Au atoms indicating that the thin MgO layer plays an essential role for the observed ordering of Au atoms on MgO/Ag(001).[†]

What is the reason for this long–range interaction? According to recent theoretical DFT calculations it has been shown that Au atoms adsorbed on a thin MgO film

[†]For a quantitative analysis of the adatoms interactions, a radial pair distribution has been calculated for the three cases: Au and Pd on MgO/Ag(100) and Au on Ag(100). For further details see, Phys. Rev. Lett. **98**, 096107 (2007).

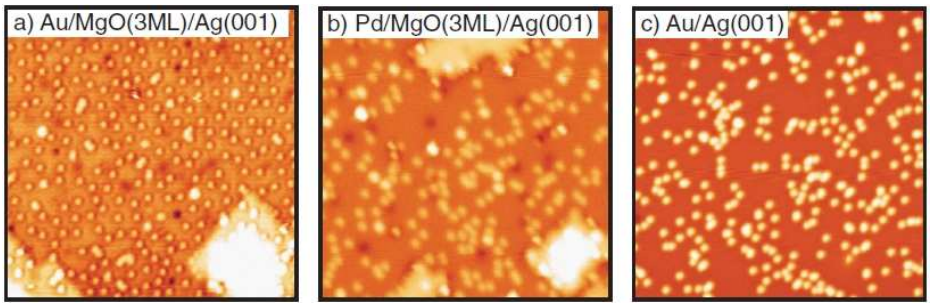

Figure 3.1: STM images (30 nm×30 nm) of (a) Au atoms adsorbed on 3 ML thin MgO films (θ=2.9% ML Au, V_S=+0.5 V, I_T=11 pA); (b) Pd atoms adsorbed on 3 ML thin MgO films (θ=2.3% ML Pd, V_S=+0.2 V, I_T=13 pA); (c) Au atoms adsorbed on bare Ag(100) (θ=2.9% ML Au, V_S=+0.1 V, I_T=100 pA).

are charged, in contrast to the situation found for unsupported MgO.[3] As compared to Au, Pd has a much lower electron affinity, thus, DFT calculations show the Pd 5s level to remain above the Fermi energy–meaning the Pd atoms remain neutral even on ultimately thin MgO films of 1 ML thickness.[3] Based on these theoretical considerations the experimentally observed two–dimensional order of Au atoms adsorbed on a 3 ML thin MgO film (Figure 3.1a) can be explained by the repulsive interactions between partially negatively charged Au atoms.

Is there further evidence that can be acquired from the STM experiments for the interpretation that Au atoms are charged, whereas Pd atoms remain neutral when adsorbed on a 3 ML thin MgO film? To this end we compare the experimental STM signatures of single Au and Pd atoms with simulated ones applying the Tersoff–Hamann approximation[9] on the electronic structure derived by DFT calculations, where Au atoms are charged and Pd atoms are neutral, respectively (Figure 3.2). In experiment, the Au atoms are imaged as protrusions surrounded by a depression (Figure 3.2a and b), whereas Pd appears as a diffuse protrusion only (Figure 3.2d and e). Both the size of the atoms as well as the depression in case of the Au atom is very well reproduced by the simulated STM images (Figure 3.2c and f, respectively) corroborating our assignment of the different charge states of the respective metal atoms. This is further shown by the fact that the "sombrerolike" shape in the STM image of the Au atom is not present for a neutral Au adsorbate. In fact by freezing the coordinates of the substrate we have been able to converge on a solution where the charge transfer does not occur and the Au atom is neutral (see polaronic dis-

tortion below). This allows us a direct comparison of the simulated STM images of neutral and charged Au atoms on the same substrate, MgO/Ag(100) (note that in this case the MgO film is 2ML thick). As can be seen from Figure 3.3, the two images are quite different. The STM images of a neutral Au^0 (Figure 3.3b) does not exhibit the depression of Figures 3.2a–c, and of Figure 3.3a, and is hardly distinguishable from that of Pd. This provides a strong and direct proof of the charged nature of the supported Au atom.

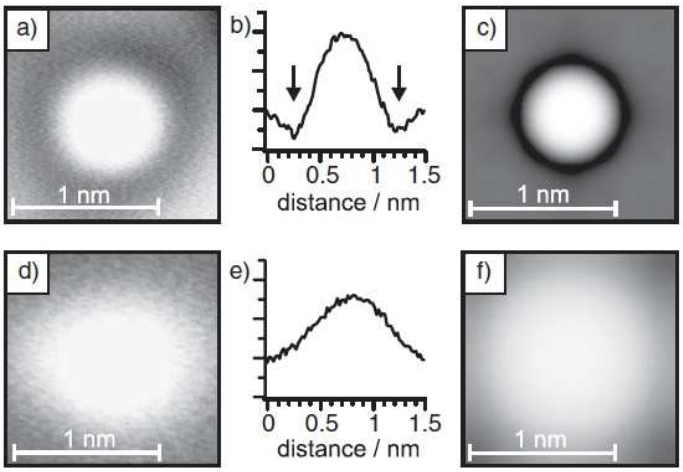

Figure 3.2: Experimental STM images and height profiles, and corresponding simulated STM images of single Au (a–c) and Pd (d–f) atoms on the surface of 3ML MgO/Ag(100), respectively. The bias voltage in the experimental and simulated STM images is V_S=+0.5 V.

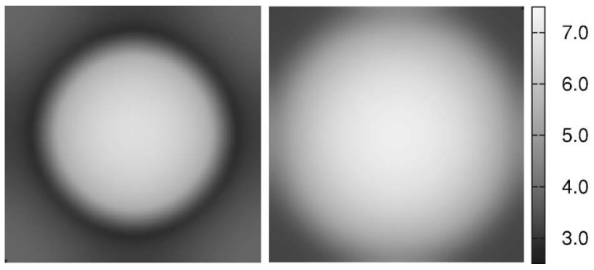

Figure 3.3: (a) Simulated STM image of Au^- formed on 2ML MgO/Ag(100); (b) simulated STM image of a Au^0 atom formed on 2ML MgO/Ag(100). The z=0 reference plane is that of the MgO surface. The dimension of the images is 0.9 nm×0.9 nm.

A characteristic depression around Au atoms was recently observed for Au on 2 ML thin NaCl films.[10] However, in the case of Au/NaCl(100)/Cu(111) the atoms were neutral directly after evaporation. Charging of the atoms was induced by a voltage pulse applied between sample and STM tip. In contrast to these experiments the Au atoms observed on the thin MgO film show the ringlike depression immediately after deposition indicating that charging of Au occurs in the course of the adsorption process.

The STM analysis is fully consistent with all the rest of theoretical evidence that will be described in the next section, and provides a fingerprint of the anionic nature of adsorbed Au atoms.

3.2.2 Other observable evidences of a charge transfer

In the following we discuss a series of evidences of the occurrence of a charge transfer in Au atoms on MgO/Ag(100) films when certain conditions are met. We will also compare these results with those obtained for Au atoms which are clearly in their atomic neutral state. This can be obtained either by depositing Au atoms on unsupported MgO films, modeling the bulk oxide surface, or Au adsorption on MgO/Ag(100) thin films where we forced the system to converge to the neutral state of the atom (see below).

Spin Properties

Neutral Au has a $5d^{10}6s^1$ valence configuration. In the absence of charge transfer, a net spin density of $\approx$1 is also expected for adatoms. This is, in fact, the situation found for Au atoms deposited on the terrace sites of the MgO(100) surface.[11] Electron paramagnetic resonance (EPR) spectra have been obtained for Au atoms on $\approx$20 layer MgO films on Mo(100), providing a clear and unambiguous evidence for the presence of a residual spin density on the adsorbed Au atom.[11] Furthermore, it has been possible to measure the hyperfine coupling constants of the deposited Au with the ^{17}O nuclides of the MgO substrate, showing that the Au atoms sit on top of the oxide anions of the surface,[11] as predicted theoretically.[12] A spin density of about $1e$ is computed for Au_1/MgO(100) as the difference between spin up and spin down for the entire system, and the corresponding hyperfine coupling constants have been determined using cluster models, Figure 3.4.[11] The EPR properties of supported Au atoms differ from those of free Au atoms because of polarization effects due to the Pauli repulsion of the $6s$ valence level with the MgO surface; the

shifts is not due to the occurrence of a net charge transfer.[11,13] These studies have proven unambiguously that Au atoms on the surface of MgO(100) are basically neutral, being the charge transfer from the oxide anion to Au of 0.2e at most.

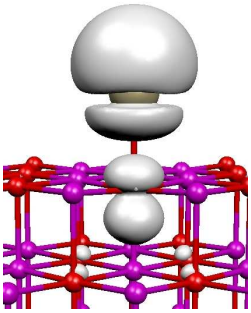

Figure 3.4: Spin density contour plot for a Au atom adsorbed on top of an oxide anion on the MgO(100) surface.

When Au atoms are adsorbed on two to three layer MgO films on Mo(100) or Ag(100) metal single crystals, a nonmagnetic solution has been found. This result has to be carefully checked in order to guarantee that the absence of spin polarization is not due to the smearing parameter used to generate the density of states (DOS) plots. Once the absence of net magnetic moment is confirmed, there are only three possible explanations of the spin quenching: (a) a charge transfer has occurred from the Au atom to the substrate, forming Au^+; (b) a charge transfer has occurred from the substrate to the Au atom, forming Au^-; and (c) a covalent bonding has formed by coupling an unpaired electron on the substrate with the singly occupied 6s level of Au, forming a S–Au bond (S=substrate). Mechanism (c) can be discarded since the number of paramagnetic defects on the MgO surface is below the detection limit of EPR;[14,15] in practice, there are no such centers on the as prepared substrate. This leaves space only for hypotheses (a) and (b), occurrence of charge transfer. The fact that for $Au_1/MgO/Ag(100)$ the calculation converges to a nonmagnetic solution is sufficient to conclude that a charge transfer has occurred, but it does not provide information about the direction of this charge transfer.

Density of states

A clear indication of the nature of the charge transfer is provided by the DOS curves. When Au is deposited on the MgO(100) surface, the two α and β compo-

nents of the 6s level are occupied and empty, respectively, reflecting the "atomic" nature of the supported species, Figure 3.5a. In a system like Au adsorbed on MgO/Ag(100) or MgO/Mo(100) films, the distinction between empty and filled states is determined by the Fermi level of the metal substrate.[3,5] Notice that this is not the same as the Fermi level of the pure metal, since the presence of the oxide film can produce deep changes in the metal work function (see below). In Figure 3.5b are shown the DOS curves of a Au atom adsorbed on MgO/Ag(100). It is apparent that both the α and β components of the Au 6s level are occupied being below the Fermi level. Thus, one electron has been transferred from the MgO/Ag(100) substrate to the 6s valence level, which becomes doubly occupied, thus accounting for the absence of spin polarization in the ground state of the system. This could be interpreted as the formation of a Au^- species with valence configuration $5d^{10}6s^2$. However, it should be noted that the 5d states are partly hybridized with the O 2p states. In semicovalent oxides (e.g., TiO_2) this could lead to a charge flow from the filled 5d levels to the partly filled O 2p states, thus reducing the net charge on Au, $Au^{\delta-}$, with $\delta \leq 1$. This situation is rather unlikely on MgO due to the highly ionic nature of the oxide and to the presence of fully reduced O^{2-} anions. On this basis, one can conclude that the DOS curves provide clear, although purely theoretical evidence for the formation of a gold anion. Notice that this conclusion is independent of the site where the Au atom is sitting. Total energy calculations have shown that the adsorption on top of O, on top of Mg, or in the fourfold hollow sites of ultrathin MgO films is equally preferred within one–tenth of an eV and that the charge transfer occurs at any site. Notice that on thick MgO films, where charge transfer does not occur, adsorption on top of O is definitely preferred.[3,11]

The presence of occupied states above the oxide valence band can be investigated using the metastable impact electron spectroscopy (MIES).[16] In MIES collisions of slow noble gas atoms (e.g., He) in excited metastable states with the surface give rise to neutralization and also electron emission. During deexcitation, the He 2s electron tunnels into an empty level of the surface (target) atoms. This is followed by an Auger neutralization process, in which an electron from the target atom is ejected (and measured using standard techniques). Only those surface atoms which come into contact with the impinging metastable He^* atoms emit electrons and the technique is extremely surface sensitive. In this respect, MIES measurements offer the opportunity to identify the location of occupied and empty states of the adsorbate species, thus helping in the characterization of the their charged nature. The main problem here is the sensitivity of the technique to the low concentration of

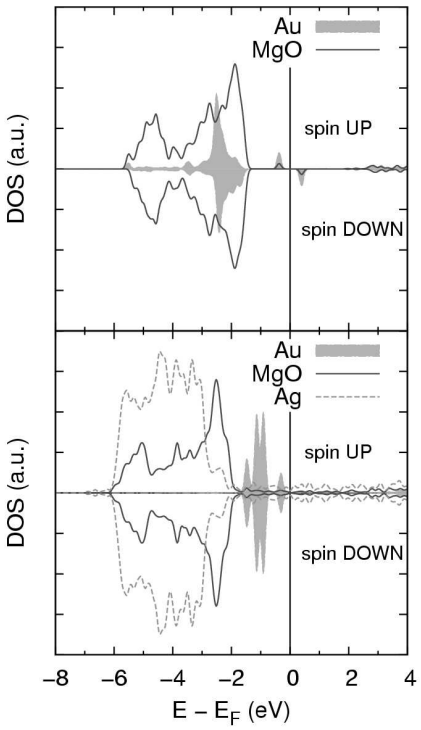

Figure 3.5: Spin resolved DOS curves for $Au_1/MgO(100)$ (on top of O adsorption) and $Au_1/MgO/Ag(100)$ (on top of Mg adsorption).

deposited atoms used in experiment.[11]

Bader Charges

The asymmetric distribution of electrons in chemical bonds results in partial charges on the atoms. Despite its usefulness, the concept of atomic charge is somewhat arbitrary, because it depends on the method used to discriminate between one atom and the next one in a molecule or a solid. It is not surprising that this problem has been a challenge for quantum chemists for decades. Mulliken charges are based on the so–called Mulliken population analysis.[17] The problem with this approach is that the equal division of the off–diagonal terms of the overlap population between two centers leads to charge separations which are often unphysical. A completely different approach has been followed by Bader in his theory of atoms in molecules.[18]

This is based on the definition of an atom in a complex system (molecule or solid) in terms of the topology of the electron density, and, in particular, as a region of real space bounded by surfaces through which there is a zero flux in the gradient vector field of the electron density. This provides a mathematical definition for a given basin where to integrate the charge.

Using this method, we have determined the charges for a Au atom adsorbed on MgO(100) and on a MgO/Ag(100) film. On MgO(100) the Au atom has a small negative charge of $-0.2e$. This results from the mixing of the O $2p$ orbitals with the Au $6s$ and $6p$ states; being MgO an ionic solid, its oxygen atoms are almost full anions and can only donate charge (basic character). This results in the small negative charge measured for the supported Au atom. For Au adsorbed on MgO(2L)/Ag(100) films, we have considered two adsorption sites, on top of Mg and the fourfold hollow site. In the first case the value of the Bader charge is $-0.77e$, in the second $-0.79e$, i.e., typical of a full anion. This clearly shows, apart from any other consideration, the very different nature of atomic gold deposited on the bare MgO surface or on an ultrathin film. It is also completely consistent with the other measures discussed previously, in particular, with the analysis of the DOS curves.

A less refined way to determine the atomic charges of deposited Au atoms is to plot the total electron density of the system in the planes parallel to the surface for various z distances, Figure 3.6. In this way one can identify the minimum of the density between the surface and the adatom layer, and integrate the charge around the adatom from this minimum point to large z values where the electron density vanishes, Figure 3.6. With this approach we found 11.58 electrons associated with the Au adatom, corresponding to a net charge of $-0.58e$, a bit smaller than that obtained with the Bader analysis. This method, although less accurate than the Bader analysis, is yet much more reliable than another technique used time to time in the literature and based on the determination of charge density difference maps. In our case this consists in determining the following quantity:

$$\Delta\rho = \rho[Au/MgO/Ag(100)] - \rho(Au) - \rho[MgO/Ag(100)]$$

a charge accumulation is found around the Au adatom, consistent with the fact that electrons flow from the substrate to the adsorbate, Figure 3.6. A quantitative estimate of the amount of charge transferred, however, is less straightforward. Integrating the charge around Au, taking the plane where $\Delta\rho$=0 as separation from the MgO/Ag(100) substrate, we obtain a net charge on Au of $-0.38e$, i.e., about one-half of the more realistic Bader charge. This is due to the rather arbitrary choice of

subtracting noninteracting fragments from a bound system.

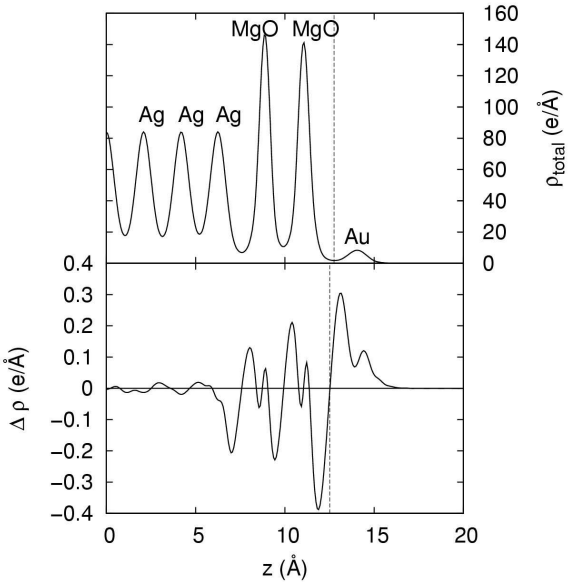

Figure 3.6: Profile of the laterally integrated total charge density ρ (top) and of the charge density difference $\Delta\rho$ (bottom) as a function of z (plotted along the line which goes through the Au adatom). The vertical dotted line indicates the point used to integrate the charge around the Au adatom (see text).

Polaronic distortion

The formation of a charged species inside or on the surface of an insulator is conceptually similar to the creation of an electron trap (a defect) in the material. Very often, the formation of charge traps in insulators is accompanied by a substantial distortion of the lattice. This polaronic distortion helps in stabilizing the state occupied by the extra electron. In many respects the formation of a negatively charged Au atom on the surface of MgO resembles this situation. A case where this phenomenon has been clearly observed is that of Au atoms on ultrathin NaCl films on Cu(111). Using the tip of a scanning tunneling microscope (STM), Repp *et al.*[10] have been able to selectively charge Au atoms and transform them into Au^- anions. DFT calculations have shown that the formation of the Au^- anion induces a strong relaxation of the substrate which is essential to stabilize the charged state. In partic-

ular, the Cl^- anion underneath the Au adatom moves downward by 0.6 Å and the surrounding Na^+ cations move 0.6 Å upward. This relaxation is removed once the electron is detached from the Au atom which goes back to the neutral state.

This phenomenon is also observed when Au is deposited on MgO/Ag(100) two–layer films. We discuss, in particular the case of Au adsorption on top of Mg.[†] The Mg cation where Au is bound relaxes outward by 0.44 Å and the O anion underneath relaxes down, toward the Ag(100) surface, by 0.2 Å; the other oxide anions in the top layer around the adsorption site relax inward by 0.10 Å, Figure 3.7. This polaronic relaxation contributes 0.8 eV to the stability of the surface complex (computed with respect to the unrelaxed surface) and is an essential ingredient for the stabilization of the charged state.

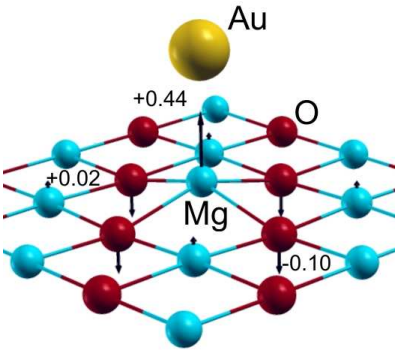

Figure 3.7: Schematic representation of the polaronic distortion due to the formation of a Au anion on MgO/Ag(100) films.

To further illustrate this point, we have performed a calculation on the same Au_1/MgO/Ag(100) system without allowing the MgO substrate to relax. In this case, using a 3×3 supercell, no charge transfer is found! The ground state is spin polarized (spin polarization on Au 0.60e, computed as different between spin up and spin down for the entire system) with the 6s level of Au only singly occupied. Also the Bader analysis attributes to this atom a charge of $-0.36e$ only, consistent with the presence of a basically "neutral" Au atom. The occurrence of a strong spontaneous distortion of the substrate in response to the adsorption of Au is a strong indication of the occurrence of a charge transfer. Although difficult to measure, this distortion

[†]For the adsorption on the hollow site the Mg cations move outwards by 0.30 Å and the O anions move downwards by 0.1 Å.

represents an observable property accessible in principle to experiment.

Work function change

The formation of an overlayer of charged species adsorbed on a metal surface has direct consequences on the work function Φ of the system. The classical picture proposed by Kingdom and Langmuir[19] and by Gurney[9] is that Φ increases for a negative adsorbate on a metal since an image charge forms into the bulk metal giving rise to a dipole layer which the emitted electron must pass through.[21] On the MgO(2L)/Ag(100) film the computed work function is 2.92 eV, i.e., about 1 eV smaller than on pure Ag(100) because of polarization–compression effects (see Introduction, section 1.3, for a thorough discussion).

Once Au atoms are deposited on these ultrathin films, Φ becomes 5.29, 4.76, and 4.48 eV, respectively, for Au adsorption on top of Mg, in the hollow sites, and on top of O. Thus, there is an increase in work function by 1.5–2.3 eV induced by adsorbed Au, in complete agreement with the expectation of Gurney's model for a negative adsorbate. The work function change, $\Delta\Phi$, is clearly dependent on the adsorption site: $\Delta\Phi$=2.37 eV for Au^- on top of Mg is much larger than for adsorption on top of O ($\Delta\Phi$=1.56 eV). The reason is a larger charge separation, hence a larger surface dipole, in the case of the Au^-–Mg^{2+} adsorption.

The change in work function is a direct proof of the formation of an ionic adsorbate and is in principle accessible to experiment. Of course, the magnitude of $\Delta\Phi$ depends on the concentration of the adsorbed species: with a 3×3 supercell (on–top Mg adsorption) $\Delta\Phi$ is 2.37 eV; when the larger 4×4 supercell is used $\Delta\Phi$ decreases to 1.48 V.

Electric field effects

An interesting method to check the presence of a strong asymmetry in the charge distribution of a chemical bond, hence of a large dipole moment, is the response of this dipole to an external uniform electric field. In the limiting case of a neutral adsorbate and absence of surface dipole, the electric field will only induce a polarization of the electron density. In the case of an ionic adsorbate on a conducting substrate, a net dipole results from the formation of an image charge and a strong interaction with the external electric field is expected. These concepts have been developed in the pioneering work of Bagus and co–workers and applied to the study of the ionic nature of atomic adsorbates on metal surfaces.[22,23]

In the presence of a charged adsorbate large changes in the equilibrium geometry can be induced by an external electric field. Consider a uniform electric field F directed normal to the surface in the z direction. The first–order perturbation theory (FOPT) energy is

$$E_{FOPT}(F) = E_{tot}(F = 0) - \mu(F = 0) \cdot F$$

where $\mu(F = 0)$ is the field–free surface dipole. Clearly, a large dipole gives rise to a significant change in potential energy curve, hence in the equilibrium distance. What we have determined is the full response of the system to the presence of the field, including electron polarization effects. The applied fields are in the range of $\pm$0.5 V/Å or 5.0$\times 10^7$ V/cm. For comparison, in semiconductors fields of the order of 10^6 V/cm can be maintained, while fields within the double layer at the electrode–electrolyte interface can reach 10^7 V/cm. Exposed cations in zeolite cavities create fields of 10^8 V/cm (1 V/Å). The upper limit of electric field strength that can be maintained over microscopic distances before field emission or field evaporation takes place is of the order of $\approx$6 V/Å; this is also the field experienced by valence electrons in atoms and molecules. The sign of F is such that F$<$0 attracts electrons from the adsorbate toward the surface.

We first applied a uniform electric field to Au atoms adsorbed on the MgO(100) surface (on top of O adsorption). Here the changes in geometry going from F=0 to F=$\pm$0.5 V/Å are small. For F=$-$0.5 V/Å the Au–O distance increases by 0.02 Å, Table 3.1. This, however, is not due to a displacement of the Au atom but more to the oxide anion that moves downward. Changing the sign of the field, the oxide anion is pushed outside the surface by 0.05 Å; also the Au atom moves slightly outward (but by 0.03 Å, in response to the displacement of the oxygen atom), and the Au–O distance decreases by 0.02 Å only. Thus, the oxide anion of MgO feels the external field much more than the Au adatom, consistent with the basically neutral nature of the adsorbate.

Things are different for MgO ultrathin films. The external electric field has been applied to Au/MgO(2L)/Ag(100) for two cases: Au adsorbed on top of a Mg ion and Au adsorbed in the four fold hollow site, Table 3.1. The most pronounced effect is found when Au is on top of Mg. For F=0, r_{Mg-Au} is 2.594 Å; in a field F=$-$0.5 V the distance reduces to 2.542 Å (Δr=$-$0.052 Å) because the Au atom, negatively charged, is pushed toward the surface. At the same time the Mg cation, positive, moves to a slightly higher position, from 0.452 to 0.480 Å above the surface plane. Notice that the polaronic distortion discussed above is not removed by the

Table 3.1: Changes in position of Au adsorbed on MgO(100) and MgO(2L)/Ag(100) as a function of the presence of an external electric field.

Adsorption site		F=−0.5 V/Å	F=0	F=+0.5 V/Å
	MgO(100)			
On–top O	$r_{Au-O}(\Delta r)$, Å	+0.029	2.270	−0.024
	Δz_O, Å	−0.028	0.0	+0.050
	MgO(2L)/Ag(100)			
On–top Mg	$r_{Au-Mg}(\Delta r)$, Å	−0.052	2.594	+0.094
	Δz_{Mg}, Å	+0.028	0.0	−0.023
Fourfold hollow	$r_{Au-Mg}(\Delta r)$, Å	−0.066	2.810	+0.119
	Δz_{Au}, Å	−0.021	0.0	+0.059

application of the electric field. A field with opposite sign, F=+0.5 V, has an even larger effect: the Au atom moves outward and since there is no repulsion with the surface in this case, r_{Au-Mg} increases to 2.688 Å, with Δr=0.094 Å. The Mg cation moves downward, but only by 0.023 Å, Table 3.1. Similar displacements, although smaller in magnitude, have been found for Au adsorbed on a fourfold hollow site. Here the largest changes are in the shortest Mg–Au distances which go from 2.744 Å (F=−0.5 V/Å), to 2.810 Å (F=0), to 2.927 Å (F=+0.5 V/Å). All these shifts are fully consistent with the presence of a negative Au adsorbate on MgO(2L)/Ag(100).

CO vibrational frequency

CO is largely used as a probe molecule to identify the charge state of a surface site, of a metal atom in a complex or on a surface, of a nanoparticle. In particular, the vibrational frequency of the C–O stretching mode is very sensitive to changes in the electron density of the atoms where the molecule is bound. According to the classical Blyholder model,[24] an increased electron density results in a larger back-donation of charge into the antibonding $2\pi^*$ molecular orbital (MO) of CO and in a considerable redshift of its frequency. For CO on metal surfaces it is well known that the CO frequency (2143 cm^{-1} in the gas phase) is shifted to 1950–2140 cm^{-1} when CO is adsorbed on top, to 1800–2000 cm^{-1} for CO on bridge sites, and to 1700–1900 cm^{-1} for three–hollow sites (see, e.g., Ref. [25]). A large body of data exists for CO adsorbed on Au particles on oxides, and, depending on the nature of the support and on the size of the particles, the frequency is always between 2000

and 2170 cm^{-1}.[26–29] Signals below 2090 cm^{-1} were assigned to negatively charged Au nanoclusters nucleated at defect sites, while values between 2140 and 2100 cm^{-1} are typical of neutral Au clusters. Values higher than 2140 cm^{-1} have been assigned to oxidized gold particles.[26]

In this scenario, CO adsorption can represent a powerful tool to distinguish between Au^0 and Au^- atoms formed on MgO. However, things are somewhat more complex, and the analysis of the vibrational shifts of CO adsorbed on Au adatoms, either neutral or in a negatively charged state, provides some elements of surprise.

We start by considering the vibrational properties of CO adsorbed on Au/MgO/Ag(100) films. The calculations have been performed for Au atoms adsorbed in the fourfold hollow sites of the MgO film. Here all the evidences illustrated above are pointing toward the presence of Au^- anions. The presence of a doubly occupied $6s$ level has a first consequence on the strength of the Au–CO bond: this is very weak due to the strong Pauli repulsion between the diffuse $6s$ orbital and the CO 5σ lone pair. The $5d$ shell of Au is also full, and there are no simple mechanisms to reduce this repulsion by changing the atomic configuration (this is what happens with transition metal atoms in d^9s^1 or d^8s^2 configuration: by CO adsorption the outer s electrons are promoted into the d shell leading to a d^{10}–like species).[30] The result is that the Au–CO distance on MgO/Ag(100) is rather long, 2.23 Å, and the interaction energy is 0.21 eV only. The CO molecule is tilted with respect to the surface normal in order to allow a better overlap of the Au $6s - 5d(z^2)$ hybrid orbital with the CO $2\pi^*$ MO (the Au–C–O internal angle is 124°).

This overlap also results in a substantial charge transfer from Au^- to CO, hence in a large redshift of the CO frequency which becomes 1943 cm^{-1}, i.e., 186 cm^{-1} lower than in the gas phase (2129 cm^{-1} is the computed frequency for free CO). This is a strong indication of the negatively charged nature of supported Au. There are no experimental data available for Au^-–CO gas–phase complexes. However, negatively charged Au clusters have been produced in the gas phase and the vibrational frequency of adsorbed CO has been measured using IR multiple photon dissociation spectroscopy.[31] The smallest cluster produced, Au_3^-–CO shows a CO frequency of 1995 cm^{-1}, with a redshift of 148 cm^{-1}; for larger clusters the redshift is reduced because the charge is delocalized over several Au atoms (e.g., Au_8^-–CO has a CO frequency of 2045 cm^{-1}).[31] Thus, the value calculated here for a supported Au^-–CO complex, 1943 cm^{-1}, is fully consistent with a negative charge localized on a single Au atom.

We have also considered the vibrational properties of CO adsorbed on Au_1/MgO/

Ag(100) in the presence of an external uniform electric field F=±0.5 V/Å. The shifts with respect to the field–free case, F=0, are large: $\Delta\omega$(F>0)=−72 cm^{-1}; $\Delta\omega$(F<0) = +96 cm^{-1}, Table 3.2. They are fully consistent with the occurrence of a substantial charge transfer from Au$^-$ to CO. A positive field moves electrons toward the adsorbate, increases the backdonation, and leads to a strongly redshifted CO frequency, 1871 cm^{-1}. A negative field, which moves charge toward the surface, reduces the backbonding, and results in a frequency of 2039 cm^{-1}, still redshifted compared to free CO (2129 cm^{-1}), Table 3.2. The computed vibrational shifts induced by the field correspond to a tuning rate, $d\omega/dF$, of 336 cm^{-1} (V/Å)$^{-1}$; for comparison, experimental measurements in electrochemical cells for CO on Pd(111)[32] and Pt(111)[33] electrodes give $d\omega/dF$ values of ≈150 and ≈200 cm^{-1} (V/Å)$^{-1}$. Therefore, we can conclude that when CO is bound to Au$_1$/MgO/Ag(100) it feels a higher electron density than when it is adsorbed on transition metal surfaces.

Table 3.2: Field induced vibrational shifts in cm^{-1} for free CO and for CO adsorbed on Au$_1$/MgO/Ag(100).

	CO		CO/Au/MgO(2L)/Ag(100)	
	ω	$\Delta\omega$	ω	$\Delta\omega$
F=−0.5 V/Å	2158	+29	2039	+96
F=+0.5 V/Å	2103	−26	1871	−72
$d\omega/dF$ [cm^{-1} (V/Å)$^{-1}$]	110		336	

At this point one should compare the vibrational frequencies of Au$^-$–CO and Au^0–CO complexes formed on the surface of MgO. The expectation is to find an only slightly shifted frequency for CO adsorbed on neutral Au, around 2100 cm^{-1}. However, things are quite different and a novel and unexpected phenomenon occurs. This has been described in detail in other studies,[34,35] and here we provide only a brief account to compare the results with those of Au$^-$–CO. The adsorption of CO on neutral Au atoms deposited on the MgO(100) surface has the effect to induce a net electron transfer from the singly occupied Au 6s level to the CO 2π^* MO. This net charge transfer occurs because in this way the Pauli repulsion is reduced, and the CO molecule can approach much more closely the gold atom. This results in a stronger interaction (D_e=0.81 eV according to PW91 plane wave calculations) and in a shorter Au–CO distance, 1.99 Å.[35] The Au–C–O tilt angle, 137°, is slightly larger than for Au$^-$. The net electron transfer into the 2π^* MO, well documented by

the spin density analysis, has dramatic consequences on the CO frequency which becomes 1848 cm^{-1}, with a redshift of 281 cm^{-1}.[35] The computed frequency is very close to that measured experimentally at low T for the same system, 1852 cm^{-1}, providing strong support to the theoretical analysis.[34]

It has been proposed that this is a special case of "final state" effect:[34] before CO adsorption the Au atom is in a neutral state, as clearly shown by EPR measurements,[11] but CO adsorption induces a strong chemical modification and a net electron transfer into the $2\pi^*$ antibonding orbital. The consequence is a paradox: the frequency of Au^0–CO formed on MgO, 1848 cm^{-1}, is more redshifted than the frequency of Au^-–CO formed on the same surface, 1943 cm^{-1}! However, there is no contradiction in this result. In fact, in Au^0–CO a full electron is transferred into the $2\pi^*$ MO, formally resulting in a Au^+–CO^- complex. In Au^-–CO the CO molecule cannot get sufficiently close to the Au atom because of the Pauli repulsion so that the overlap is smaller and the charge transfer from Au into the $2\pi^*$ MO of CO is only partial.

The vibrational frequency of adsorbed CO remains a powerful tool to learn about the nature of the supported atoms or clusters: for a correct analysis of the response, however, a sound theoretical interpretation is needed.

Core level shift

X–ray photoemission spectroscopy (XPS) is a powerful technique to study the oxidized or reduced nature of a supported metal particle and some examples have been reported for the specific case of Au nanoparticles on oxide substrates.[36,37] The interpretation of these spectra is not always straightforward as the final core level shift is the result of several contributions, often of opposite sign.[38–40] The simplest and most immediate interpretation of a core level binding energy (CLBE) shift is that a decrease corresponds to a "reduced" species, since extra electronic charge results in a stronger Coulomb potential which acts to destabilize the core levels of the system.

We have determined the CLBEs of the $4f$ levels of supported gold atoms in neutral and "negative" charge states. To this end we have used the densities obtained for Au^0/MgO/Ag(100) (no relaxation) and Au^-/MgO/Ag(100) (polaronic relaxation). We used the Kohn–Sham eigenvalues, $-\varepsilon_i$, as a measure of the CLBEs of supported gold. In this way final state effects are not included. Since we are interested in trends and not in absolute values, the approximation of considering initial

state effects is justified and provides an internally consistent measure of the core level shift.

The ionization of the $4f$ level costs 78.0 eV in Au^0/MgO/Ag(100) and costs 76.1 eV in Au^-/MgO/Ag(100). Thus, going from the formally neutral to the formally charged Au atom there is reduction of the CLBE of 1.9 eV, a very large shift in XPS measurements. The shift is fully consistent with the presence of a negative charge on the Au adatom and further reinforces the analysis obtained with other methods. This shift is in principle accessible experimentally. The problem is, as for other measurements, the very low concentration of deposited atoms, hence the low sensitivity, and the possible interference of other effects such as gold–substrate interactions, formation of small particles, etc.

3.3 Summary

The results presented in the first part of the chapter (STM images of Au and Pd atoms) show the first experimental evidence for the presence of charged Au atoms on a thin, Ag(100)–supported MgO layer as proposed by calculations,[3] in contrast to Au atoms on thick MgO films, which were proven to be neutral. No charging effect is evident from STM data for Pd atoms. As a consequence, while the Au atoms exhibit two–dimensional ordering due to repulsive interactions between the charged entities, no ordering is present for Pd. Besides, a direct comparison between experimenta and simulated STM images prove the charge tranfer from the substrate to the gold atoms. The observation of the charging of Au adsorbed on a thin MgO film is a direct consequence of the work function reduction of the metal substrate by the thin film, and depends critically on the electron affinity of the adsorbed metal. The experimental verification of this hypothesis associates credibility to the proposal to use combinations of various thin oxide films and deposited metals to tune surface reactivity.

In addition, in the second section we have also considered in detail the different properties of neutral Au atoms deposited on the MgO(100) surface, and those of negatively charged Au anions formed on MgO/Ag(100) thin films (includin simulated SYM images). Using a variety of properties, some of them directly related to measurable quantities, we have been able to clearly show that the two species give rise to very characteristic and distinct behaviors which are indicative of the neutral or anionic nature of the adatom. While a single evidence may not be sufficient to

conclude about the presence of neutral or anionic gold, the combination of a number of properties provides a convincing proof of the nature of the adsorbate.

We believe that the methods and measurements described above do not apply exclusively to the case of Au atoms on MgO surface, but provide a general framework to identify ionic adsorbates on surfaces.

Bibliography

[1] B. Yoon *et al.*, *Science* **307** (2005), p. 403.

[2] M. Sterrer *et al.*, *Angew. Chem., Int. Ed.* **45** (2006), p. 2630.

[3] G. Pacchioni, L. Giordano, and M. Baistrocchi, *Phys. Rev. Lett.* **94** (2005), p. 226104.

[4] D. Ricci, A. Bongiorno, G. Pacchioni, and U. Landman, *Phys. Rev. Lett.* **97** (2006), p. 036106.

[5] L. Giordano and G. Pacchioni, *Phys. Chem. Chem. Phys.* **8** (2006), p. 3335.

[6] M. Yulikov *et al.*, *Phys. Rev. Lett.* **96** (2006), p. 146804.

[7] J. Repp *et al.*, *Phys. Rev. Lett.* **85** (2000), p. 2981.

[8] N. Knorr *et al.*, *Phys. Rev. B* **65** (2002), p. 115420.

[9] J. Tersoff, D. R. Hamann, *Phys. Rev. Lett.* **50** (1983), p. 1998.

[10] J. Repp, G. Meyer, F. E. Olsson, and M. Persson, *Science* **305** (2004), p. 493.

[11] M. Yulikov, M. Sterrer, M. Heyde, H. P. Rust, T. Risse, H.-J. Freund, G. Pacchioni, and A. Scagnelli, *Phys. Rev. Lett.* **96** (2006), p. 146804.

[12] A. Del Vitto, G. Pacchioni, F. Delbecq, and P. Sautet, *J. Phys. Chem. B* **109** (2005), p. 8040.

[13] M. Chiesa, E. Giamello, C. Di Valentin, G. Pacchioni, Z. Sojka, and S. Van Doorsiaer, *J. Am. Chem. Soc.* **127** (2005), p. 16935.

[14] M. Sterrer, F. Fishbach, T. Risse, and H. J. Freund, *Phys. Rev. Lett.* **94** (2005), p. 186101.

[15] M. Sterrer, M. Heyde, M. Novicki, N. Nilius, T. Risse, H.-P. Rust, G. Pacchioni, and H.-J. Freund, *J. Phys. Chem. B* **110** (2006), p. 46.

[16] W. Maus-Friedrichs, S. Dieckhoff, and V. Kempter, *Surf. Sci.* **249** (1991), p. 149.

[17] R. J. Mulliken, *J. Chem. Phys.* **23** (1955), p. 1833.

[18] R. F. W. Bader, *Atoms in Molecules: A Quantum Theory* (Clarendon, New York, 1994).

[19] K. H. Kingdom and I. Langmuir, *Phys. Rev.* **21** (1923), p. 380.

[20] R. W. Gurney, *Phys. Rev.* **47** (1935), p. 479.

[21] A. Zangwill, *Physics at Surfaces* (Cambridge University Press, Cambridge, 1988).

[22] L. G. M. Pettersson and P. S. Bagus, *Phys. Rev. Lett.* **56** (1986), p. 500.

[23] P. S. Bagus, G. Pacchioni, and M. R. Philpott, *J. Chem. Phys.* **90** (1989), p. 4287.

[24] G. Blyholder, *J. Phys. Chem.* **68** (1964), p. 2772.

[25] N. Sheppard and T. T. Nguyen, in *Advances in Infrared and Raman Spectroscopy*, edited by R. E. Hester and R. J. H. Clark (Heyden, London, 1978), Vol. 5, p. 67 and references therein.

[26] F. Boccuzzi, A. Chiorino, M. Manzoli, D. Andreeva, and T. Tabakova, *J. Catal.* **188** (1999), p. 176.

[27] B. Yoon, H. Häkkinen, U. Landman, A. S. Wrz, J. M. Antonietti, S. Abbet, K. Judai, and U. Heiz, *Science* **307** (2005), p. 403.

[28] A. S. Wörz, U. Heiz, F. Cinquini, and G. Pacchioni, *J. Phys. Chem. B* **109** (2005), p. 18418.

[29] R. Meyer, C. Lemire, S. K. Shaikhutdinov, and H. Freund, *Gold Bull.* **37** (2004), p. 72.

[30] G. Pacchioni and N. Rösch, *Acc. Chem. Res.* **28** (1995), p. 390.

[31] A. Fielicke, G. van Helden, G. Meijer, B. Simard, and D. M. Rayner, *J. Phys. Chem. B* **109** (2005), p. 23935.

[32] S. Zou, R. Gomez, and M. J. Weaver, *J. Electroanal. Chem.* **474** (1999), p. 155.

[33] A. Rodes, R. Gomez, J. M. Feliu, and M. J. Weaver, *Langumir* **16** (2000), p. 811.

[34] M. Sterrer, M. Yulikov, T. Risse, H.-J. Freund, J. Carrasco, F. Illas, C. Di Valentin, L. Giordano, and G. Pacchioni, *Angew. Chem., Int. Ed.* **45** (2006), p. 2633.

[35] L. Giordano, J. Carrasco, C. Di Valentin, F. Illas, and G. Pacchioni, *J. Chem. Phys.* **124** (2006), p. 174709.

[36] J. Radnik, C. Mohr, and P. Claus, *Phys. Chem. Chem. Phys.* **5** (2003), p. 172.

[37] A. Zwijnenburg, A. Goossens, W. G. Sloof, M. W. J. Craj, A. M. van der Kraan, L. J. De Jongh, M. Makkee, and J. Moulijn, *J. Phys. Chem. B* **106** (2002), p. 9853.

[38] P. S. Bagus and G. Pacchioni, *Phys. Rev. B* **48** (1993), p. 15262.

[39] S. Lizzit, A. Baraldi, A. Grosso, K. Reuter, M. V. Ganduglia-Pirovano, C. Stampfl, M. Scheffler, M. Stichler, C. Keller, W. Wurth, and D. Menzel, *Phys. Rev. B* **64** (2001), p. 205419.

[40] P. S. Bagus, F. Illas, G. Pacchioni, and F. Parmigiani, *J. Electron Spectrosc. Relat. Phenom.* **100** (1999), p. 215.

CHAPTER 4

Charge transfer and enhancement of the magnetic moment[†]

Continuous miniaturization is driving the data–storage technology down to the nanometer scale. The magnetic behavior of metal clusters is particularly intriguing because in gas phase they possess higher magnetic moments than the corresponding bulk metals[1] or exhibit complex magnetic orderings.[2] However, any practical application of magnetic clusters implies to deposit and stabilize them on a substrate, either a metal or an insulator, or to form cluster–assembled materials.[3] Usually, the interaction of clusters with the support results in a partial quenching of their magnetic moment.[4–7] On a metallic support this is due to the hybridization of the cluster and the support states at the interface[4] while on an insulating oxide it originates from the fact that some filled spin–majority states of the cluster are shifted to higher energies and the electrons fill the empty states close to the Fermi level E_F, which are predominantly composed of spin minority states.[5–7] A similar effect is induced by organic ligands surrounding a magnetic particle,[8] and the surface can be seen as a special kind of "ligand". Here we report on the possibility to modify the cluster magnetic moments by depositing them on ultrathin oxide films grown on a mag-

[†]The results described in this Chapter have been reported in: *U. Martinez*, G. Pacchioni, F. Illas, *The Journal of Chemical Physics* **130** 184711 (2009)

netic metal.

In the previous chapter we reported the charging of gold atoms deposited on ultrathin MgO films epitaxially grown on a metal . An interesting question is if this kind of electronic communication may produce observable consequences also on the magnetic properties of the supported cluster. To this end we have performed density functional theory DFT calculations on the structure and magnetization of Fe clusters containing two to six atoms deposited on a two–monolayer MgO film on a metal and on the bare MgO(100) surface. MgO films have been prepared on Ag(100), Fe(100), and Mo(100) and induce a substantial reduction in the metal work function depending on the metal (see section 1.3). For MgO/Mo(100) this change is of 2.1 eV, for MgO/Fe(100) of 1.9 eV, while for MgO/Ag(100) it is of 1.2 eV. However, Ag and Mo are nonmagnetic metals and the magnetic properties of a supported Fe cluster could be different on a MgO film grown on a magnetic metal like Fe. Indeed, in this study we show that for Fe clusters deposited on MgO/Fe(100) films there is an enhancement of the cluster magnetic moment compared to MgO/Mo(100) films and to bare MgO(100). This arises mostly from the Fe atoms of the cluster at the interface and its origin is a partial charge transfer from the Fe cluster to the metal/oxide interface.

4.1 Computational Details

The calculations has been performed with the VASP code (see Sec. 2.1.1, pag. 25). The kinetic energy cutoff has been set to 400 eV. A vacuum of at least 10 Å separates the slabs and a dipole correction has been applied. The Mo(100) and Fe(100) substrates have been modeled by four atomic layers. The 2 ML MgO film has been adapted to the Mo(100) and Fe(100) lattice parameters. For Mo (a_0=3.151 Å; a_0(exp.) =3.147 Å) this implies an expansion of 5%; for Fe (a_0=2.840 Å; a_0(exp.)=2.866 Å) a contraction of 5%. The O atoms of MgO are on top of the metal atoms while Mg falls in hollow positions. The 2 ML films on Mo(100) used here represent a somewhat idealized situation. In fact, at this film thickness MgO on Mo(100) forms Moiré patterns due to the lattice mismatch with the metal support.

Fe$_n$ clusters ($2 \leq n \leq 6$) have been deposited on these ultrathin films and, for comparison, on a 3 ML unsupported MgO film which well represents a bare MgO(100) surface.[9,10] The initial structure of the clusters is that used in Ref.[6] after careful search of various isomers. All atoms of the Fe clusters, of the MgO film, and

in the two top layers of Mo and Fe were relaxed until the atomic forces are less than 0.01 eV/Å. The remaining two metal layers were frozen at bulk positions. For the calculations we used 3×3 supercells containing 9 Mg, 9 O, and 9 Mo or Fe atoms per layer. Based on direct experience with the calculations of supported clusters on oxide thin films we believe that this supercell size is sufficient to avoid interaction between cluster images. Sampling of the Brillouin zone using a 4×4×1 k–point mesh resulted in a converged total energy.

4.2 Results and Discussion

4.2.1 Fe_2

We start with the properties of the Fe dimer. Gas–phase Fe_2 has a magnetic moment of 3 μ_B per atom corresponding to a $^7\Delta_u$ ground state.[11] When supported on MgO(100) the molecule lies flat with the Fe atoms close to the O ions of the surface and is bound by 1.75 eV, Table 4.1. On MgO(100) Fe_2 maintains the magnetization, Figure 4.1 and Table 4.2, despite a slightly longer Fe–Fe distance than in gas phase, 2.05 Å versus 1.98 Å, Figure 4.2. The Bader analysis shows that there is virtually no charge transfer between Fe_2 and MgO(100), Figure 4.1, in agreement with previous studies.[6] The bonding is due to the hybridization of the Fe_2 states with the O 2p states of the oxide support. On the MgO/Mo(100) film Fe_2 occupies the same position but the Fe–Fe distance is considerably elongated, 2.19 Å, Figure 4.2, while the Fe–O distance is reduced by 0.12 Å with respect to the bare surface 1.87 Å versus 1.99 Å. This structural change, which is common also to other clusters considered, reflects the stronger bonding of the Fe dimer to the MgO/Mo(100) film, Table 4.1. Also in this case the Bader analysis shows that there is virtually no charge transfer, Figure 4.1. The main reason of the stronger bonding is not the presence of the Mo support but the larger lattice parameter of the MgO film. In fact, on a 5% expanded MgO 3 ML film the properties of supported Fe_2 are very similar to those of Fe_2/MgO/Mo(100). The lattice expansion in MgO results in a lower Madelung potential and a higher reactivity of the oxide anions.[12] Despite the stronger bonding at the interface, the net magnetic moment of Fe_2 on MgO/Mo(100) is the same as in gas phase or on bare MgO, Figures 4.1 and 4.3.

On MgO/Fe(100) the geometry of Fe_2 is identical to that found for MgO(100), Figure 4.2, but the binding energy is considerably smaller, 1.13 eV versus 1.75 eV, Table 4.1. Again, the large change in adsorption energy reflects the compressed lat-

Table 4.1: Properties of gas phase and supported Fe_n clusters.

	E_{ad} (eV)			$< d(Fe-O) >$ (Å)		
	MgO	MgO/Mo	MgO/Fe	MgO	MgO/Mo	MgO/Fe
Fe_2	1.75	2.64	1.13	1.99	1.87	1.99
Fe_3	2.28	3.22	2.14	1.94	1.87	1.96
Fe_4	2.29	3.12	2.49	2.03	1.94	2.00
Fe_5	2.68	3.58	2.51	2.13	1.97	2.04
Fe_6	2.47	3.61	2.27	2.01	1.93	2.05

tice constant in the MgO film: on an unsupported and 5% compressed MgO 3 ML film Fe_2 is bound by 1.24 eV and the magnetization is that of gas phase. The role of the Fe metal support becomes clear when we consider the magnetic properties. The magnetic moment of Fe_2 on a MgO/Fe(100) film is in fact 3.22 μ_B per atom, Figure 4.1, with a net increase of 0.4 μ_B for the entire cluster compared not only to MgO(100) and MgO/Mo(100) but even to free Fe_2, Figure 4.3. The origin of the enhanced magnetic moment is that the electron density on Fe atoms is depleted by $0.11e$ per atom. The projected density of states (DOS), Figure 4.4, shows that a spin minority state of Fe_2 with mainly $3d$ character is crossed by the Fermi level on MgO/Fe(100) at variance with MgO(100) or MgO/Mo(100) where the state is below E_F. Electrons flow from this minority spin state to the metal/oxide interface,

Table 4.2: Avarage magnetic moment of gas phase and supported Fe_n clusters. The local magnetic moment is determined from the spin density using Bader analysis.

	Gas phase	MgO	MgO/Mo	MgO/Fe
Fe_2	3.00	3.02	3.03	3.22
Fe_3	3.33	2.68	2.68	2.81
Fe_4	3.00^a–3.50^b	2.54	2.54	2.74
Fe_5	3.20^a–3.60^b	3.16	2.75	2.97
Fe_6	3.33	2.98	2.97	3.04

[a] Low spin state

[b] High spin state

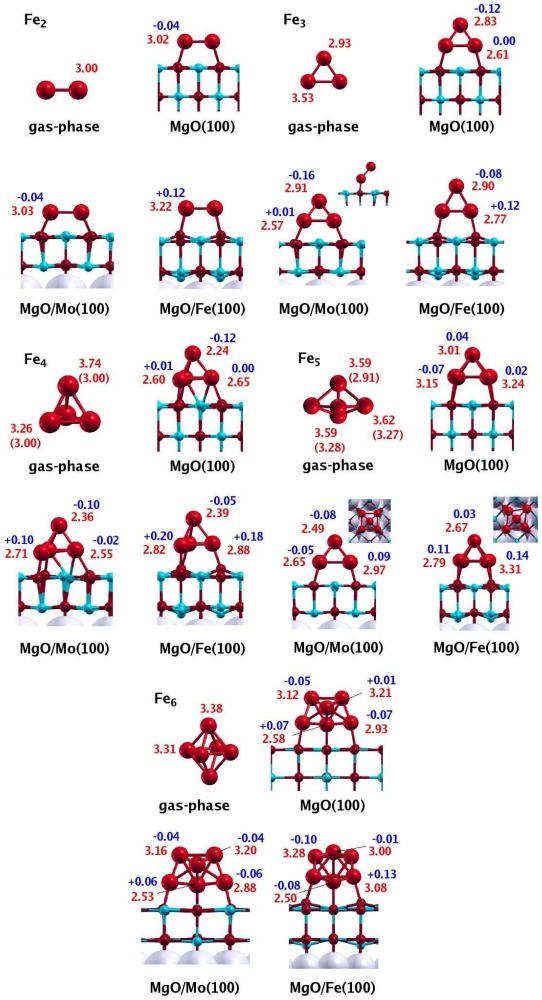

Figure 4.1: Side views of Fe_n clusters in gas phase and adsorbed on MgO(100), MgO/Mo(100), and MgO/Fe(100) surfaces. Numbers in red and blue are the magnetic moments and the net Bader charges, respectively, of individual atoms in the cluster. Adsorbed Fe_3 is tilted with respect to the surface normal by 41° on MgO(100), 54° on MgO/Mo(100), and 13° on MgO/Fe(100). Fe_5 on MgO/Mo(100) is a square pyramid while on MgO/Fe(100) the basal plane is rhombic.

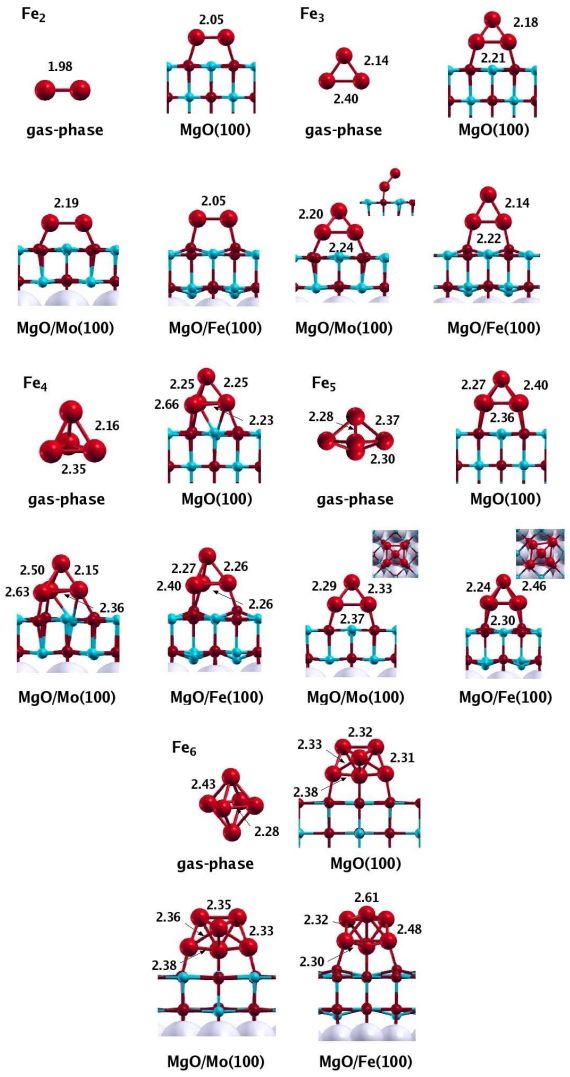

Figure 4.2: Selected Fe–Fe distances of Fe_n clusters in gas phase and adsorbed on MgO(100), MgO/Mo(100), and MgO/Fe(100).

resulting in a larger spin polarization. Thus, the charge transfer is not due to the change in lattice parameter of the oxide film but to the metal underneath: on a 5% compressed MgO 3 ML film Fe_2 is neutral and has the same magnetization as on

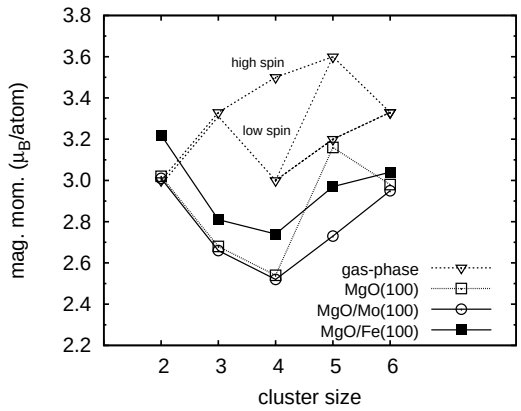

Figure 4.3: Average magnetic moment per atom vs cluster size for gas–phase Fe_n clusters and for Fe_n clusters supported on MgO(100), MgO/Mo(100), and MgO/Fe(100) surfaces. For gas–phase Fe_4 and Fe_5 two values of the magnetic moment are reported as high spin and low spin nearly degenerate states exist (see text).

the bare MgO(100) surface. The charge transfer is accompanied by a non–negligible polaronic distortion of the MgO film, clearly visible in Figure 4.2, consisting of the protrusion of the oxide anions of the MgO film toward the Fe atoms of the dimer; at the same time the Mg cations underneath in the bottom layer relax toward the Fe(100) support, Figure 4.2. In order to evaluate the role of the magnetic structure of the Fe support on the induced charge transfer, we have considered two situations where the magnetic moments of the Fe_2 unit are ferro– or antiferromagnetically coupled to those of the Fe(100) metal support. The enhancement of the local magnetic moment in Fe_2 is found in both cases, indicating that this does not depend on the structure of the majority and minority components of the DOS of the Fe(100) support. We also found that the state where the moments of Fe_2 are antiferromagnetic coupled to those of Fe(100) is more stable by 0.58 eV. However, since the enhancement of magnetization in Fe_2 is found for both magnetic orderings, the rest of the discussion refers to Fe clusters ferromagnetically coupled to the Fe(100) substrate.

4.2.2 Fe_3

Fe_3 has a triangular shape both in gas phase and on MgO(100) where the cluster plane forms an angle of 41° from the surface normal, Figure 4.2. The interaction has dramatic consequences on the magnetization. In fact, free Fe_3 has an average mag-

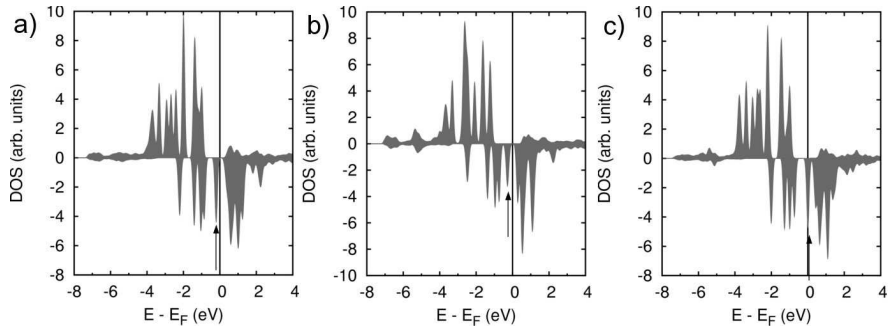

Figure 4.4: Spin–polarized DOS of Fe_2 adsorbed on (a) MgO(100), (b) MgO/Mo(100), and (c) MgO/Fe(100). The arrow indicates a spin minority state of Fe_2 with mainly $3d$ character which on MgO and MgO/Mo lies below the Fermi level. On MgO/Fe the level is crossed by the Fermi level, indicating depletion of electronic charge from this state.

netization of 3.33 μ_B per atom, 10% higher than Fe_2. As reported by Sljivancanin and Pasquarello,[6] on MgO(100) the cluster magnetic moment is strongly quenched and becomes 2.68 μ_B per atom in average, with the atoms at the interface having a smaller magnetization than the apical atom. The binding energy is 2.28 eV and the Fe–O distance is 1.94 Å. On MgO/Mo(100) the interface bonding is 1 eV stronger, 3.22 eV, and the interface distance is shorter, 1.87 Å, Table 4.1 for the reasons illustrated above, but the average magnetic moment is virtually the same found on MgO(100) with a strong reduction compared to gas–phase Fe_3. In neither MgO(100) nor the MgO/Mo(100) film we found evidence of significant charge transfer. In particular, the two Fe atoms at the interface are neutral, while a small and similar charge accumulation is found on the apical atom, Figure 4.1. Things change when we consider Fe_3 on MgO/Fe(100). Both the geometry and the adsorption energy are similar to those found on bare MgO, Figure 4.2. However, as for Fe_2, the average magnetic moment per atom is larger, 2.81 μ_B. Also in this case we found a depletion of charge on the Fe atoms, especially for those at contact with the oxide film, and a corresponding enhancement of their magnetic moments, see Figure 4.1 and Table 4.2.

4.2.3 Fe_4 and Fe_5

The next two clusters, Fe_4 and Fe_5, have a common feature: in gas phase they both exhibit two nearly degenerate electronic states with different total magneti-

zation. Fe_4 is a distorted tetrahedron; the ground state has 14 unpaired electrons (average of 3.5 μ_B per atom) but is separated by 16 meV only from a state with 12 unpaired electrons (3.0 μ_B per atom); Fe_5 is a distorted trigonal bipyramid and exhibits a high spin state with 18 unpaired electrons (3.6 μ_B per atom) separated by 7 meV only from a low spin state with 16 unpaired electrons (3.2 μ_B per atom). While the existence of two states for gas–phase Fe_5 has been reported previously,[13] we are not aware of a similar situation for Fe_4. Given the intrinsic accuracy of the calculations, the two spin states in Fe_4 and Fe_5 must be considered as degenerate.This is no longer the case when clusters are supported on MgO(100). For both Fe_4 and Fe_5 there is a net decrease in the average magnetic moment, Figures 4.1 and 4.3. For Fe_4, however, the low spin state is definitely more stable, and the magnetic moment is of 2.54 μ_B per atom. The quenching is very large if referred to the high spin Fe_4 isomer, while it is in line with that found for Fe_3 if the low spin state is considered, Figure 4.3. For Fe_5 the situation is reversed, and only the high spin state is stable on the MgO(100) surface with an average magnetization of 3.16 μ_B per atom. Again, the quenching is in line with that of Fe_3 or Fe_4 if referred to free Fe_5 in high spin configuration, while it presents an anomalous high value of the magnetization no quenching if compared to low spin Fe_5, Figure 4.3. Attempts to converge on other spin states of Fe_4 and Fe_5 supported on MgO(100) failed, suggesting the existence of a single stable supported isomer. Notice that the strong oscillation in the curve of the average magnetization versus cluster size observed for Fe clusters on MgO(100), Figure 4.1, closely reproduces that reported in Ref.[6]; however, the finding of two degenerate spin states for the free clusters changes substantially the physical picture. The extent of the magnetic quenching in Fe_3, Fe_4, and Fe_5 is in fact rather similar, and its origin is that described above and in Ref.[6]. In fact, also for Fe_4 and Fe_5 the charge transfer between the cluster and the oxide surface is negligible, Figure 4.1.

When we deposit Fe_4 on a MgO/Mo(100) film we obtain similar results as for the bare MgO(100) surface: same structure and average magnetization despite the stronger bonding and shorter interface distance, Figure 4.1 and Table 4.2. On the contrary, due to the strong adsorption energy, things change for Fe_5 on MgO/Mo(100): here only the low spin state exists and attempts to locate a high spin isomer failed. The magnetic quenching is in line with that found for the smaller clusters once it is referred to the low spin gas–phase Fe_5 isomer. Again, no charge transfer but only an internal charge redistribution occurs in supported Fe_5, Figure 4.1. The behavior of Fe_4 and Fe_5 deposited on a MgO/Fe(100) film parallels that of the two clusters

on MgO/Mo(100) except for the net magnetic moment that is increased, Figure 4.3. For both Fe_4 and Fe_5 the low spin state is preferred, and the Fe_4 average magnetic moment goes from 2.54 μ_B per atom in MgO/Mo to 2.74 μ_B per atom in MgO/Fe and for Fe_5 from 2.75 μ_B per atom in MgO/Mo to 2.97 μ_B per atom in MgO/Fe. The effect is even more pronounced if one restricts the analysis to the Fe atoms at direct contact with the oxide film. On MgO/Fe(100) these atoms show in fact a large enhancement of the magnetization compared to the same atoms of the MgO/Mo(100) supported clusters. The increase in magnetic moment has the same origin discussed for Fe_2, i.e., a substantial flow of charge from a cluster spin minority state to the metal/oxide interface.

4.2.4 Fe_6

The last case considered is that of Fe_6, which in gas phase has an octahedral shape. Both our results and the literature data[6,13] agree on the existence of a single isomer with 20 unpaired electrons (3.33 μ_B per atom). On MgO(100) and MgO/Mo(100) the cluster magnetic moment is reduced by the same amount (2.98 μ_B per atom in Fe_6/MgO(100) and 2.97 μ_B per atom in Fe_6/MgO/Mo (100)). On MgO/Fe(100), however, the quenching is slightly smaller and the average magnetization is of 3.04 μ_B per atom, corresponding to a net increase of 0.4–0.5 μ_B for the whole cluster, Figure 4.1. Fe_6 is bound to the oxide surface with only three Fe atoms and the charge transfer is less pronounced than, for instance, in Fe_5. More important, the weak interaction with the MgO/Fe(100) substrate, 2.27 eV versus 3.61 eV on MgO/Mo(100), results in a different structure, Figure 4.2. Thus, besides the electronic effects considered before, here we also have the interplay of structural effects that contribute to a reduction in the magnetization. Still, on the Fe(100) supported MgO film Fe_6 exhibits a higher magnetic moment than on MgO/Mo(100) or on the bare MgO surface, indicating that the enhancement is a rather general effect, Figure 4.3.

4.3 Summary

As reported in the literature, Fe clusters deposited on a MgO surface undergo a magnetic quenching;[6] the size of this quenching is rather constant if one considers that for some cluster sizes two degenerate spin states exist. In this work we have shown that on MgO ultrathin films (two layers) grown on Mo(100) the magnetic

quenching parallels that found on the bare MgO(100) surface, although there are cases, e.g., Fe_5, where different spin configurations are stabilized because of the different strengths of the cluster–oxide bond. However, when the MgO films are grown on Fe(100), charge flows from the cluster to the support leading to a depletion of charge on the Fe atoms of the cluster at the interface, resulting in an enhanced magnetic moment.

The mechanism observed is different from what was reported in other studies on the enhancement of the magnetization on surface layers of Fe metal upon oxygen adsorption.[14–16] It has been suggested that adsorbed oxygen atoms on the Fe(100) surface or in subsurface sites withdraw electrons from the Fe top layers and increase the local magnetic moments. At a completely O covered surface, the magnetic moment of Fe has a value comparable to that of the antiferromagnetic Fe oxides. A partial magnetization is present also on the oxygen atoms. The effect is thus related to the creation of a thin layer of iron oxide which starts to exhibit the typical properties of magnetic insulators. On the contrary, in the case presented here the MgO layer is not involved in the oxidation of the supported clusters (no formation of iron oxides) and the charge flows from the metallic Fe clusters to the metal-oxide interface by electron tunneling. This means that the effect is expected to be reinforced on one–layer films and to decrease in a regular way with increasing film thickness.[9,17] The change in magnetic moment of supported Fe clusters represents another example of specific properties of ultrathin films and could open new perspectives in the design of magnetic nanostructures by exploiting the potential offered by these systems to engineer materials with novel and unprecedented properties.[18,19]

Bibliography

[1] S. E. Apsel, J. W. Emmert, J. Deng, and L. A. Bloomfield, *Phys. Rev. Lett.* **76** (1996), p. 1441.

[2] S. N. Khanna, B. K. Rao, P. Jena, and M. Knickelbein, *Chem. Phys. Lett.* **378** (2003), p. 373.

[3] S. A. Claridge, A. W. Castelman, S. N. Khanna, C. B. Murray, A. Sen, and P. S. Weiss, *ACS Nano* **3** (2009), p. 244.

[4] K. Wildberger, V. S. Stepanyuk, P. Lang, R. Zeller, and P. H. Dederichs, *Phys. Rev. Lett.* **75** (1995), p. 509.

[5] L. Giordano, G. Pacchioni, A. M. Ferrari, F. Illas, and N. Rösch, *Surf. Sci.* **473** (2001), p. 213.

[6] Z. Sljivancanin and A. Pasquarello, *Phys. Rev. Lett.* **90** (2003), p. 247202.

[7] M. Moseler, H. Häkkinen, and U. Landman, *Phys. Rev. Lett.* **89** (2002), p. 176103.

[8] D. A. van Leeuwen, J. M. van Ruitenbeek, L. J. de Jongh, A. Ceriotti, G. Pacchioni, O. D. Häberlen, and N. Rösch,, *Phys. Rev. Lett.* **73** (1994), p. 1432.

[9] G. Pacchioni, L. Giordano, and M. Baistrocchi, *Phys. Rev. Lett.* **94** (2005), p. 226104.

[10] S. Schintke, S. Messerli, M. Pivetta, F. Patthey, L. Libioulle, M. Stengel, A. De Vita, and W.-D. Schneider, *Phys. Rev. Lett.* **87** (2001), p. 276801.

[11] M. Tomonari and H. Tatewaki, *I. Chem. Phys.* **88** (1998), p. 1828.

[12] G. Pacchioni, J. M. Ricart, and F. Illas, *J. Am. Chem. Soc.* **116** (1994), p. 10152.

[13] G. Rollmann, P. Entel, and S. Sahoo, *Comput. Mater. Sci.* **35** (2006), p. 275.

[14] S. R. Chubb and W. E. Pickett, *Phys. Rev. Lett.* **58** (1987), p. 1248.

[15] P. Blonski, A. Kiejna, and J. Hafner, *Surface Science* **590** (2005), p. 88.

[16] S. J. Jenkins, *Surface Science* **600** (2006), p. 1431.

[17] P. Frondelius, A. Hellman, K. Honkala, H. Häkkinen, and H. Gronbeck, *Phys. Rev. B* **78** (2008), p. 085426.

[18] H. J. Freund and G. Pacchioni, *Chem. Soc. Rev.* **37** (2008), p. 2224.

[19] C. Freysoldt, P. Rinke, and M. Scheffler, *Phys. Rev. Lett.* **99** (2007), p. 086101.

Part II

Thin oxide films as molecular sieves

CHAPTER 5

Realization of an atomic sieve[†]

The adsorption properties of solid surfaces are dominated by the chemical and physical nature of the topmost atomic layer, with sub–surface layers contributing only weakly. This adsorption behavior is usually unspecific in terms of admitting only selected molecular species for binding or in determining well–defined interaction sites on the surface. A much higher degree of surface functionality is common to all biological systems, where foreign species are repelled at the inert surface of a membrane and are allowed to interact only at specific pores and channels. A simplified concept of this has been transferred to material science, where a size–selective interaction mechanism was realized for three–dimensional zeolite and silicate structures.[1–3] The decisive parameter in the process is the pore size of the –Si–Al–O– network, which controls whether a reactant penetrates the opening and propagates to the reaction site or not. Typical pore sizes in zeolites can be adjusted between 1–50 nm, this being an ideal diameter for the fabrication of molecular sieves.

To the best of our knowledge, no two–dimensional counterpart for a molecular sieve has been produced so far that would be able to control the access of an atomic/molecular species to a reactive subsurface region via nanopores in the inert

[†]The results described in this Chapter have been reported in: S. Ulrich, N. Nilius, H-J Freund, *U. Martinez*, L. Giordano and G. Pacchioni *ChemPhysChem* **92** 1367 (2008) and S. Ulrich, N. Nilius, H-J Freund, *U. Martinez*, L. Giordano, G. Pacchioni, *Surface Science* **603** 1145 (2009)

top layer. A selective interaction characteristic would have interesting applications in heterogeneous catalysis, as reaction processes could be steered via the size of the reactants with respect to the openings in the top layer.

A promising candidate for size-specific adsorption is the ultra–thin SiO_2 film on Mo(112), described in details in Section 1.3.3 page 16. The film is build up by a network of six–membered SiO rings, which is interrupted by eight–membered rings along line defects. These ring openings give access to the Mo(112) support, which is considerably more reactive than the inert silica layer. According to theoretical predictions,[4] the possibility to attach adsorbates to the Mo–SiO_2 interface may depends on their effective diameters. In this chapter is demonstrated such size–specific adsorption characteristics of the SiO_2 film by employing scanning tunneling microscopy (STM) and density functional theory (DFT) investigating the binding behavior of Pd, Ag and Au atoms onto SiO_2/Mo(112). While Pd and Ag atoms are able to penetrate the openings in defect–free oxide patches, Au atoms are too large and only bind at SiO_2 line defects. The relevant parameter that governs the energy barrier for passing the holes in the oxide film has not been identified yet for the different atoms. In a first, intuitive picture, it might be connected to the atom size with respect to the pore diameter. We will also show that this approach is too simple and metal atoms of comparable size have different penetration probabilities. The three species are chosen, because they either exhibit comparable van der Waals radii (Pd and Au) or similar electronic properties (Au and Ag). The derived binding characteristic demonstrates that the probability for an adatom to pass the holes in the silica top–layer is governed by its electronic structures, in particular by the spatial extension and electron filling of its valence orbitals.

5.1 Computational and Experimental Details

Computational Details

Spin–polarized DFT calculations has been performed with the VASP code (see section 2.1.1, page 25). The kinetic energy cutoff has been set to 400 eV. A vacuum of at least 10 Å separates the slabs and a dipole correction has been applied. The regular sites in the silica film are modeled with a (4×2) super–cell containing 7 Mo layers ($Mo_{56}Si_8O_{20}$), a (5×2) cell with 4 Mo layers is used for the line defect ($Mo_{40}Si_{10}O_{25}$) and a (6×4) cell fot the simulated STM images ($Mo_{96}Si_{24}O_{60}$). Penetration barriers are determined by moving the metal atom along the surface normal into the oxide

pore and relaxing the metal/oxide complex for each vertical distance. The computed barriers do not correspond to a real transition state and slightly overestimate the actual barrier height. Topographic STM images are simulated using the Tersoff–Hamann approach.[5]

Experimental Details

The experiments are carried out in a custom–build, ultra-high vacuum STM operated at 10 K. Imaging is performed in the constant current mode, whereas the sample electronic properties are deduced from differential conductance (dI/dV) measurements applying lock–in technique. According to the Tersoff–Hamann theory for vacuum tunneling[5] the dI/dV signal provides a measure for the local density of electronic states (LDOS) in the sample.

The SiO_2 film is prepared by depositing 1.2 ML Si in 1×10^{-7} mbar O_2 onto a Mo(112) surface pre–covered with oxygen and annealing the sample to 1200 K. Single Pd, Ag and Au atoms are deposited from three different mini–evaporators consisting of the respective high–purity wires wrapped around a tungsten filament. Although atom deposition has been performed at 20 K sample temperature, the thermal energy of the incoming atoms ensures transient diffusion into their equilibrium adsorption sites.

5.2 Results and Discussion

STM topographic images of the film exhibit a honeycomb structure with protrusions located at each corner of the interlocked hexagons (Figure 5.1a). Each maximum represents the silicon atom of a SiO_4 tetrahedron, which is connected to three neighboring silicon atoms via bridging oxygen atoms. The fourth oxygen atom located below the silicon sits in a bridge position of the $[\bar{1}\bar{1}1]$ oriented rows of Mo(112) and anchors the film to the support. The –Si–O– hexagons enclose a hole of 5 Å in size that opens into a nanopore at the Mo–SiO_2 interface. The major structural defects of the film are $[\bar{1}10]$–oriented antiphase domain boundaries (APDB), formed by an alternation of eight– (hole size: 5×8 Å^2) and four–membered rings (see arrows in Figure 5.1a).

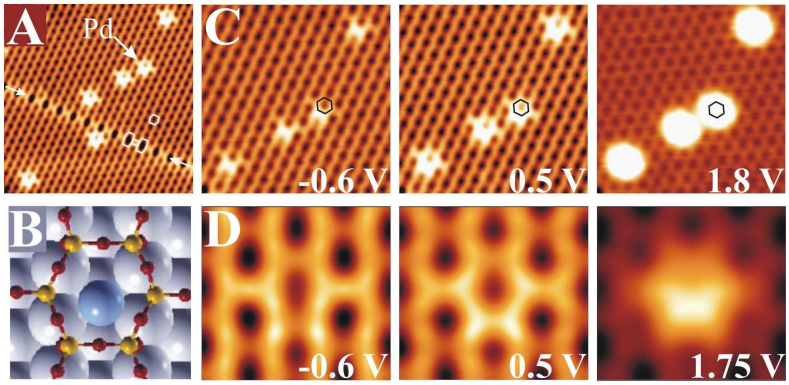

Figure 5.1: (a) STM image (0.5 V, 13×13 nm^2) of 0.1 ML Pd on SiO_2 on Mo(112). (b) Structure model of the Pd adsorption site. Bias dependence of the topographic contrast of Pd atoms in (c) experimental (5×5 nm^2) and (d) simulated STM images (1.8×1.6 nm^2, 6×4 supercell).

5.2.1 Pd adsorption

Adsorption of 0.05 ML of Pd leads to distinct changes in topographic images of the SiO_2 film (Figure 5.1a). In contrast to earlier experiments, no protruding features are observed that could be associated to single Pd atoms bound to the oxide surface.[6–8] Instead, selected structural elements of the SiO_2 network appear bright, indicating that Pd–induced modifications in the oxide LDOS, and not the adatom itself, are responsible for the contrast change. This assumption is supported by the pronounced bias dependence of the topographic features associated with Pd (Figure 5.1c, left to right). At negative sample bias (occupied states), the adatom affects only the lower section of a SiO hexagon. At small positive bias, the contrast extends over a larger part of the ring, leading to the emergence of hexangular stars with dark central regions. With further bias increase, the bright contrast gradually moves from the edges to the center of the hexagon, where a protrusion becomes visible above +1.75 V. Pd–induced modifications in the SiO_2 lattice are randomly distributed across the surface and show no preference for either line or point defects. Even for a nominal Pd coverage as high as 0.15 ML, no Pd aggregation or cluster formation is observed.

Conductance spectra of the Pd–induced features reveal an increase of the dI/dV signal at 2.3 V with respect to the bare oxide, indicating the presence of a new unoccupied state (Figure 5.2a). The spatial distribution of the conductance is plotted

in the dI/dV map shown in Figure 5.2b. High Pd–related intensity is observed at 2.3 V, which corresponds to the bias value, where the topographic contrast localizes in the center of a –Si–O– hexagon. The Pd dI/dV signal is swamped by the silica conduction band that appears as a bright line at 2.75 V.

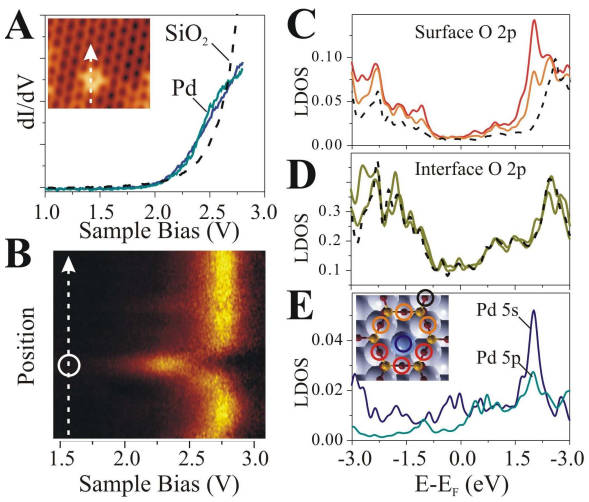

Figure 5.2: (a) Differential conductance spectra of a Pd atom and bare SiO_2/Mo(112) (set point 2.75 V). (b) dI/dV line scan of the same Pd atom along the line marked in the inset of (a). (c)–(e) Calculated LDOS for a Pd atom incorporated into a –Si–O– hexagon. (c) Contribution of the 2p orbital of the oxygen atoms in the top layer, as marked in the inset of (e). (d) Contribution of the 2p orbital in the O interface atoms. (e) Partial LDOS of the Pd 5s,p states.

DFT calculations of Pd atoms on the silica film rationalize the adsorption characteristics deduced from the experiments. Pd atoms are able to diffuse without barrier through the openings in the six–membered rings and bind to the short Mo–Mo bridge position accessible in the nanopore[10] (Figure 5.3). The resulting binding energy of 3.3 eV is almost ten times larger than on the silica surface. This strong interaction at the interface is responsible for the ineffective lateral diffusion of Pd atoms, explaining their small preference for oxide defects and the absence of Pd aggregates. Although Mo contributes most to the Pd binding, the electronic states of the oxide ring also participate in the interaction. In particular, the 2p states of the oxygen atoms in the topmost oxide plane hybridize with the Pd 5s orbital, leading to an increase of the unoccupied LDOS between 1.5–2.5 eV (Figure 5.2c). The electronic states of the Si–surface and O–interface atoms, on the other hand, remain nearly

unaffected upon insertion of the adatom (Figure 5.2d). This interplay between O and Pd orbitals is responsible for the specific contrast evolution of the –Si–O– rings accommodating a Pd atom, as demonstrated by STM simulations (Figure 5.1d, left to right). As the Pd is located deep below the oxide surface, the contrast change mainly reflects the adsorbate influence on the silica LDOS, as direct tunneling into Pd orbitals is inefficient. The LDOS contour of the occupied states shows only little change around the Pd adsorption site. However, the adsorbate–induced increase of the unoccupied LDOS leads to the appearance of the typical hexangular stars at positive bias. Structural deformations of the –Si–O– ring – involving a slight relaxation of the top layers oxygen atoms towards the embedded Pd – contribute to the electronic alterations.

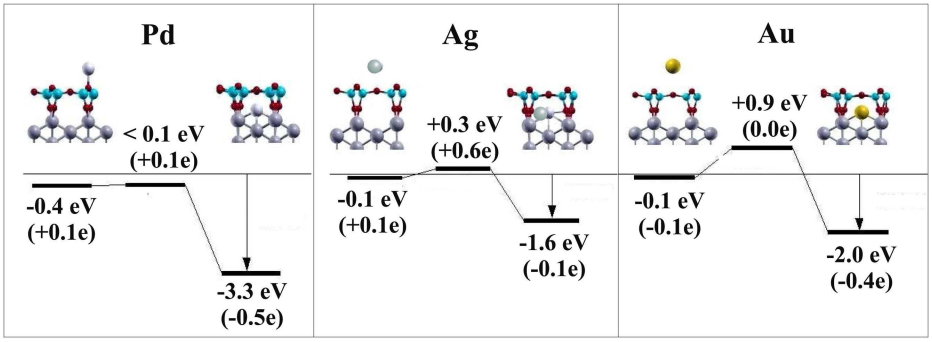

Figure 5.3: Energy profiles for the insertion of Pd, Ag and Au atoms into regular six–membered rings of the silica film. Left and right values in each plot denote the atom binding energy on top and inside the film, respectively, while the central value gives the energy barrier for penetration. All energies are given with respect to a gas–phase atom. The Bader charges during penetration are reported in parenthesis. The binding configurations of the different atoms above and below the silica film are shown in the insets.

Only at the resonance position of the Pd 5s orbital calculated at +2.0 eV (Figure 5.2e), do the Pd states directly influence the STM imaging process. The onset of tunneling into this orbital gives rise to the observed dI/dV increase in the Pd conductance spectra. The accessibility of the Pd 5s–resonance also leads to the localization of the topographic contrast within the center of the –Si–O– rings, as reproduced in the simulated STM images (Figure 5.1d, right).

5.2.2 Ag adsorption

After Ag deposition, the same hexangular stars appear on the silica surface as for Pd, although in a slightly different bias regime (Figure 5.4a). The features are visible at small negative and positive voltages, but transform into round protrusions already above 1.5 V (Figure 5.4b). The presence of hexangular stars provides a first indication that also Ag atoms are able to penetrate the holes in the –Si–O– hexagons. In contrast to the Pd species, Ag shows a certain affinity to interact with the APDB. In Figure 5.4b, one out of 18 atoms occupy a –Si–O– octagon, as marked by the square. The overall fraction of Ag atoms bound to APDB is determined to 5%, which compares to 1–2% of all available sites being located along the domain boundaries. Consequently, the probability to find an Ag in the –Si–O– octagon is 3–5 times higher than in a hexagon, suggesting a slightly lower penetration barrier at the APDB.

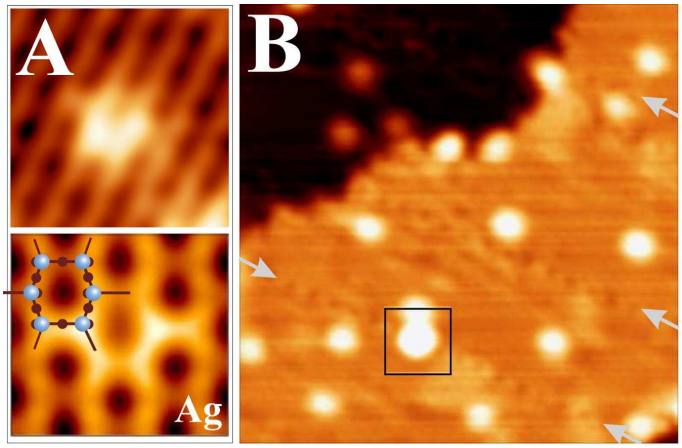

Figure 5.4: (a) Experimental (0.3 V, 5×5 nm^2) and simulated STM images (0.3 V, 1.8×1.6 nm^2) of an Ag atom on SiO_2/Mo(112) incorporated into regular six–membered rings. (b) STM topographic images of Ag on SiO_2/Mo(112) film (1.5 V, 20×20 nm^2). The nominal coverage was set to 5×10^{12} atoms per cm^2. The arrows mark domain boundaries in the film. The Ag atom denoted by the square in (b) is bound to such a boundary.

The Ag atoms experience a much higher barrier of 0.3 eV for penetrating the six–membered –Si–O– rings with respect too the Pd atoms (Figure 5.3). Assuming an Arrhenius behavior, thermal Ag atoms have a 30 times lower penetration probability than Pd atoms, which is however still high enough to yield measurable pen-

etration rates.[†] The Ag atoms are able to overcome this barrier only at the moment of impact. After thermalization, the atoms are trapped in a weak physisorption potential of roughly 0.1 eV and diffuse to adjacent APDB, where penetration of the octagonal rings remains possible. This diffusive transport might be responsible for the higher adsorption probability of Ag atoms at APDB with respect to regular oxide sites. After passing the nano–hole, Ag binds to the Mo–SiO_2 interface with 1.6 eV, remaining in its neutral $4d^{10}5s^1$ configuration as above the surface (Figure 5.3). The binding energy is substantially lower than for Pd due to the chemically inactive nature of the low–lying Ag $4d$ states. Similar to the Pd case, the largest change in the oxide electronic structure is the formation of an O $2p$–Ag $5s$ hybrid state that peaks at $+1.6$ eV and exhibits a long tail crossing the Fermi level (Figure 5.5a). Tunneling into this tail produces the typical star–like images of inserted Ag atoms, reflecting from the enhanced LDOS of the six O atoms of the hosting ring (Figure 5.4a). Above 1.5 V, the O $2p$–Ag $5s$ hybrid state becomes directly available for electron transport and the imaging contrast localizes at the Ag atoms (Figure 5.4b). Also the resonance state of inserted Ag shows up experimentally as a dI/dV peak at 2.05 V, supporting the proposed binding mechanism (Figure 5.5b).

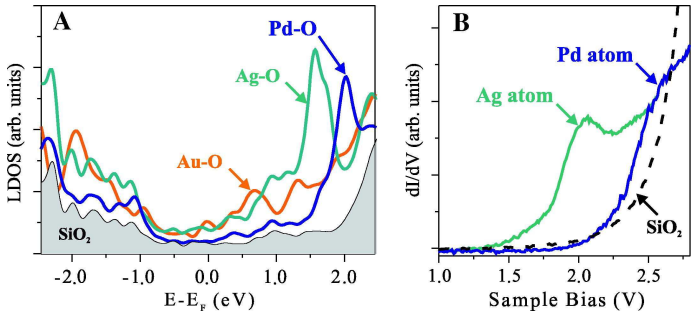

Figure 5.5: (a) Total LDOS of the pristine silica film (gray) and plots of the hybrid states formed between s–orbitals of incorporated Pd, Ag and Au atoms and the O $2p$ states of the surface oxygen atoms. (b) Experimental dI/dV spectra of the pristine oxide film and inserted Pd and Ag atoms, showing similar resonance states as in (a). (The Pd data are again reported in the graph in order to compare the three species, Pd, Ag and Au)

[†]Quantitative values for the penetration rate cannot be given as the pre–factor for the Arrhenius process is unknown.

5.2.3 Au adsorption

Exposure of the oxide surface to Au atoms results in a completely different picture (Figure 5.6a). While no topographic changes are detected on defect–free oxide terraces, protrusions of different sizes become visible along the APDB. The smallest feature identified with the STM sits in an eight–membered –Si–O– ring and is tentatively assigned to a single Au adatom (Figure 5.6c, circled, left to right). It shows a similar bias–dependent contrast as the Pd species. At small negative bias, two bright spots appear at the long side of the octagon, leaving the nanopore in the center as a dark hole. With increasing positive bias, the topographic contrast first spreads over larger sections of the ring and then moves towards the ring center, where it forms an elliptical protrusion (Figure 5.6c, circle, right). The second smallest aggregate is characterized by an asymmetric shape with respect to the Mo$[\bar{1}10]$ direction, which indicates occupation of two non–equivalent adsorption sites in the –Si–O– octagon (Figure 5.6c, square). At higher exposure, larger Au aggregates with spherical shapes and negligible bias–dependent contrast develop along the APDB (bottom right of Figure 5.6a). The Au–related features induce little change in the dI/dV spectra of the SiO_2 film. The monomer spectrum exhibits a slight increase in the conductance at $+1.5$ V, similar to the one observed at $+2.3$ V for Pd. With increasing aggregate size, the dI/dV spectra of the Au species become indistinguishable from the silica background, demonstrating their strong coupling to the support.

Also in the Au case, the experimental findings are reproduced well by DFT. The larger Au atoms have to overcome a barrier of 0.9 eV to penetrate a typical six–membered ring[10] (Figure 5.3). As this activation energy is higher than the Au binding energy to the SiO_2 of 0.1 eV, the adatoms remain weakly bound to the surface and rapidly diffuse even at low temperature. Only at APDB, exposing eight–membered rings with larger diameter and lower activation energy for penetration (0.15 eV), binding to the Mo–SiO_2 interface becomes possible with 2.67 eV. The insertion of an Au atom again induces strong modifications in the silica LDOS. In contrast to Pd, these changes are not primarily induced by a direct hybridization with the Au orbitals (Figure 5.5), but result from a long–range deformation of the oxide lattice. Not only the atoms of the affected octagon relax outward to allocate more space for the Au, the adjacent four–membered rings take part in the relaxation process as well. The structural rearrangement has little effect on the filled states of both oxygen and silicon atoms, but increases the unoccupied LDOS of the oxygen atoms in the oxide top layer. This specific LDOS change reflects the widening of the octagon,

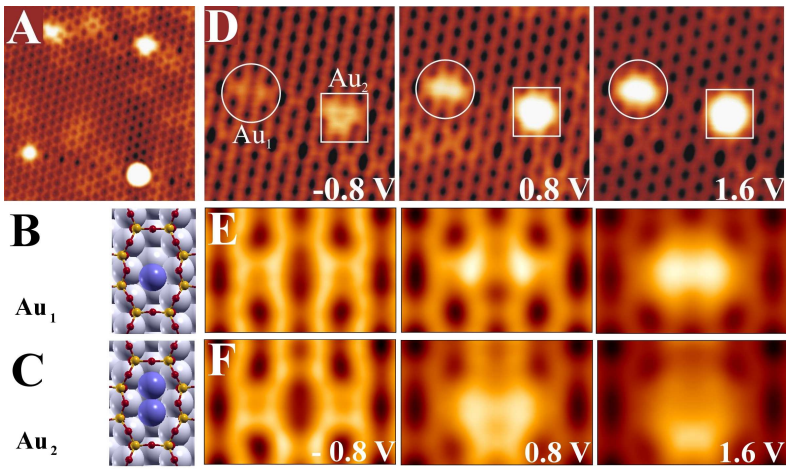

Figure 5.6: (a) STM image (0.5 V, 13×13 nm^2) of 0.1 ML Au on SiO_2 on Mo(112). (b) Structure model for Au monomer and (c) for Au dimer. Bias dependence of the topographic contrast for Au aggregates in (d) experimental (4.5×4.5 nm^2) and (e–f) simulated STM images (2.1×1.4 nm^2, 5×4 supercell).

which reduces the spatial overlap and therefore the hybridization between silicon and oxygen orbitals. The four oxygen atoms in the –Si–O– ring that are next to the embedded Au are affected most strongly by the lattice distortion and consequently show up as bright spots in experimental and simulated STM images taken at small positive bias (Figures 5.6d and e). At voltages above +1.5 V, direct tunneling into Au states becomes important, as revealed by the shift of the topographic contrast towards the ring center and the increase of the dI/dV signal of the Au species. The new channel for tunneling is related to the empty part of the Au 6s orbital, which has split into an occupied and an unoccupied resonance at $-0.8/+0.8$ eV due to the interaction with the Mo states.

The nanopores at APDB are large enough to accommodate a second and third Au atom. The Au dimer adopts a flat configuration with both atoms sitting in a Mo–Mo bridge site (Figure 5.6c). The energy gain for attaching the second atom to a pre–adsorbed monomer amounts to 2.48 eV. A third atom binds with 1.77 eV to the bridge position of the Au_2, thus forming a triangular trimer. Based on STM simulations, Au dimers are clearly identified in the experiment (Figures 5.6d, square and f, central panel). In images taken at small positive or negative bias, only the

upper and central parts of the affected –Si–O– octagon become visible, as these sections are subject to the largest structural deformation. At higher positive bias, the energy levels of Au_2 dominate the tunneling process. Due to hybridization of the two $6s$ orbitals of the dimer atoms, the lowest accessible state shifts towards E_F with respect to the monomer and the ring center appears with bright contrast already below $+0.8$ V (Figure 5.6c, square). The energy gain when adding atoms to an embedded Au_1 species indicates that APDB are preferential nucleation sites on the SiO_2 film, and the growth of large Au particles decorating the line defects is indeed observed at higher coverage.[9]

5.2.4 Penetration mechanism

The origin for the dramatically different penetration barriers for Pd, Ag and Au atoms shall be discussed in the last part of the chapter. In a first intuitive picture, the barrier height might be connected to the size of the respective gas–phase atoms, as given by their van der Waals radius.[10] Following this model, smaller atoms should exhibit a reduced barrier with respect to larger ones, a trend that is indeed observed for Pd (van der Waals radius of 163 pm) versus Ag (172 pm). However, the penetration barrier for Au is substantially higher, although its van der Waals radius of 165 pm is relatively small due to the relativistic contraction of Au orbitals. The atomic radius seems therefore to be an inappropriate parameter to rationalize the observed trend in barrier height. In a more sophisticated model, the penetration barrier might be linked to the repulsion that is exerted by the oxide charge density, especially the occupied O $2p$ states, on the incoming atom. This interaction will be dominated by the spatially most expanded adatom orbitals, that are the s–like valence states. Due to its unfilled nature, the Pd $5s$ orbital produces only a small repulsion and the resulting penetration barrier is low. In contrast, the half–filled Ag $5s$ and Au $6s$ orbitals will strongly interact with the surface O $2p$ states during penetration. The surprising fact that Ag has a three times lower energy barrier than Au is explained by a transient positive charging of Ag atoms when passing the ring plane. The Ag atom transfers charge density from its $5s$ orbital into the Mo states, thereby reducing the electron–electron interaction with the oxide states. This effect is clearly revealed from the computed Bader charge of $+0.6\ e$ for an Ag atom in the ring plane (Figure 5.3).

A similar mechanism is not accessible for gold. An Au atom is a strongly electronegative species and rather accumulates excess electrons in its $6s$ orbital instead of

transferring charge density to adjacent atoms.[11,12] Consequently, the Au remains neutral when passing the hole in the silica top–layer (Figure 5.3). Also an internal charge redistribution, e.g. by promoting the $6s$ electron into the "leaner" $6p_z$ state having its electron density localized along the penetration axis, is inhibited by the high activation energy of 4.6 eV.[13] The Au atoms are therefore unable to lower the repulsive interaction with the oxide surface electrons and the penetration barrier remains high.

5.3 Summary

The nano–porous SiO_2 film grown on Mo(112) exhibits essential properties of an atomic sieve. Single metal adatoms can either penetrate the openings in the top–most silica layer, followed by a strong binding at the metal–oxide interface, or are repelled at the inert oxide surface. As demonstrated by the combined STM/DFT study, the oxide penetration barrier varies considerably for different atomic species. Whereas Pd atoms experience virtually no barrier, the activation energy for penetration steeply increases when going to Ag and Au atoms. The actual barrier height is connected to a repulsive interaction between the valence electrons of the incoming atom and the electron density at the oxide surface, and therefore a purely electronic effect. The identification of this interaction mechanism enables a reliable prediction of penetration barriers for other atomic and molecular species, being a first step towards the construction of a true atomic sieve based on the SiO_2/Mo system.

Bibliography

[1] S. Bhatia, *Zeolite Catalysis: Principles and Applications* (1990) CRC Press, Boca Raton.

[2] A. K. Cheetham, G. Ferey, T. Loiseau, *Angew. Chem.* **111** (1999), p. 3466.

[3] A. K. Cheetham, G. Ferey, T. Loiseau, *Angew. Chem. Int. Ed.* **38** (1999), p. 3268.

[4] L. Giordano, A. Del Vitto, G. Pacchioni, *J. Chem. Phys.* **124** (2006), p. 034701.

[5] J. Tersoff, D. R. Hamann, *Phys. Rev. Lett.* **50** (1983), p. 1998.

[6] N. Nilius, T. M. Wallis, W. Ho, *Phys. Rev. Lett.* **90** (2003), p. 046808.

[7] N. Nilius, E. D. L. Rienks, H.–P. Rust, H.–J. Freund, *Phys. Rev. Lett.* **95** (2005), p. 066101.

[8] M. Sterrer, T. Risse, U. Martinez Pozzoni, L. Giordano, M. Heyde, H.–P. Rust, G. Pacchioni, H.–J. Freund, *Phys. Rev. Lett.* **98** (2007), p. 096107.

[9] K. Min, W. T. Wallace, A. K. Santra, D. W. Goodman, *J. Chem. Phys. B* **108** (2004), p. 16339.

[10] In: D.R. Lide, Editor, *Handbook of Chemistry and Physics* (2008) CRC Press, Boca Raton.

[11] G. Pacchioni, L. Giordano and M. Baistrocchi, *Phys. Rev. Lett.* **94** (2005), p. 226104.

[12] N. Nilius, V. Ganduglia–Pirovano, V. Bradzova, M. Kulawik, J. Sauer and H.–J. Freund, *Phys. Rev. Lett.* **100** (2008), p. 096802.

[13] In: C.E. Moore, Editor, *Atomic Energy Levels* (1952) US–Gov. Print Office, Washington.

CHAPTER 6

Adsorption of Pd and Au atoms on SiO_2 films: the role of atomic structure[†]

In the previous Chapter we reported the possibility to use well–defined, crystalline SiO_2/Mo(112) films as 2D atomic sieve. The experimetal procedure for the preparation of this silica films has been described in details in Section 1.3.3. In addition, the SiO_2/Mo(112) surface prepared under oxygen–rich conditions results in a new phase where a layer of oxygen atoms is adsorbed only on the Mo surface, i.e., below the silica layer.[1] Thus, two kinds of silica films can be prepared on the Mo(112) substrate: one with additional O atoms at the interface, referred to as "O–rich" to discriminate it from the "O–poor" film without these atoms. The two phases exhibit slightly different values of the phonon frequency, which are basically related to the Si–O stretching mode.

In the last Chapter we have considered the adsorption of Pd, Ag and Au on the O–poor SiO_2/Mo(112) films. It has been found that Pd and Ag can penetrate the silica nanopores and bind at the silica/metal interface. Au atoms instead interact very weakly with the silica surface and can easily diffuse and aggregate only along

[†]The results described in this Chapter have been reported in: M. Baron, D. Stacchiola, S. Ulrich, N. Nilius, S. Shaikhutdinov, H.-J. Freund, *U. Martinez*, L. Giordano and G. Pacchioni, *J. Phys. Chem. C* **112** 3405 (2008)

the domain boundaries defects running along the $[\bar{1}10]$ direction. In order to further verify the hypothesis, here we report on the comparative study of the Pd and Au atom deposition on the O–poor and O–rich monolayer films as well as on a multilayer silica film, used as a reference support. Concomitantly, the density functional theory (DFT) calculations are extended to the O–rich films and also to the adsorption of CO on both films. The experimental results provide compelling evidence for the structural models proposed by DFT. This represents an interesting example for the close interplay between structural and adsorption properties, where a small change in the structure of the oxide–metal interface may result in quite substantial differences in adsorption phenomena.

6.1 Computational and Experimental Details

Computational Details

The calculations has been performed with the VASP code (see Sec. 2.1.1, pag. 25). The kinetic energy cutoff has been set to 400 eV. A vacuum of at least 10 Å separates the slabs and a dipole correction has been applied. The Mo(112) substrate has been modeled by seven Mo layers which well reproduce the band structure of bulk Mo.[2] The O atom linking the SiO_4 tetrahedra to the Mo surface is in a bridge position over two protruding Mo atoms.[3] During geometry optimization, the three Mo bottom layers were frozen at bulk positions while the top four layers were optimized. The atoms within the slab are relaxed until the atomic forces are less than 0.01 eV/Å.

The surface stoichiometry of the slab that gives a Mo(112)–c(2×2) structure is $Mo_{14}Si_2O_5$, as observed by low–energy electron diffraction. For modeling the adsorption of Au or Pd atoms, the cell size has been increased to (4×2) in order to represent a low concentration of adsorbed species. The calculations have been done in a 2×2×1 grid of k–points. The surface slabs are separated by a vacuum gap of 10 Å.

Experimental Details

The experiments were performed in an ultrahigh vacuum (UHV) chamber (base pressure below 1×10^{10} mbar) equipped with X–ray photoelectron spectroscopy, an infrared reflection absorption spectroscopy (IRAS), and standard facilities for sample preparation. The IRAS spectra were measured with p–polarized light at 84°

grazing angle of incidence (resolution ∼4 cm^{-1}).

Multilayer silica films were grown by deposition of >3 ML of Si in UHV onto clean Mo(112) at 300 K followed by oxidation at 400 K in 5×10^{-7} mbar of O_2. The sample was then slowly heated to 900 K in 5×10^{-7} mbar of O_2 and finally annealed at 1150 K in UHV.[4]

Pd and Au (both 99.99%, Goodfellow) were vapor deposited at 90 K (and 10 K for the STM measurements) using a commercial evaporator (Focus EFM 3) with a deposition rate of ca. 0.2 Å/min. For each Pd/silica sample, a new silica film was prepared. The Pd coverage is presented in the text as the nominal thickness (in Å); approximately 2.3 Å corresponds to a monolayer coverage.

6.2 Results and Discussion

Figure 6.1 shows the IRA spectrum of an O–poor silica film with the main feature at 1063 cm^{-1} assigned to the Si–O–Mo asymmetric stretching vibrations.[3,5,6] It has been previously shown that for the O–rich films this mode shifts to the lower frequencies by 10 cm^{-1}.[1] All these features, i.e., at 1063 cm^{-1} for O–poor and at 1049 cm^{-1} for O–rich phases as well as the weak bands at 775 and 675 cm^{-1}, were reproduced by DFT calculations.[1]

Infrared spectroscopy serves to study the impact of the admetals on the oxide phonons.[7] The deposition of 0.1 Åof Pd causes a 14 cm^{-1} red–shift of the Si–O–Mo stretching band and signal broadening as shown in Figure 6.1. For comparison, incorporation of Al into the film to produce aluminosilicate films results in a 30 cm^{-1} red–shift.[8] The red–shift is Pd–coverage–dependent, as observed for alumina films, and various mechanisms have been proposed to explain this behavior.[7] The adsorption of Pd on the O–rich films showed a similar effect. In contrast, the deposition of the same amount of Au only decreases the intensity but does not induce any peak shift on both O–poor and O–rich films.

To study the effect of the film thickness on the interaction with metal atoms, we also deposited Pd onto the atomically flat, amorphous SiO_2 films of approximately three monolayers in thickness (henceforth referred to as "multilayer" film).[4] Even for subnanometer thickness, these films show phonon vibrations at 1258 cm^{-1} characteristic of the bulk SiO_2 systems.[9] Figure 6.1 shows that the silica phonon in the multilayer film is not affected by the adsorption of even larger amounts of Pd. The observation of the spectral shift for the Pd and not for the Au deposition is a first

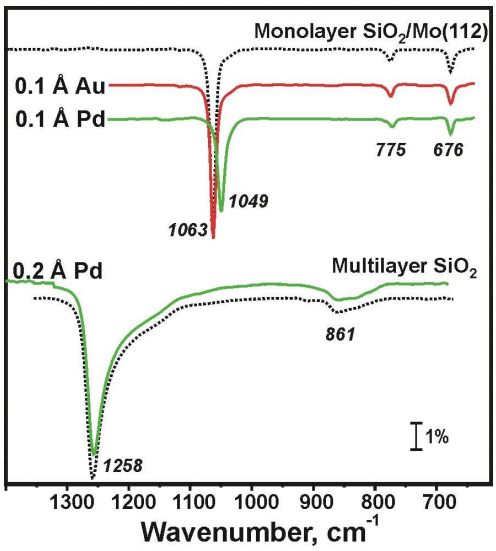

Figure 6.1: Phonon region of the IRA spectra obtained on an O–poor monolayer SiO_2/Mo(112) film and on a multilayer silica film, exposed to small amounts of Au and Pd as indicated (see the text). The spectra for the clean silica surfaces are shown for comparison (dotted lines). The spectra are offset for clarity.

indication of the different interaction of these two metals with the monolayer silica films. Furthermore, the fact that Pd adsorption on a thicker silica film does not modify the phonon spectrum implies a specific adsorption behavior of Pd on the monolayer films.

Figure 6.2 shows the interaction energy profile obtained from DFT calculations for a Pd atom bound to monolayer SiO_2/Mo(112) films. On the O–rich phase, the Pd atom sits above the center of the ring and is bound by 0.44 eV. A small energy barrier (0.08 eV) separates this local minimum from a deeper minimum where the Pd atom is adsorbed below the silica layer with a binding energy of 0.68 eV. The effect of penetration of the Pd atom below the silica layer is much more dramatic on the O–poor phase: the estimated barrier for diffusion is negligible, and the binding at the interface is very large, ca. 3.3 eV.[10] In this case, the Pd atom interacts directly with the Mo metal surface, while on the O–rich phase this is hampered by the presence of the adsorbed O atom (see Figure 6.2). In both cases, however, the presence of the Pd atom at the interface slightly perturbs the structure of the silica film and affects the phonon spectrum. In particular, the calculations show that the main phonon

frequency is red-shifted by 11 cm^{-1} for the O–poor (from 1058 to 1047 cm^{-1}) and by 23 cm^{-1} for the O–rich structures (from 1043 to 1020 cm^{-1}), respectively, which is consistent with the experimental findings.

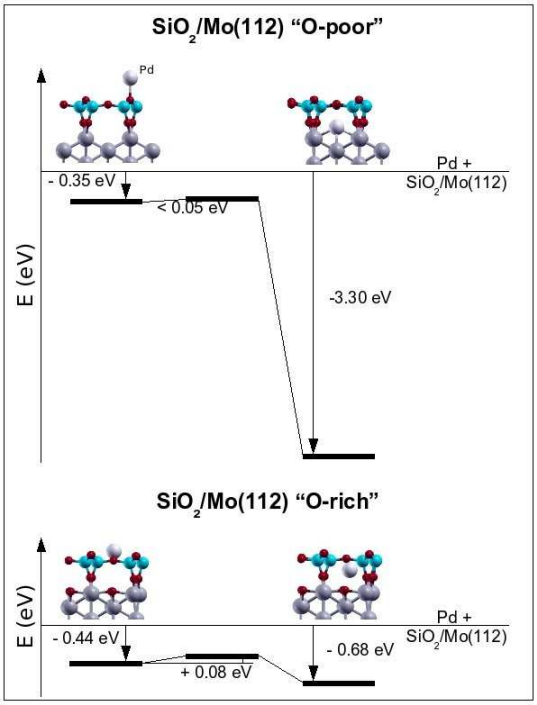

Figure 6.2: Energy profile of the interaction of a single Pd atom with an O-poor (top) and O-rich (bottom) SiO_2/Mo(112) film. The central panel indicates the energy of the transition state. The side view of the silica film and the position of the Pd adatom in the structure are shown. Color key: large gray spheres, Mo; white spheres, Pd; small blue spheres, Si; red spheres, O.

The adsorption of Au is predicted to be completely different. According to the calculations, Au atoms do not migrate into the rings because of very weak interaction with the O–poor film and the large atomic size, giving rise to a higher barrier than that for Pd. On the O–rich phase, subsurface Au is even unbound. Given the low binding energy of Au with the silica surface of about 0.1 eV, a very low diffusion barrier is expected, so that surface diffusion and subsequent aggregation of Au adatoms likely occurs at low temperatures.

One can expect that the different interaction of Pd with the silica films will manifest itself in the adsorption of CO as a probe molecule, since CO adsorption on the Pd surfaces is well understood and a large database exists for IR spectra.[11]

Two bands in the CO stretching region were observed at 90 K at saturation CO coverage. One is around 2105 cm^{-1} assigned to terminal CO, and another broad feature is centered at 1950 cm^{-1}, which is assigned to multicoordinated CO molecules (e.g., see inset in Figure 6.3).

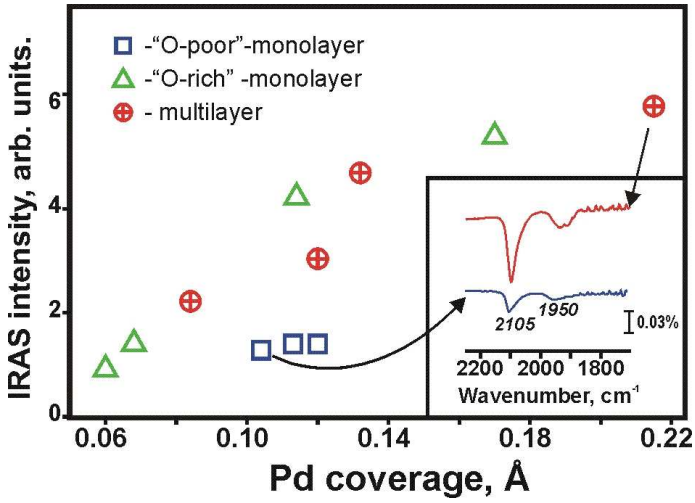

Figure 6.3: Integral area of CO IRAS signal (2200–1800 cm^{-1}) as a function of Pd coverage measured on different silica films, as indicated. The inset shows the IR spectra observed for the samples, marked by the arrows, after exposure to 20 L of CO at 90 K.

Figure 6.3 plots the integral peak area as a function of the amount of Pd deposited. (Note that the same trend is found separately for either terminal or multicoordinated CO bands.) Although the intensity of the IR lines of adsorbed CO is not linearly proportional to the site population, it provides a qualitative measure of the total CO uptake and hence the Pd surface area. Data show that Pd atoms on the O–rich monolayer and the multilayer films behave similarly, while Pd atoms on the O–poor films exhibit much lower CO adsorption capacity than those on the O–rich films. In principle, there may have two reasons for this. It can be due to different Pd dispersions (particle size and density) that result in different metal surface areas on these two silica surfaces. Alternatively, some portion of Pd is not accessible to CO as a result of migration into the film.

To better understand the microscopic aspects of the observed behavior, we have performed DFT calculations on the CO adsorption. On the O–poor phase, where Pd is strongly bound to the substrate, CO is unbound to Pd (by 0.11 eV). Even if we assume that a Pd–CO complex is formed under elevated CO pressures, the barrier to pull the Pd–CO species out from the hexagonal ring would be very large, approximately 1.7 eV (see Figure 6.4). This means that on the O-poor surface, CO is unable to bind to the Pd atoms, which are trapped at the interface. The situation changes on the O–rich film. Here CO binds strongly (by 1.04 eV) to Pd atoms located in the "cavity". The formation of a strong Pd–CO bond weakens the interaction of Pd with the substrate so that the Pd-CO complex becomes unbound by 0.69 eV and can easily escape from the cavities by overcoming a barrier of 0.23 eV only. On the surface, the Pd–CO complex is bound to the silica layer by 0.66 eV and can diffuse and eventually aggregate with other Pd atoms or clusters. Thus, CO adsorption has a completely different effect on Pd atoms deposited on O–poor or O–rich silica monolayers. This may explain recent observation of CO–induced sintering effect on the low–temperature Pd deposition.[12]

6.3 Summary

The combined experimental and theoretical study of the interaction of Pd and Au atoms with monolayer and multilayer silica films demonstrates the importance of structural details in determining of the adsorption properties of oxide surfaces. In particular, Au behaves in a similar way on all three silica supports considered, namely, O–rich and O–poor monolayer films and three–monolayers amorphous films. Gold aggregates at the surface preferentially on the line defects. In contrast, the Pd interaction with the oxide film and its tendency to bind CO are substrate–dependent. On the monolayer films, this manifests itself in a change of the phonon frequency and the bright appearance of the six–membered silica rings in the STM images due to the presence of subsurface Pd atoms, confirming previous theoretical predictions that Pd can migrate into the six–membered rings.[10] It was also found that the CO uptake for Pd deposited on O–poor films is much smaller than that on the O–rich phase and multilayer silica.

DFT calculations showed that on the O–poor films the Pd atoms strongly bind at the silica–Mo interface and do not interact with CO, so that the total amount of adsorbed CO molecules remains small. On the O–rich monolayer film, the Pd atoms

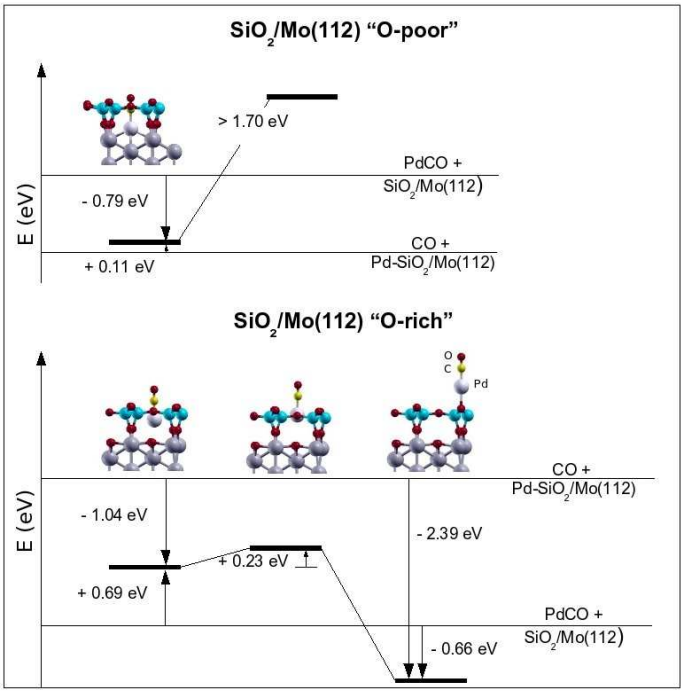

Figure 6.4: Energy profile of the interaction of CO with a Pd atom adsorbed on O–poor (top) and O–rich (bottom) phases of SiO_2/Mo(112). The central panel indicates the transition state between initial and final configurations. The insets show the structure of the silica film (side view) and the position of the PdCO complex in the subsurface state (left) and above the surface (right). Color key: large gray spheres, Mo; white spheres, Pd; small blue spheres, Si; red spheres, O.

are also adsorbed subsurface, but the CO is able to form stable PdCO complexes which can escape from the cavity and aggregate to form Pd nanoparticles. In contrast, Au does not show any of these effects because the size of the rings is too small for penetration to occur. The adatoms bind only weakly on the surface and can easily diffuse and aggregate on the silica surfaces. The continuous silica monolayer can therefore be viewed as the first example of a two–dimensional sieve, which could be used to selectively permit diffusion of metal atoms or small molecules to a metal substrate.

Bibliography

[1] M. Sierka, T. K. Todorova, S. Kaya, D. Stacchiola, J. Weissenrieder, J. Lu, H. Gao, S. Shaikhutdinov, H.–J. Freund, J. Sauer, *Chem. Phys. Lett.* **111** (2006), p. 424.

[2] D. Ricci, G. Pacchioni, *Phys. Rev. B* **69** (2004), p. 161307.

[3] J. Weissenrieder, S. Kaya, J. L. Lu, H. J. Gao, S. Shaikhutdinov, H.–J. Freund, M. Sierka, T. Todorova, J. Sauer, *Phys. Rev. Lett.* **95** (2005), p. 076103.

[4] D. Stacchiola, M. Baron, S. Kaya, J. Weissenrieder, S. Shaikhutdinov, H.–J. Freund, *Appl. Phys. Lett.* **92** (2008), p. 011911.

[5] M. S. Chen, A. K. Santra, D. W. Goodman, *Phys. Rev. B* **69** (2004), p. 155404.

[6] S. Wendt, E. Ozensoy, T. Wei, M. Frerichs, Y. Cai, M. S. Chen, D. W. Goodman, *Phys. Rev. B* **72** (2005), p. 115409.

[7] M. Frank, K. Wolter, N. Magg, M. Heemeier, R. Kuhnemuth, M. Bäumer, H.–J. Freund, *Surf. Sci.* **492** (2002), p. 270.

[8] D. Stacchiola, S. Kaya, J. Weissenrieder, H. Kuhlenbeck, S. Shaikhutdinov, H.–J. Freund, M. Sierka, T. K. Todorova, J. Sauer, *Angew. Chem.* **45** (2006), p. 7636.

[9] C. T. Kirk, *Phys. Rev. B* **38** (1988), p. 1255.

[10] L. Giordano, A. Del Vitto, G. Pacchioni, *J. Chem. Phys.* **124** (2006), p. 034701.

[11] P. Hollins, *Surf. Sci.* **16** (1992), p. 51.

[12] J. L. Lu, S. Kaya, J. Weissenrieder, H.–J. Gao, S. Shaikhutdinov, H.–J. Freund, *Surf. Sci.* **600** (2006), p. L153.

CHAPTER 7

Modifying the adsorption characteristic of inert silica films by inserting anchoring sites[†]

Tailoring the adsorption properties of solid materials has been a long–term objective in surface science.[1–3] The functionalization of surfaces is determined by several aspects. First, the density and spatial arrangement of binding sites need to be controlled. Second, the adsorption behavior should be chemically selective, admitting only certain species to interact with the surface. And last, the internal structure of the ad–material should be tunable. Systems with designable adsorption properties have a wide range of applications, e.g., as catalysts in stereoselective reactions, chemical sensors, and template surfaces for selforganization processes.

Several approaches have been developed to fabricate tunable adsorption systems; however, most of them are unable to fulfill all the specifications mentioned above. Regular arrays of binding sites are produced on vicinal surfaces,[4] molecular template structures,[5] and epitaxial systems exhibiting an ordered network of dislocations.[6,7] Chemical sensitivity is achieved by equipping the surface with suitable functional groups to stimulate binding to the desired adsorbates. Alternatively, the size–selective adsorption behavior of porous materials, e.g., zeolites, is exploited to

[†]The results described in this Chapter have been reported in: S. Ulrich, N. Nilius, H-J Freund, *U. Martinez*, L. Giordano and G. Pacchioni, *Physical Review Letter* **102** 016102 (2009)

tune surface reactions via the adsorbate diameter.[1,8] Controlling the internal structure of the ad–material remains the most difficult part. Here, mainly atomic manipulation with the scanning tunneling microscope (STM) has been employed to assemble aggregates with a defined structure and chemical composition.[9,10]

In this chapter, we report a new approach towards a functionalized adsorption system that is based on the insertion of defined binding sites into an initially inert surface. A suitable system to realize this concept is a porous silica film prepared on Mo(112) (see Section 1.3.3). The film is chemically inactive and only physisorbs inorganic molecules, like CO and H_2O.[11] However, as described in the previous two chapter, small metal atoms can be inserted into the oxide nanopores, as demonstrated for Pd and Ag, whereas larger atoms such as Au are unable to penetrate the holes in the silica top layer (see Chapters 6 and 5). The inserted atoms remain close to the surface and might be used to stabilize adsorbates on the inert oxide film.

The approach is similar to the doping of oxide materials with impurity atoms or point defects, as an alternative route to creating surface binding sites. Substantial changes in the adsorption behavior were indeed reported for Li– or Ti– doped SiO_2, and MgO surfaces containing oxygen vacancies.[12–15] However, while doping affects the global electronic and chemical properties of the oxide material, the insertion of single–atom anchors modifies the binding characteristics only locally. The possibility of using Pd atoms incorporated into a silica film to anchor metal adatoms is now demonstrated with a STM and density functional theory (DFT), approving this new route towards a functionalized adsorption system.

7.1 Computational and Experiemtal Details

Computational Details

The calculations has been performed with the VASP code (see Sec. 2.1.1, pag. 25). The kinetic energy cutoff has been set to 400 eV. A vacuum of at least 10 Å separates the slabs and a dipole correction has been applied. The Mo(112) substrate is described by seven Mo layers, whereby the three bottom layers are kept frozen at bulk positions during geometry optimization. The silica film is modeled with (4×2) and (6×4) supercells, corresponding to a stoichiometry of $Mo_{14}Si_2O_5$ and $Mo_{24}Si_6O_{15}$, respectively.

Experimental Details

The experiments are performed in a custom built UHV–STM operated at 10 K. The silica film is prepared on an oxygen precovered Mo(112) surface by depositing 1.2 monolayers silicon at 800 K in an O_2 ambience of 1×10^{-7} mbar. Sample annealing to 1200 K leads to the formation of a crystalline SiO_2 layer, as indicated by the sharp $c(2\times2)$ LEED pattern.

Single Pd, Ag, and Au atoms are deposited onto the film from high–purity metal wires (99.95%) wrapped with a tungsten filament. Although deposition is performed at 20 K, the atoms have sufficient initial energy to perform transient diffusion into their equilibrium configuration. The local density of states (LDOS) of the sample is probed by differential conductance (dI/dV) spectroscopy performed with lock–in technique and open feedback loop (10 mV/1137 Hz modulation).

7.2 Results and Discussion

STM topographic images of the bare film show the characteristic honeycomb structure of the silica. Upon Pd exposure, distinct hexagonal stars appear in images taken at 0.5 V (Figure 7.1a). They transform into bright protrusions of 0.7 Å height above 2.0 V sample bias. As described in details in the Chapter 5, the features are assigned to Pd atoms that have penetrated the silica nanopores and bind to the Mo–SiO_2 interface with 3.3 eV (referred to as Pd_{sub}). The characteristic starlike contrast originates from a hybridization between the Pd $5s$ and O $2p$ orbitals, which renders the oxygen atoms of the hosting –Si–O– ring visible in the STM. Above $+2.0$ V sample bias, the Pd $5s$ becomes directly accessible for tunneling electrons, and the contrast localizes at the Pd_{sub} atom in the center of the pore (Chapter 5 pag. 77).

To investigate the possibility of anchoring single atoms to these Pd_{sub} species, three sets of experiments are performed: (i) deposition of 1×10^{13} Pd atoms per cm^2 onto a silica film already containing 2×10^{13} cm^{-2} Pd_{sub} and deposition of (ii) 1×10^{12} cm^{-2} Au and (iii) 1×10^{12} cm^{-2} Ag atoms onto a silica film with 1×10^{13} cm^{-2} Pd_{sub} incorporated (Figures 7.1b–7.1d). In all three cases, new species appear on the oxide surface, which clearly differ in height, shape, and bias-dependent contrast from the Pd_{sub} anchors. The species are imaged as round protrusions at all sample biases, in contrast to the hexagonal shape of inserted Pd_{sub}, and reach apparent heights of more than 2.0 Å (compared to 0.7 Å for Pd_{sub}). They are not compatible with single Ag or Au atoms on the silica surface, either. According to DFT calcula-

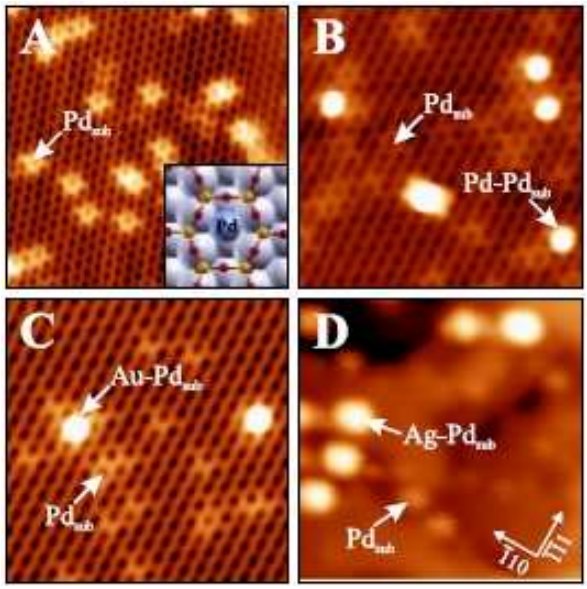

Figure 7.1: (a) STM topographic image of SiO_2/Mo(112) after insertion of Pd_{sub} species (U_s=1.2 V, 14×14 nm^2). (b) Same surface after deposition of single Pd (0.5 V), (c) Au (0.5 V), and (d) Ag atoms (1.9 V, 14×14 nm^2). While only Pd_{sub} species are observed in (a), new ad–structures become visible in (b–d). The inset in (a) shows a structure model of a Pd_{sub} in a silica pore (Si, small yellow; O, small red; and Mo, large blue circles).

tions, both atomic species only weakly interact with the oxide film (adsorption energies below 0.05 eV) and perform rapid diffusion even at low temperature (Chapter 5 pag. 77). Whereas the Ag atom is able to pass the opening in the –Si–O– hexagons, producing similar STM features as the Pd_{sub}, the Au atom is too big for penetration and binds exclusively at domain boundaries exposing larger pores. As the new species are neither located along such boundaries nor exhibit the unusual contrast of an embedded atom, they can safely be discriminated from Ag and Au atoms. The adsorption structures emerging after Pd, Ag, and Au deposition are therefore assigned to single atoms bound to Pd_{sub} anchors in the silica film, a hypothesis that will be supported by further experimental evidence in the following.

The ad–species are easily removed from the oxide surface by applying moderate voltage pulses to the STM tip (3–5 V), as shown for a Pd–Pd_{sub} complex in Figure 7.2. After the manipulation experiment, the characteristic signature of an

embedded Pd_{sub} becomes visible in every case, suggesting that the Pd_{sub} anchor is indeed required to stabilize the adatom. Furthermore, the different ad–species exhibit dI/dV fingerprints that clearly deviate from the spectroscopic response of the inserted atoms. For example, while a Pd_{sub} shows a weak dI/dV shoulder at $+2.3$ V, attributed to the Pd $5s$ orbital, a pronounced maximum at $+1.75$ V is observed for the Pd–Pd_{sub} complex (Figure 7.3a). Similarly, the Au–Pd_{sub} species exhibits enhanced dI/dV intensity at -0.2 V and -1.6 V, whereas no maxima are revealed for Au monomers located at the domain boundaries. Only for Ag–Pd_{sub} complexes, no dI/dV spectra could be acquired, because the Ag atom easily desorbs during a spectroscopic run.

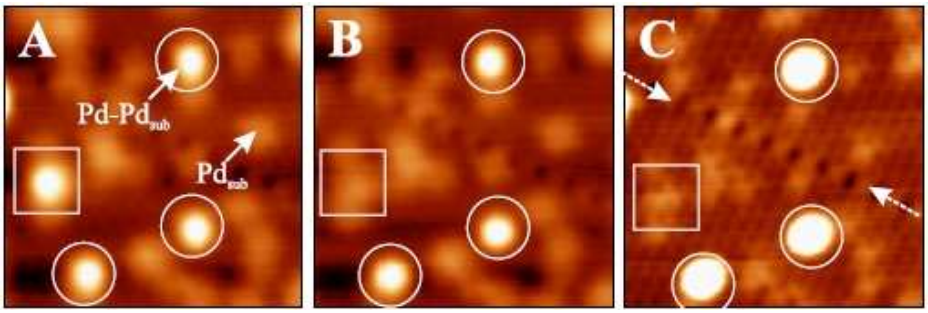

Figure 7.2: (a) STM topographic image of Pd_{sub} and Pd–Pd_{sub} species on SiO_2/Mo(112) (U_s=1.0 V, 10×10 nm^2). (b) As in (a) but after controlled removal of the adatom marked by the square box. (c) As in (b) but with enhanced contrast to show the silica atomic structure. Below the removed atom, the signature of a Pd_{sub} becomes visible that has initially anchored the ad–species. The circles indicate other Pd–Pd_{sub} complexes as guides for the eye; the dashed arrows mark a silica domain boundary.

The attachment of Pd, Ag, and Au atoms to Pd_{sub} anchors in the silica film is verified by DFT calculations. In all three examples, the adatoms form covalent bonds with a Pd_{sub} sitting in an oxide pore, however, with rather different binding energies. The strongest interaction is found for Pd adatoms, which bind with 1.16 eV to the Pd_{sub} (bond length: 2.66 Å). Without a surface anchor, the binding strength decreases to 0.35 eV, and the atoms spontaneously penetrate the hole in the –Si–O– hexagons. The adsorption energy of noble–metal atoms is considerably smaller and amounts to 0.35 eV for Au–Pd_{sub} and 0.19 eV for Ag–Pd_{sub} complexes (virtually no binding without Pd_{sub}). Surprisingly, the atom–atom bond lengths are with 2.54 Å for Au–Pd_{sub} and 2.85 Å for Ag–Pd_{sub} species not much different from the Pd–Pd_{sub}

case and are even close to the values of the corresponding gas–phase dimers (Pd_2, 2.54 Å; Au–Pd, 2.68 Å). In contrast, the binding energy follows an opposite trend for gas–phase (Pd_2, 0.7 eV; Au–Pd, 1.4 eV)[16,17] and surface complexes.

The apparent contradiction between short interatomic distances and low binding energies of the different ad–structures indicates the presence of two competing interaction mechanisms on the silica surface. On the one hand, the adatoms form strong covalent bonds to the Pd_{sub} anchors. On the other hand, this attractive contribution is counterbalanced by the Pauli repulsion that is mainly exerted by the filled $2p$ states of the surface oxygen on the adatom. The repulsion is governed by the spatially most expanded adatom orbital, which is the $5s$ for Pd and Ag and the $6s$ for the Au. Those frontier orbitals hybridize with the O $2p$ states upon adsorption, forming new states of antibonding character (Figure 7.3b). The strength of the repulsion and therefore the adatom–surface interaction is now controlled by the number of electrons in these hybrid states. The Pd $5s$–O $2p$ mixed state is located at $+1.25$ eV above the Fermi level (E_F) and therefore empty, which reduces the repulsion with the oxygen states and allows the formation of a strong Pd–Pd_{sub} bond. The binding energy is even higher than in gas–phase Pd_2, reflecting the stabilization effect of the Mo support. The position of the Pd $5s$–derived state above E_F manifests the charge neutrality of the adatom, as the state is empty in gas–phase Pd, too. The hybrid

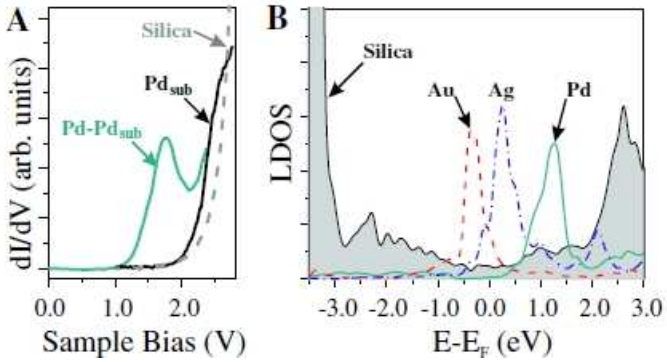

Figure 7.3: (a) dI/dV spectra of a Pd_{sub} , a Pd–Pd_{sub} complex, and the bare silica surface (set point 2.5 V). (b) Calculated state density of the supported silica film (gray region). The line spectra depict the Pd $5s$ (solid line), Ag $5s$ (dash–dotted line), and Au $6s$ (dashed line) contribution to the hybrid state formed with the O $2p$ orbitals, when the respective adatom binds to a Pd_{sub} anchor.

state shows up also experimentally and is assigned to the dI/dV peak at $+1.75$ V observed for Pd–Pd$_{sub}$ complexes (Figure 7.3a).

In contrast, the hybrid state formed between the Ag $5s$ (Au $6s$) orbital and the O $2p$ states is singly (doubly) occupied, as deduced from its calculated energy position at $+0.1$ eV (-0.3 eV) (Figure 7.3b). Because of the vicinity to E_F, they could not be identified in the dI/dV spectra. The electron(s) in the mixed metal–oxygen states induce substantial Pauli repulsion with the silica LDOS, which partly compensates the attractive interaction with the Pd$_{sub}$ and gives rise to the small binding energies of Ag and Au atoms. The effect is larger for Au, because its valence s orbital is doubly occupied ($6s^2$ configuration) as a result of a charge transfer from the Mo support. The formation of anionic Au species has been observed for other oxide films before and manifests the strong electronegative character of gold.[18,19] Instead, the Ag adatom remains neutral on the silica surface, since its $5s$ orbital carries a single electron as in gas–phase Ag. The comparable adsorption energies for Au and Ag atoms, in spite of different repulsive terms, reflect the balancing influence of the metal d states. Whereas the Au $5d$ states considerably strengthen the Au–Pd$_{sub}$ interaction, the Ag $4d$ is too low in energy to participate in the bond formation.

To reduce steric repulsion, the –Si–O– hexagon hosting the Pd$_{sub}$ strongly relaxes upon adatom attachment. The effect is most pronounced for the Au–Pd$_{sub}$ complex due to the double occupancy of the Au $6s$–O $2p$ hybrid state. According to the DFT calculations, the opening in the –Si–O– hexagon enlarges by several tenths of an angstrom ($\sim$5%) and enables the Au to approach the Pd$_{sub}$ anchor. As a result, the Au binding energy increases from 0.14 eV as calculated for a rigid geometry to 0.35 eV after structural relaxation. The ring widening is accompanied by a reduction of the silica LDOS next to the Au–Pd$_{sub}$ binding site, which reflects the decreasing Si–O orbital overlap in the enlarged hexagon.

7.3 Summary

Pd$_{sub}$ atoms incorporated into the nanopores of a thin silica film are able to anchor various adatoms at the originally inert oxide surface. The stabilization effect results from a strong covalent bonding between adatom and embedded Pd$_{sub}$, which is, however, partly compensated by the Pauli repulsion of the filled $2p$ states of the surface oxygen atoms. The strength of the repulsive interaction is dominated by the occupancy of the frontier orbitals of the different adatoms and increases when

going from Pd with an empty valence s state, to neutral Ag and negatively charged Au species with singly and doubly occupied s orbitals, respectively. The ratio between repulsive and attractive terms in the anchoring process thus depends on the electronic properties of the adatoms, introducing a certain chemical sensitivity of the interaction mechanism. The approach described here can be employed to produce even more complex structures via subsequent attachment of different atomic species to the surface anchors. The successful insertion of single–atom binding sites into porous silica films on Mo(112) therefore presents a first step towards the preparation of a functionalized adsorption system.

Bibliography

[1] H. Li, M. Eddaoudi, M. O'Keeffe, and O. M. Yaghi, *Nature* **402** (1999), p. 276.

[2] *Functionalization of Nanomaterials*, edited by C. S. R. Kumar (Wiley–VCH, Weinheim, 2005).

[3] H.–J. Freund, *Surf. Sci.* **601** (2007), p. 1438.

[4] N. Neel, J. Kröger, and R. Berndt, *Appl. Phys. Lett.* **88** (2006), p. 163 101.

[5] J. A. Theobald, N. S. Oxtoby, M. A. Phillips, N. R. Champness, and P. H. Beton, *Nature* **424** (2003), p. 1029.

[6] H. Brune, M. Giovannini, K. Bromann, and K. Kern, *Nature* **394** (1998), p. 451.

[7] C. Becker *et al.*, *New J. Phys.* **4** (2002), p. 75.

[8] S. Bhatia, *Zeolite Catalysis: Principles and Applications* (CRC Press, Boca Raton, FL, 1990).

[9] N. Nilius, T. M. Wallis, and W. Ho, *Science* **297** (2002), p. 1853.

[10] G. V. Nazin, X. H. Qui, and W. Ho, *Science* **302** (2003), p. 77.

[11] J. B. Giorgi, T. Schröder, M. Bäumer, and H.–J. Freund, *Surf. Sci. Lett.* **498** (2002), p. L71.

[12] L. Giordano, A. Del Vitto, and G. Pacchioni, *J. Chem. Phys.* **124** (2006), p. 034 701.

[13] J. X. Wang and J. H. Lunsford, *J. Phys. Chem.* **90** (1986), p. 5883.

[14] M. C. Wu, C. M. Truong, and D. W. Goodman, *Phys. Rev. B* **46** (1992), p. 12 688; B. K. Min, W. T. Wallace, and D. W. Goodman, *J. Phys. Chem. B* **108** (2004), p. 14 609.

[15] M. Sterrer *et al.*, *Angew. Chem., Int. Ed.* **45** (2006), p. 2630.

[16] D. Andrea, U. Haussermann, M. Dolg, H. Stoll, and H. Preuss, *Theor. Chim. Acta.* **78** (1991), p. 246; P. Schwerdtfeger, *Chem. Phys. Lett.* **183** (1991), p. 457; J. Ho, K. M. Ervin, M. L. Polak, M. K. Gilles, and W. C. Lineberger, *J. Chem. Phys.* **95** (1991), p. 4854.

[17] *Handbook of Chemistry and Physics* edited by D. R. Lide (CRC Press, Boca Raton, FL, 1998).

[18] M. Sterrer *et al.*, *Phys. Rev. Lett.* **98** (2007), p. 096107.

[19] N. Nilius *et al.*, *Phys. Rev. Lett.* **100** (2008), p. 096802.

Part III

Modifying properties of ultra–thin oxide films

CHAPTER 8

Defects Centers[†]

The experimental observation that metal clusters (e.g., of Au and Pd) deposited on defect–rich MgO films are catalytically more active than the same clusters deposited on defect–poor MgO films[1–4] has acctracted an increasing interest. In general creating defects could be a suitable way to modify in a controlled way the properties of ultra–thin films.

Scanning tunneling spectroscopy measurements have demonstrated that F centers create energy levels within the band gap of MgO.[5] In the case of ultra–thin films, however, an additional level of complexity is introduced by the fact that the thin oxide film is deposited onto a metal substrate. As reported in Chapter 3 and 4, when the film is particularly thin, a few atomic layers, electron transfer from the oxide surface to the metal support or vice versa can occur. This is due to the fact that the supported metal has empty states which fall below the Fermi level (E_F) of the metal support so that electrons can tunnel from the metal support to the deposited atoms or clusters. Similar effects could also occur for F^0 or F^+ centers. Accurate theoretical calculations have shown that neutral F centers introduce states high in the gap,[6] such that their position could be above that of the Fermi level of the sup-

[†]The results described in this Chapter have been reported in: L. Giordano, *U. Martinez*, G. Pacchioni, M. Watkins and A.L. Shluger, *J. Phys. Chem. C* **112** 3857 (2008)

porting metal. This may result in an intrinsic instability of neutral F centers created on ultrathin MgO films and in their spontaneous conversion into paramagnetic F^+ centers. On the other hand, one can ask whether F^+ centers can exist on an ultrathin MgO film if their unoccupied state falls below E_F? This can induce charge transfer from the metal support to the vacancy with formation of neutral F centers. In a similar case of SiO_2 single–layer films grown on Mo(112), DFT calculations have shown that the nonbridging oxygen center, $\equiv$Si–O$^\bullet$, a typical defect on the surface of silica, spontaneously transforms into the silanolate anion, $\equiv$Si–O$^-$, by capturing of one electron from the metal support.[7]

In this chapter is described the electronic structure of F and F^+ centers in ultrathin MgO films on two metal substrates. As discussed above, the number of electrons in the vacancy is determined by the position of the defect level with respect to the Fermi level of metal substrate. This, in turn, can be affected by several factors: metal work function, film thickness, position of the vacancy inside the film and with respect to different surface features, such as steps, edges, and corners. We have performed plane waves DFT calculations on oxygen vacancies formed in MgO films on two substrates with different work function, MgO/Ag(100) and MgO/Mo(100), and analyzed their electronic structure as a function of position and film thickness.

The Section 8.2 has been divided into six parts: a brief review of the structure of F and F^+ centers on the MgO(100) surface; role of the metal substrate (Ag vs Mo) on the stability of F centers created on three–layer MgO films; role of the position in the film on the stability of F centers (surface, bulk, interface); role of film thickness (three layers vs two layers of MgO); role of low–coordinated sites (steps); role of strain in the film.

8.1 Computational Details

In this chapter we discuss the energetically preferable stationary charge states of a defect at a particular position in a film and do not consider lifetimes of transient charge states created by irradiation or electron transfer from an STM tip. To this end, we performed plane wave gradient corrected density functional theory (DFT) calculations using the VASP code (see section 2.1.1, page 25). The positions of atoms are relaxed until the atomic forces are less than 0.01 eV/Å.

We used 3×3 supercells to model two (2L) or three (3L) layers of MgO deposited on four Ag or Mo layers representing the Ag(100) and Mo(100) substrates, respec-

tively. During geometry optimization, all atoms in the MgO film and in the two metal layers nearest to the interface were relaxed while atoms in the remaining two metal layers were frozen at their bulk positions. For comparison, an unsupported MgO 3L slab computed at the lattice constant of Ag has been considered. Here the bottom layer was kept fixed during the geometry optimization.

Oxygen vacancies were created by removing an O atom and by relaxing the resulting defect. Various sites were considered on a MgO(3L)/Ag(100) film: surface (first layer), "bulk" (second layer), and interface (third layer). In 2L MgO films, only the surface defects were considered. Low–coordinated F centers were investigated using a supercell where steps were created in a MgO(3L)/Ag(100) film.

Neutral F^0 centers were considered in the closed shell singlet configuration (no unpaired electrons), in a spin–polarized calculation with two unpaired electrons in the unit cell (we will refer in the following to this as the "triplet" configuration although of course this does not correspond to a pure spin state), and in a second spin–polarized calculation where the number of unpaired electrons is determined self–consistently. To simulate a paramagnetic F^+ center we used two approaches. In one approach, the divalent Mg atom under the missing oxygen was replaced by a monovalent Na atom. The resulting system is globally neutral but contains only one trapped electron in the cavity, as described in previous papers.[8–10] We denote this center as $F^\bullet$(Na). In the second approach, an F^+ center was obtained from a neutral F center by removing one electron from the periodic cell and calculating a spin–polarized solution. To keep the electrical neutrality of the whole system, a uniform neutralizing background of charge has been added.

To ease the constraints imposed by fixing metal layers in geometry optimization, we have also used a replicated cluster approach, where a MgO cluster was deposited on the top of a bigger Ag cluster modeling the Ag substrate. In this case the Quickstep code, the DFT part of the cp2k suite,[11,12] was used to reduce computational demands. The calculations were carried out within a large periodic cell ($35\times35\times27$ Å^3) to minimize interactions between replicated clusters. Double–ζ polarization (DZVP) quality Gaussian basis sets were used with a 300 Ry plane wave cutoff for the auxiliary basis set. The PBE exchange–correlation functional[13] was used, and geometries were relaxed until forces on all atoms were below 0.025 eV/Å.

A word of caution is required about the accuracy of the results presented below. Since the DFT method is not suited for computing excited electronic states, some systematic errors may occur when the Kohn–Sham eigenvalues are used to estimate the relative positions of the metal work function, Φ, the top of the O $2p$ valence band,

the bottom of the conduction band, and that of the empty or filled states of the defects. The error is not necessarily the same for all these quantities as it depends upon the localization of the quasi–particle wave functions, which are different for different materials and systems and also for different exchange–correlation functionals. So, although the general concepts discussed here about the relative stability of F^0 and F^+ centers should be valid and may apply to any metal/oxide interface, specific predictions regarding stability of the two centers may depend on the details of the oxide/interface electronic structure.

8.2 Results and Discussion

8.2.1 Surface F Center Defects on MgO(100)

The electronic structure of F^0 and F^+ centers on the MgO(100) surface has been addressed in a number of papers,[6,14–20] and here we restrict the discussion to those aspects which are needed for comparison with the properties of supported MgO films on Ag(100) or Mo(100). The formation energy of the F^0 center, computed with respect to the perfect relaxed MgO(100) surface and $1/2$ O_2 or that of an O atom, is 6.32 and 9.48 eV, respectively, in line with previous calculations.[6,19] The creation of an F^0 center (singlet state) is not accompanied by a significant surface relaxation, with displacements of the surface atoms around the vacancy of about 0.06 Å (3% of the Mg–O distance, Figure 8.1a). The calculation of the formation energy of an F^+ center is impossible in our approach since in one case the addition of the neutralizing background of charge introduces a spurious interaction, and in the other, $F^\bullet$(Na), the composition changes as one Mg atom is replaced with a Na atom. The structural relaxation associated with the formation of the paramagnetic $F^\bullet$(Na) and F^+ centers is similar, about 6–7%, in line with previous calculations, exhibiting a more pronounced lattice distortion around the singly occupied vacancy, Figure 8.1, parts b and c.

All centers considered on the terraces of the MgO(100) surface, F^0, $F^\bullet$(Na), and F^+, introduce new states in the band gap. F^0 gives rise to a doubly occupied state at 2.15 eV above the top of the valence band, Figure 8.1a. The corresponding electron density plot clearly shows a significant electron density inside the vacancy, Figure 8.1a. An F^0 center is characterized by empty excited states below the bottom of the MgO conduction band. In particular, cluster model configuration interaction calculations[21–23] predict that the lowest singlet–triplet transition in a surface F^0 cen-

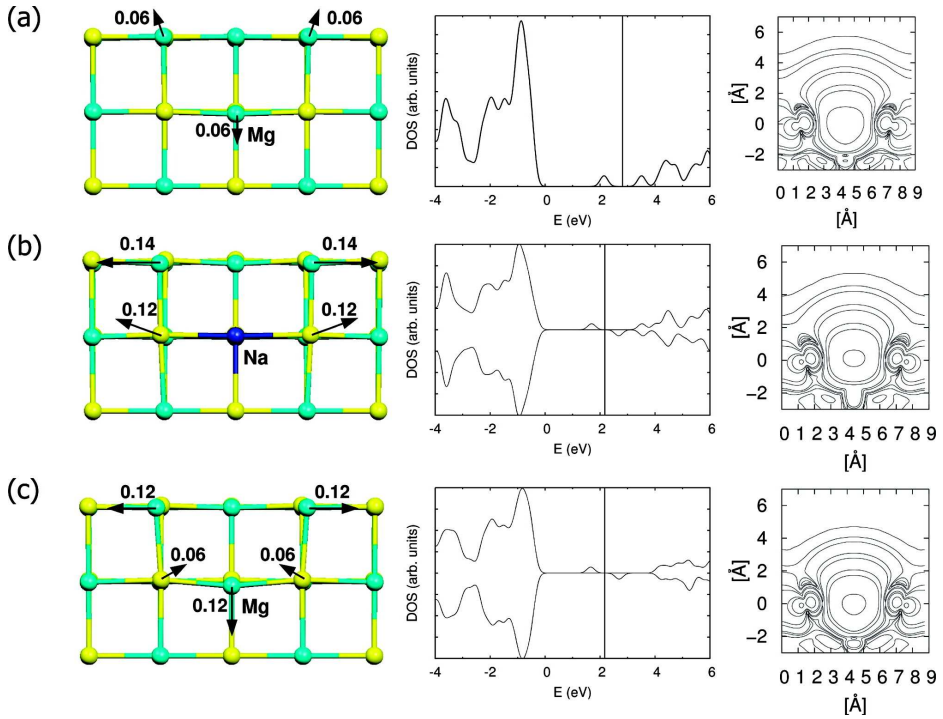

Figure 8.1: Structural relaxation (side view, left), DOS curves (center), and electron density plot of the state in the gap (right), for (a) F^0 (singlet) center, (b) $F^\bullet$(Na) center, and (c) F^+ center on the MgO(100) surface. Atomic displacements are in angstroms. In the DOS curves the zero level is positioned at the top of the valence band, while the vertical line indicates the Fermi level. The isodensity curves displayed in the contour plot (in $e/\text{Å}^3$) are as follows: 10^{-5}, $5{\times}10^{-5}$, 10^{-4}, $5{\times}10^{-4}$, 10^{-3}, $5{\times}10^{-3}$, 10^{-2}, $5{\times}10^{-2}$. The zero vertical height is positioned on the surface layer.

ter has s–p character and occurs at 1.93 eV. In our calculations, however, the empty F^0 center states artificially occur above the conduction band minimum because the band gap of MgO is underestimated in the PW91 functional. This deficiency of DFT is even more pronounced in the triplet (excited) state of the surface F^0 center. The total energy of this state is 1.54 eV higher than that for the F^0 (singlet) ground state, but the relaxation around the defect is very similar to that found for $F^\bullet$(Na) and F^+ centers, with displacements of neighboring Mg ions of about 6–7% a. This reflects the fact that only one out of two electrons remains trapped in the vacancy and gives

rise to a level in the gap about 1.6 eV above the top of the valence band; the second electron is delocalized over the 3s states of the Mg atoms of the bottom layer where it induces a partial spin polarization of the oxygen atoms, Figure 8.2a. Thus, it is not surprising that both the geometric and electronic structures of the F^0 (triplet) are similar to those of the $F^\bullet$(Na) and F^+ defects. Both centers give rise to a singly occupied level at about 1.6 eV above the top of the valence band, Figure 8.1, parts b and c. Also the charge densities of $F^\bullet$(Na) and F^+ are very similar, Figure 8.1, parts b and c. The basic similarity of F^0 (triplet) and F^+ centers is evident from a plot of their spin densities in the MgO top layer. As one can see in Figure 8.2 they are nearly identical. The main difference between $F^\bullet$(Na) and F^+ models is that in the second case the energy gap is about 0.6 eV higher because the bottom of the conduction band is shifted to higher energies because high concentration of the Na^+ cation induces some lattice distortions due to its larger ionic radius.

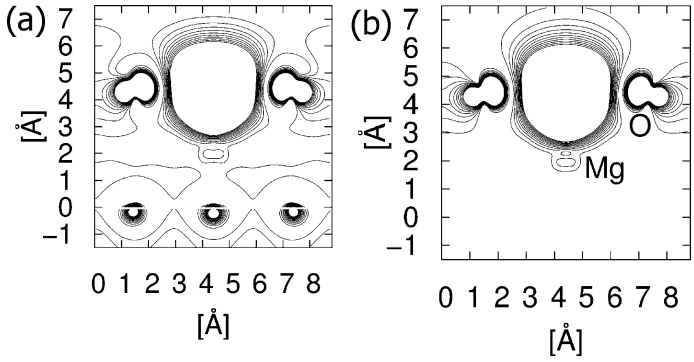

Figure 8.2: Spin density plot for (a) F^0 (triplet) and (b) F^+ centers on MgO(100). The separation between consecutive isodensity curves is 10^{-3} $e/\text{Å}^3$. The zero vertical height is positioned on the bottom MgO layer.

8.2.2 Role of the Metal Substrate

In this chapter we consider thin films of MgO adsorbed on two different metallic substrates, Ag and Mo. The MgO/Ag(100) and MgO/Mo(100) interfaces exhibit different properties, in particular adhesion energies and interface distances.[24] This results in different work functions and alignments of the F centers states with respect to the metal Fermi level. In particular, in MgO/Mo(100), where the interface distance is considerably shorter, there is a strong reduction of the metal work func-

tion, $\Delta\Phi$=−2.1 eV, compared to clean Mo(100). In MgO/Ag(100) $\Delta\Phi$ is −1.2 eV.[19] This means that the Fermi level in MgO/Mo(100) is about 1 eV higher in energy compared to that in a MgO film of the same thickness deposited on Ag(100).

We start our discussion by considering the properties of an F^0 (singlet) center created in the top layer of a MgO(3L)/Ag(100) film. The formation energies, 6.27 eV with respect to $1/2\,O_2$ and 9.44 eV with respect to atomic oxygen, are very similar to those for the unsupported MgO(100) slab. Also, the geometrical relaxation is similar, Figure 8.3a, suggesting close similarity of the two defects. However, the analysis of the density of states curves shows some important differences. The creation of an F^0 (singlet) center results in a new state 2.35 eV above the top of the O 2p valence band, Figure 8.4a, i.e., just 0.16 eV below the Fermi level of the Ag(100) substrate. This indicates that the defect may be metastable with respect to the formation of a singly occupied vacancy (F^+) and the transfer of one electron into the Ag conduction band (see below).

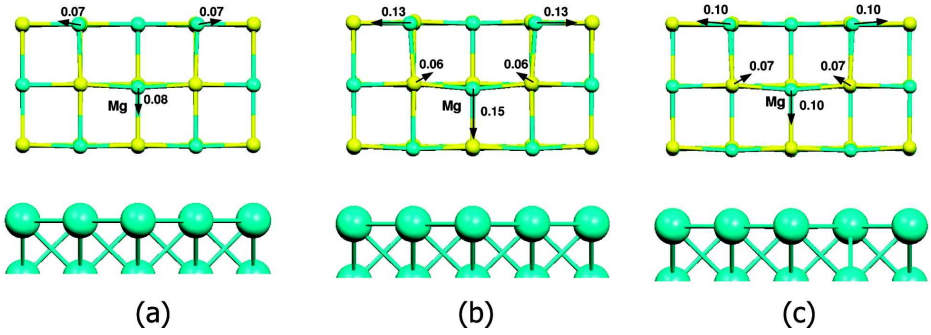

Figure 8.3: Side view of the local relaxation of (a) F^0 (singlet), (b) F^+, and (c) F^0 (triplet) centers on a MgO(3L)/Ag(100) supported film. Atomic displacements are in angstroms.

The DOS curves for an F^+ center on the surface of a MgO(3L)/Ag(100) film show a singly occupied state in the gap about 2.05 eV above the top of the O 2p valence band, Figure 8.4b. Thus, there is a shift toward the center of the gap by about 0.3 eV compared to the unsupported MgO film. The α component of the impurity state is 0.6 eV below the E_F(Ag), whereas the corresponding β component is about 0.5 eV above it. The result points toward an intrinsic stability of the F^+ center even in the presence of the metal substrate; in fact, there is no spontaneous charge transfer from the Ag metal to the empty β component of F^+, a process which would lead to the formation of a neutral vacancy. We believe that this is not induced artificially by the

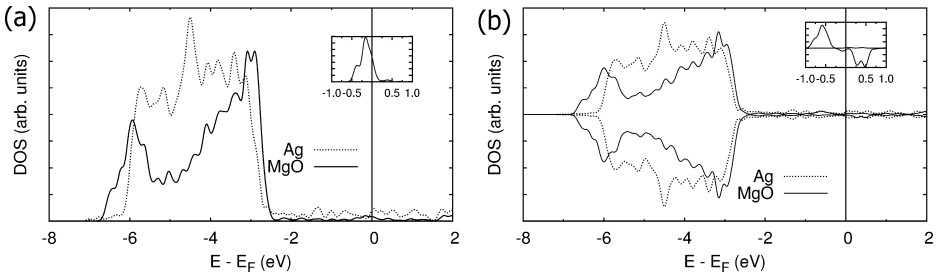

Figure 8.4: DOS curves for (a) an F^0 (singlet) center and (b) an F^+ center formed on a MgO(3L)/Ag(100) film. The inset shows the contribution of the F center ($\times$15). Dotted line, Ag(100); solid line, MgO.

use of a homogeneous background of charge in the treatment of the F^+ center: the electronic structure of the neutral $F^\bullet$(Na) center is virtually identical. The relaxation around F^+, Figure 8.3b, is similar to that found for the bare MgO(100) surface (about 6–7%). This strong lattice distortion contributes to stabilizing the singly occupied defect center. Furthermore, the formation of what is formally a positive defect, F^+, induces a polarization response in the metal support (image interaction), which also contributes to stabilizing the singly occupied vacancy.

To check the stability of the doubly occupied F^0 center on MgO(3L)/Ag(100) we consider the triplet state. The spin density for this state clearly shows that one electron is trapped in the cavity while the second one is delocalized in the Ag metal support, Figure 8.5a. Differently from the MgO(100) slab, where F^0 (triplet) is 1.5 eV higher in energy than F^0 (singlet), here the two states are nearly degenerate with the singlet only 0.03 eV more stable than the triplet. Thus, the two configurations with one or two electrons in the cavity are nearly isoenergetic due to the presence of the Ag substrate which serves as an electron reservoir. A further proof of the role played by the Ag metal comes from a spin–polarized calculation where no constraint was imposed on the number of unpaired electrons: this state is slightly lower in energy (0.08 eV) and shows a spin polarization of about 0.6 electrons. The fact that this solution is the lowest one further supports the metastable nature of the diamagnetic F^0 center on a MgO(3L)/Ag(100) film. Both the electronic and geometric structures of the F^0 (triplet) center on the MgO/Ag(100) film coincide with those of a classical F^+ center. For instance, the spin density plots of F^0(triplet) and F^+ states in the MgO top layer are almost identical, Figure 8.5.

In contrast, due to the significantly higher position of the Fermi level in Mo rel-

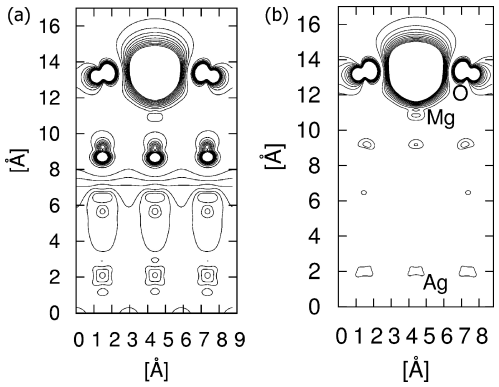

Figure 8.5: Spin density plot for (a) F^0 (triplet) and (b) F^+ centers on MgO(3L)/Ag(100). The separation between consecutive isodensity curves is 10^{-3} $e/\text{Å}^3$. The zero vertical height is positioned on the bottom Ag layer.

ative to Ag, the F^0 doubly occupied impurity level in MgO(3L)/Mo(100) is well below the Fermi level, Figure 8.6, whereas it is at E_F in MgO(3L)/Ag(100), Figure 8.4a. The F^0 (singlet) defect is therefore stable, at variance with the corresponding center in MgO/Ag(100). To further prove this, we have considered the F^0 (triplet) state in MgO(3L)/Mo(100): its energy is similar to that of the singlet ground state, but when a triplet solution is enforced, the system generates two unpaired electrons in the Mo metal, while the two electrons in the MgO vacancy remain with their spin paired (singlet closed shell). This clearly shows that it is energetically unfavorable to excite one electron from the F^0 center to the metal. On the other hand, in the F^+ center calculation an electron is spontaneously transferred from the Mo metal so that two electrons occupy the vacancy. In other words, an F^+ center in the top layer of the MgO/Mo(100) film is unstable because the corresponding level is well below the metal Fermi level.

This comparison between different metal supports shows unambiguously that the stability or instability of an F center created on a thin MgO film depends strongly on the metal/oxide interface and on how this affects the position of the Fermi level of the system. It is also clear that the MgO/Ag(100) system could be extremely sensitive to the local environment of the F center. In the next section we examine this case in detail.

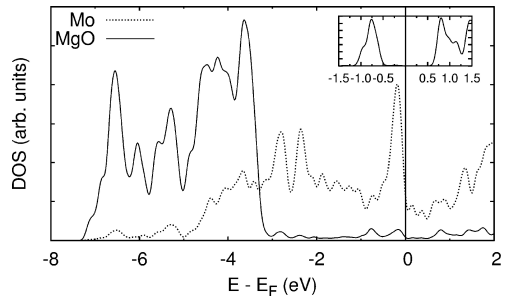

Figure 8.6: DOS curves for an F^0 (singlet) center formed on a MgO(3L)/Mo(100) film. The inset shows the contribution of the F center ($\times$15). Dotted line, Mo(100); solid line, MgO contribution.

8.2.3 MgO(3L)/Ag(100) Thin Films: The Role of Local Structure

There are three nonequivalent sites for oxygen vacancies within the perfect three layers MgO/Ag(100) film: at the surface, in the second "bulk" layer, and in the third layer at the interface with the metal. The previous section has shown that for the surface vacancy there is an extremely fine energetic balance between the relative stabilities of F^0 and F^+ centers. Here we examine further the effect of the local environment on the stability of the F center charge state and quantitatively analyze the electron distribution associated with different defects.

The instability of the F^0 center is even more pronounced when the defect is created in the second layer of MgO(3L)/Ag(100) ("bulk" F^0 center). We considered singlet closed shell and spin–polarized solutions and found that the latter is more stable by 0.28 eV with a spin population of 0.88 electrons inside the vacancy. The tendency toward a paramagnetic solution is thus even more pronounced for the internal than for the top layer. The second electron formally associated with the vacancy is delocalized over the Ag metal, and what is left is effectively a "bulk" F^+ center with only one trapped electron.

The F^0 center created at the MgO(3L)/Ag(100) interface (third layer) has the lowest formation energy, 4.95 eV relative to 1/2 O_2 (see also Refs.[25] and [26]). As found in previous studies, the charge density is largely delocalized into the metal substrate. A rough estimate shows that no more than one electron is present in the vacancy in this position, the rest being distributed on the Ag metal. The charge density in the vacancy is thus very similar to that of F^+, but the center is not paramagnetic because of the coupling of the trapped electron with the Ag valence band

states.

To obtain a more quantitative estimate of the number of electrons associated with F^0 center created in various positions of the MgO films (supported and unsupported) we have performed an integration of the charge in spheres centered at the vacancy with radii up to 2 Å; this has to be compared with the density in a sphere of the same size for the ideal nondefective system. To this end we have subtracted the density of the ideal case (O^{2-}) from that of the vacancy, adding the six valence electrons of oxygen:

$$\Delta\rho(r) = \rho(vacancy) - \rho(O^{2-}) + \rho(O_{2s,2p}) \tag{8.1}$$

In this way we can evaluate to which extent the number of electrons associated to the vacancy is close to two. For the ideal case of an F^0 center (two trapped electrons), $\Delta\rho$(r) should converge to zero as the radius of integration includes all electron density associated with the vacancy; this occurs at approximately the nearest neighbor Mg ions for F^0 center in bulk MgO. For an F^+ center with only one electron in the cavity $\Delta\rho$ should converge to -1. In general, negative values in the region between 1 and 2 Å indicate that the number of trapped electrons is smaller than that expected for a "classical" diamagnetic F center.

As expected, nearly two trapped electrons are associated with the F^0 (singlet) center in bulk MgO, Figure 8.7a. However, the same center formed in the second layer of the MgO(3L)/Ag(100) film ("bulk" F^0) shows a density of only 1.3 electrons, very similar to that computed for the bulk F^+ center in MgO. This result shows unambiguously that the nature of an F^0 defect in bulk MgO is different from that of an equally coordinated defect on a supported ultrathin MgO film: in the latter case one electron is in fact transferred spontaneously to the Ag substrate. This confirms that the F^0 center in the central layer is unstable and transforms spontaneously into the paramagnetic F^+ defect. As a further test of the stability of the F^+ defect we added or removed an electron from our simulation cell. The charge densities for the three cells lie almost on top of each other, demonstrating that the metallic substrate acts as an electron reservoir effectively deciding the charge state of the F center: electrons added or removed from the system come from or go to the Fermi level of the metal leaving the F^+ center virtually unchanged.

When performing similar analysis for an F^0 (singlet) center on the surface of the MgO(3L)/Ag(100) film we compare with an F^0 center on the surface of MgO(100), Figure 8.7b. The integration procedure illustrated above shows that the number of electrons associated with a five–coordinated F^0 center on MgO(100) is smaller than

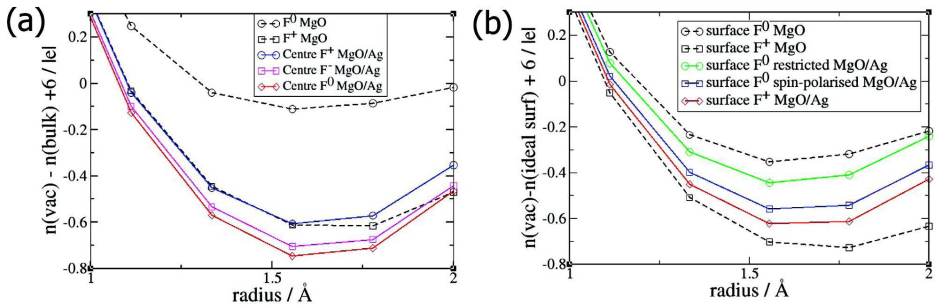

Figure 8.7: Charge density difference analysis $\Delta\rho(r) = \rho(vacancy) - \rho(O^{2-}) + \rho(O_{2s,2p})$ for (a) "bulk" and (b) surface F centers.

two (about 1.7 e) because the charge spills over from the surface and extends toward the vacuum (see Figure 8.1a). This is not the case for F^+ on MgO(100) since here the charge is more localized: about 1.1 electron is associated with this center, Figure 8.1c. If we now consider the F^0 (singlet) center on the top layer of MgO(3L)/Ag(100), the result is very close to that found for MgO(100), Figure 8.7b. However, if we consider the more stable spin–polarized solution, the charge associated with the vacancy is intermediate between that for F^0 (close to two electrons) and F^+ (close to one electron). This is an additional proof of the metastability of the F^0 center created on the top layer of a MgO(3L)/Ag(100) film. This result shows that the stability of F^0 centers depends on the position where they are formed (surface or "bulk") and suggests that it may also change with the film thickness, an aspect that will be discussed in the following section.

8.2.4 MgO(2L)/Ag(100) Thin Films: The Role of Film Thickness

We consider now the nature of F^0 and F^+ centers created on the top layer of MgO(2L)/ Ag(100). We have shown above that surface F^0 and F^+ centers formed on MgO(3L)/ Ag(100) are close in energy. Here, for the thinner film, the defect is still formed on the surface, but the defect charge density can better overlap with that of the metal. This, together with the stronger interaction of the formally positively charged center with the corresponding image charge, can further contribute to stabilizing the singly occupied vacancy.

We start with the F^0 (singlet) center. The geometry optimization, Figure 8.8a, shows a strong relaxation of the atoms around the cavity, similar to an F^+ center.

Performing the calculation in a spin–polarized way or for a triplet state, we found essentially the same geometrical structure, see Figure 8.8, parts b and c, respectively. Notice the particularly strong relaxation, by about 0.3 Å, of the Mg ion at the bottom of the vacancy toward the metal substrate. The similar structure obtained for the three calculations is indicative of the fact that the F^0 center created on a 2L MgO film differs from the same center created on thicker films or on MgO(100). This is clearly shown by the DOS plot, Figure 8.9. The defect state is crossed by the Fermi level, Figure 8.8a, showing that it is unstable toward the transfer of one electron to the Ag conduction band. The spin density plot for the F^0 (triplet) solution confirms that one unpaired electron is in the cavity, while the other one is delocalized over the Ag substrate (the corresponding plot is similar to that of Figure 8.5). The only difference between F^0 (singlet) and F^0 (triplet) states is the spin coupling of the electrons trapped in the cavity with those of the Ag metal (antiparallel or parallel, respectively). In this respect, the most appropriate description is provided by the spin–polarized calculation, which in the DOS curves shows the presence of filled and empty components just around E_F, Figure 8.9b, and the same spin density of a normal F^+ center.

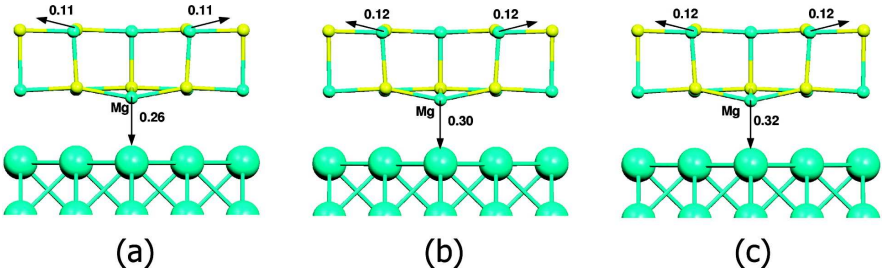

Figure 8.8: Side view of the local relaxation of (a) F^0 (singlet) center, (b) F^+ center (spin polarized), and (c) F^0 (triplet) center on a MgO(2L)/Ag(100) supported film. Atomic displacements are in angstroms.

8.2.5 MgO/Ag(100) Thin Films: Vacancy at Step Edges

Experiments on thin MgO films have shown that upon electron bombardment point defects (oxygen vacancies) are created almost exclusively along the step edges.[5,27] So far our discussion has been restricted to flat terraces. Here we extend the analysis to an O vacancy at a step edge on a MgO(3L)/Ag(100) film. In the unsupported

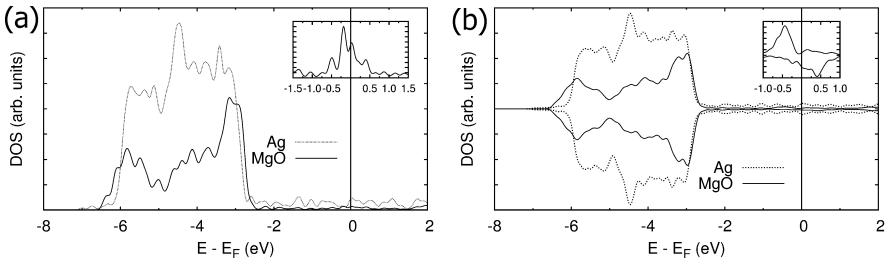

Figure 8.9: DOS curves for (a) an F^0 center and (b) an F^+ center formed on a MgO(2L)/Ag(100) film. The inset shows the contribution of the F center ($\times$15). Dotted line, Ag(100); solid line, MgO.

MgO(100) slab, the creation of a vacancy on a step–edge O leads to the creation of a localized state 2.5 eV above the MgO valence band (F^0 singlet). This level is about 0.2 eV higher in energy than that for the MgO terrace, and consequently, its positioning relative to the Fermi level of Ag will be slightly altered; in particular, we expect this center to more easily lose an electron to the metal support. The step edge is formed by the removal of half of the top layer of MgO to form upper and lower terraces the width of three Ag atoms in the support (6.4 Å), Figure 8.10. The formation of a step–edge vacancy on the supported film costs 5.27 eV with respect to the ideal stepped MgO film and 1/2 O_2. The formation energy at the edge site of the thin film is by 1 eV less than the energy required for vacancy formation on the equivalent terrace, which is similar to the difference in formation energies of F centers at terrace and step–edge sites in bulk MgO.[19,20] However, the step–edge vacancy on the MgO(3L)/Ag(100) film is not the most favorable location for an oxygen vacancy, as might be expected from the lower coordination of the oxygen removed. Instead, the interface F center is favored by 0.3 eV, showing the strong interaction with the underlying metal support. The structural relaxation of the step–edge vacancy is shown in Figure 8.10 and is significantly larger than that found for bulk or terrace vacancies. The energy of a spin–polarized solution for the step–edge vacancy is 0.01 eV below that for the restricted solution, with 0.31 excess α spin electrons.

8.2.6 MgO/Ag(100) Thin Films: Isolated Islands and Stress Effects

One factor thus far not considered is the possible effect of the periodic boundary conditions used in our calculations. The MgO thin film is forced into compression

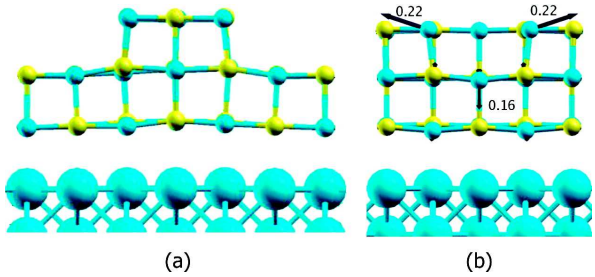

Figure 8.10: Side view of (a) the structure of a stepped MgO/Ag(100) film and (b) relaxations of Mg ions surrounding a step–edge vacancy site. Atomic displacements are in angstroms.

(∼2%) by the requirement of epitaxy with the metal support: this is realistic; however, in practice there are defects within the film to relieve this stress and MgO films are usually polycrystalline.[5,27] To investigate the possible implications of the stress induced by the ideal periodic model we have carried out calculations on isolated nanoparticles of silver topped with small MgO islands. The silver nanocluster is formed of 164 Ag atoms in three layers. These layers were cut from our periodic simulations, and then the geometry was relaxed to a local minimum. On the top surface of this silver nanocluster 1.2 nm^2 islands of MgO were placed, two or three layers deep. Figure 8.11 shows the structure of the ideal two–layer system. To reduce the cost of these calculations, the cp2k[11,12] program was used, which combines a local Gaussian basis set with a plane wave auxiliary basis set.

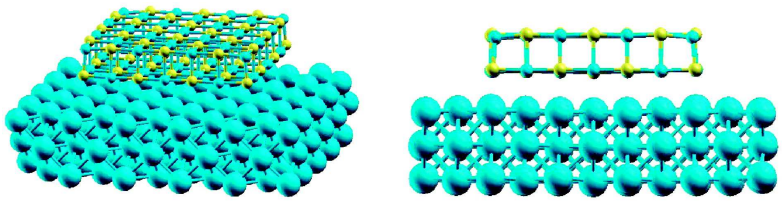

Figure 8.11: Geometry of the two–layer MgO island on a silver cluster.

The structure of the ideal MgO islands on the Ag cluster is similar to that observed in our periodic calculations but with some inward relaxations of the undercoordinated atoms at the edges and corners of the island. The interface oxygen atoms are still in perfect registry with the top layer of Ag with Ag–O bond lengths

close to those observed in the periodic model, 2.63 Å for the Ag–O bond at the center of the island.

The MgO island offers several possible sites for the creation of oxygen vacancies: we have considered the energetic cost for the creation of interface, terrace, edge, and corner oxygen vacancies. The formation energies of these species are compiled in Table 8.1. The results show a striking similarity in formation energies of similar vacancy sites calculated using the different models and display a clear trend. The formation energy of oxygen vacancies at the interface of MgO/Ag(100) films (computed with respect to $1/2\ O_2$) is almost independent of the system and costs ∼4.9 eV; similarly, creation of a vacancy at a five–coordinated terrace site costs ∼6.1 eV. Four–coordinated oxygen sites are more readily formed than those on the terrace at ∼5.4 eV. It is noticeable that a three–coordinated corner vacancy site appears to be slightly energetically favorable compared to a vacancy at the interface. These results are in line with those reported previously for similar centers.[19,20]

Table 8.1: Oxygen vacancy formation energies (in eV) for different surface sites calculated using the periodic slab and periodic cluster models[a].

	model		
vacancy site	periodic model (3L)	2L island	3L island
terrace	6.27	5.94	6.09
edge		5.38	5.49
step–edge	5.37		5.46
corner			4.62
interface	4.95	4.90	4.85

[a] Formation energies are relative to the ideal MgO/Ag system and the vacancy and $1/2\ O_2$.

There are many differences in both the calculation details and the local environment for the systems considered; hence, to some degree, the excellent agreement in formation energies between the periodic and cluster models may be a result of error cancellation. However, the results suggest that the stress induced by growth on the Ag substrate is not an especially significant factor in the formation of F centers in/on the MgO/Ag films and that the silver substrate exhibits essentially bulk behavior within a relatively small cluster. Particularly, the stabilization of interface vacancy sites seems to be caused by the local coordination to silver which is evi-

denced in the large relaxation energies of these defects, ∼1.5 eV. The results agree with the observation that electron bombardment principally causes damage at edge and corner sites, though buried interface vacancies are thermodynamically more stable than edge or step–edge sites.

8.3 Summary

The unusual properties of ultrathin films deposited on metal substrates open a number of questions related to their behavior in chemisorption and reactivity but also regarding the stability of intrinsic defects with respect to their bulk counterparts. The electron transfer to molecular species or metallic clusters with high electron affinity adsorbed on the surface of 2L–3L MgO films on Ag(100) or Mo(100) has been predicted theoretically and demonstrated experimentally (see Chapter 3). This is due to the fact that the adsorbed species have empty states which fall below the Fermi level of the metal support and can be filled via direct tunneling of electrons through the thin insulating film. Point defects created at the surface or in the interior of the oxide film (in particular O vacancies) can act in the same way, as they also introduce filled and empty states in the band gap. Stationary electronic states formed as a result of the interaction of these defect states with the metal electrons of the support were investigated here on the example of oxygen vacancies in a supported MgO film.

The results clearly show that in some conditions the neutral doubly occupied F^0 center is metastable or unstable and transforms into the paramagnetic F^+ center. This occurs when the defect state induced by the F^0 center in the band gap is very close to the metal Fermi level, a condition which is fulfilled for MgO films on Ag(100). The phenomenon is enhanced when the vacancy is closer to the interface, as in two–layer MgO films or for vacancies formed in the internal layer of a three–layer MgO film. The effect may change with increasing film thickness and converge to the typical stability of F^0 compared to F^+ on the surface of MgO(100). We note that the observed stability of F^+ centers is enhanced by the strong lattice distortion, which always accompanies the formation of charged vacancies. Another reason is that the presence of only one electron in the cavity results in a modification of the local potential of MgO and in a formal positive charge in the insulating film. This charge induces polarization of the metal support, which acts to stabilize the defect. On MgO/Mo(100) films, where the Fermi level is at higher energies, F^0 centers are

stable and do not show a tendency to transforming into F^+. On the contrary, F^+ centers can transform spontaneously into neutral F^0 centers by capturing an electron from the Mo substrate. These conclusions seem to apply for F centers formed on flat terraces as well as on step edges.

Finally we note that our calculations do not address an important question of a lifetime of some particular charge state of a defect created by irradiation, electron transfer from an STM tip, or by other means. This lifetime would of course depend on the defect position with respect to metal, i.e., film thickness. Our results determine only the energetically preferable charge state of a defect at a particular position in a film which may result from several electron–transfer events accompanying the film charging.

Bibliography

[1] B. Yoon, H. Häkkinen, U. Landman, A. S. Worz, J. M. Antonietti, S. Abbet, K. Judai, U. Heiz, *Science* **307** (2005), p. 403.

[2] A. Sanchez, S. Abbet, U. Heiz, W. D. Schneider, H. Häkkinen, R. N. Barnett, U. Landmann, *J. Phys. Chem. A* **103** (1999), p. 9573.

[3] A. Sanchez, S. Abbet, U. Heiz, W. D. Schneider, A. M. Ferrari, G. Pacchioni, N. Rösch, *J. Am. Chem. Soc.* **122** (2000), p. 3453.

[4] S. Abbet, E. Riedo, H. Brune, U. Heiz, A. M. Ferrari, L. Giordano, G. Pacchioni, *J. Am. Chem. Soc.* **123** (2001), p. 6172.

[5] M. Sterrer, M. Heyde, M. Novicki, N. Nilius, T. Risse, H. P. Rust, G. Pacchioni, H.–J. Freund, *J. Phys. Chem. B* **110** (2006), p. 46.

[6] P. V. Sushko, A. L. Shluger, C. R. A. Catlow, *Surf. Sci.* **450** (2000), p. 153.

[7] U. Martinez, L. Giordano, G. Pacchioni, *J. Phys. Chem. B* **110** (2006), p. 17015.

[8] L. M. Molina, B. Hammer, *J. Catal.* **233** (2005), p. 399.

[9] M. Ménétrey, A. Markovits, C. Minot, A. Del Vitto, G. Pacchioni, *Surf. Sci.* **549** (2004), p. 294.

[10] A. Del Vitto, L. Giordano, G. Pacchioni, U. Heiz, *J. Phys. Chem. B* **109** (2005), p. 3416.

[11] J. VandeVondele, J. Hutter, *J. Chem. Phys.* **118** (2003), p. 4365.

[12] J. VandeVondele, M. Krack, F. Mohamed, M. Parrinello, T. Chassaing, J. Hutter, *Comput. Phys. Commun.* **167** (2005), p. 103.

[13] J. P. Perdew, K. Burke, M. Ernzerhof, *Phys. Rev. Lett.* **77** (1996), p. 3865.

[14] A. M. Ferrari, G. Pacchioni, *J. Phys. Chem.* **99** (1995), p. 17010.

[15] E. Castanier, C. Noguera, *Surf. Sci.* **364** (1996), p. 1.

[16] E. Scorza, U. Birkenheuer, C. Pisani, *J. Chem. Phys.* **107** (1997), p. 9645.

[17] G. Pacchioni, *Chem. Phys. Chem.* **4** (2003), p. 1041.

[18] M. Menetrey, A. Markovits, C. Minot, G. Pacchioni, *J. Phys. Chem. B* **108** (2004), p. 12858.

[19] G. Pacchioni, P. Pescarmona, *Suf. Sci.* **412/413** (1998), p. 657.

[20] H.–J. Freund, *Surf. Sci.* **601** (2007), p. 1438.

[21] F. Illas, G. Pacchioni, *J. Chem. Phys.* **108** (1998), p. 7835.

[22] C. Sousa, G. Pacchioni, F. Illas, *Surf. Sci.* **429** (1999), p. 217.

[23] C. Sousa, F. Illas, *J. Chem. Phys.* **115** (2001), p. 1435.

[24] L. Giordano, F. Cinquini, G. Pacchioni, *Phys. Rev. B* **73** (2005), p. 045414.

[25] L. Giordano, J. Goniakowski, G. Pacchioni, *Phys. Rev. B* **67** (2003), p. 045401.

[26] J. Carrasco, N. Lopez, F. Illas, H.–J. Freund, *J. Chem. Phys.* **125** (2006), p. 074711.

[27] M. Sterrer, E. Fischbach, T. Risse, H.–J. Freund, *Phys. Rev. Lett.* **94** (2005), p. 186101.

CHAPTER 9

Modifying the work function by adsorption of alkali atoms[†]

In the first part of the thesis it was shown what the modification of the metal/oxide work function is that an essential parameter to determine the properties of deposited metal atoms, and ways to tune the work function in a controlled way are highly desirable.

Alkali metal atoms deposited on a metal surface are known to produce deep changes in Φ as a function of the coverage.[1] The classical picture proposed by Kingdom and Langmuir[2] and by Gurney[3] is that Φ decreases for a positive adsorbate on a metal since an image charge forms into the bulk metal giving rise to a dipole layer which the emitted electron must pass through.[4] Since alkali metal atoms deposited on a metal surface easily form cationic species, the global effect is a large change in Φ, $\Delta\Phi$. For K atoms on Pt(111), $\Delta\Phi$ is more than 4 eV,[5] Figure 9.1a. Much less is known in terms of alkali atoms deposited on oxide surfaces. Here we have to distinguish between reducible and nonreducible oxides. On reducible oxides such as TiO_2 and in general on transition metal oxides the deposition of alkali metal atoms results in the reduction of Ti^{4+} to Ti^{3+} and formation of an adsorbed alkali metal cation.[6–11] On nonreducible oxides (e.g., MgO) the phenomena are more complex

[†]The results described in this Chapter have been reported in: *U. Martinez,* L. Giordano and G. Pacchioni, *The Journal of Chemical Physics* **128** 164707 (2008)

and ionization of the alkali metal atom is only possible in the presence of specific electron trapping sites.[12] In most cases the atom remains neutral, although strongly polarized.[13]

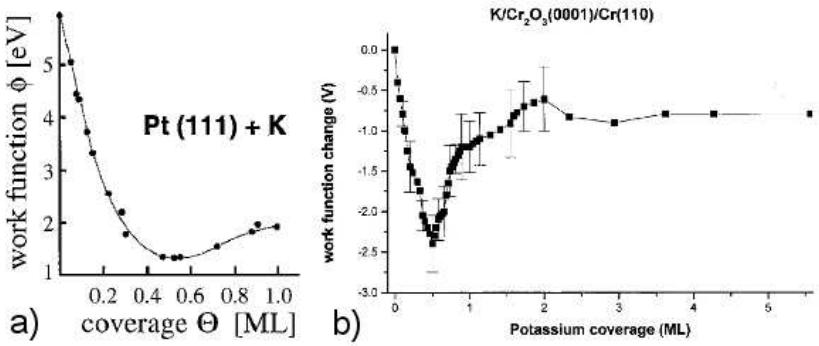

Figure 9.1: Work function change vs potassium coverage on Pt(111)[5] and on Cr_2O_3(1000)/Cr(110).[14]

Only few examples of alkali deposition on oxide thin films have been reported. The curve of $\Delta\Phi$ versus coverage for K on Cr_2O_3(0001)/Cr(110) is similar but not identical to the one found for alkali atoms on metal surfaces,[14] Figure 9.1b. To the best of our knowledge, no example has been reported of alkali metal deposition on thin films of nonreducible oxides, such as MgO or SiO_2. This is indeed the topic of this theoretical study.

Using a supercell plane wave density functional theory approach we have investigated the adsorption of Li, Na, and K atoms on three different, well characterized oxide thin films: SiO_2/Mo(112) (see previos part), MgO/Ag(100),[15,16] and TiO_2/Pt(111).[17] The first two cases are representative of nonreducible oxides; the third one is a typical transition metal oxide. We are particularly interested in the work function changes induced by the alkali metal adsorption and on the occurrence of charge transfers from the alkali atom to the support.

9.1 Computational Details

The calculations has been performed with the VASP code (see Sec. 2.1.1, pag. 25). The kinetic energy cutoff has been set to 400 eV. A vacuum of at least 10 Å separates the slabs and a dipole correction has been applied. The atoms within the supercell

are relaxed until the atomic forces are less than 0.01 eV/Å. The Mo(112), Ag(100), and Pt(111) metal substrates have been modeled by seven, four, and five metal layers, respectively. The SiO_2 film is built up by a network of six–membered Si–O rings; the fourth O atom located below each Si sits in a bridge position of the $[\bar{1}\bar{1}1]$ oriented rows of Mo(112) and anchors the film to the support (Section 1.3.3). For MgO a two–layer film has been deposited on the Ag(100) substrate; finally, the TiO_2 overlayer has a lepidocrocite structure matched to the size of the Pt(111) substrate.[17] Three alkali metal atoms have been considered, Li, Na, and K, characterized by different atomic sizes and ionization potentials. In particular, the ionic radii are 0.74 Å for Li^+, 1.02 Å for Na^+, and 1.38 Å for K^+.[18]

The work function of metal and metal/oxide surfaces has been defined as the energy of the vacuum level (determined as the self–consistent potential in the vacuum) with respect to the Fermi level of the metal or of the metal/oxide interface. The analysis of the work function change has been done for various coverages of alkali metals. Here the coverage is defined as the number of alkali atoms per surface metal cation (Si, Mg, or Ti) in the unit cell.

9.2 Results and Discussion

9.2.1 Alkali atoms on SiO_2/Mo(112)

The first system considered is K adsorbed on SiO_2/Mo(112). The atom has been placed above the center of a six–membered ring and the position fully optimized. In the minimum, K remains in the center of the ring (Figure 9.2) more or less equidistant from the O atoms of the silica network, 5.09 Å above the Mo surface layer; it is bound by 2.06 eV with respect to a gas–phase neutral K atom. A second minimum is found when K is placed directly on top of a bridging oxygen atom; in this case the bonding is weaker, 1.32 eV, and the K–O distance shorter, 2.56 Å (Table 9.1), typical of K^+ complexes. The existence of different minima separated by relatively large energies indicates that the potential energy surface is rather corrugated and that the diffusion barriers must be relatively high, of the order of more than 0.8 eV.

The position of the K atom is reminiscent of that assumed by alkali ions in the cavities of zeolite networks like the sodalite six–membered rings. The occurrence of a charge transfer and the formation of an adsorbed cation is confirmed by the analysis of the projected density of states (PDOS), Figure 9.3a, which clearly shows that the 4s level of K is empty, well above the Fermi level. A full electron has been

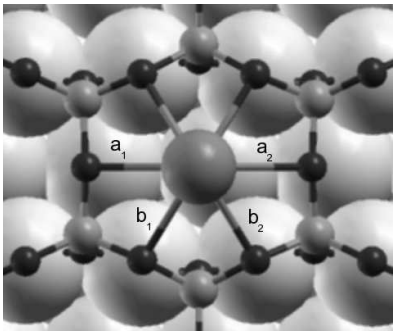

Figure 9.2: Top view of Li, Na, and K atoms adsorbed on SiO_2/Mo(112) films. (Selected distances) Li: $a_1 = 2.06$ Å, $b_1 = 2.15$ Å, $a_2 = 3.53$ Å, and $b_2 = 3.15$ Å; Na: $a_1 = 2.80$ Å, $b_1 = 2.59$ Å, $a_2 = 2.84$ Å, and $b_2 = 2.59$ Å; and K: $a_1 = 3.06$ Å, $b_1 = 2.83$ Å, $a_2 = 3.07$ Å, and $b_2 = 2.83$ Å. (Black spheres) O atoms, (small gray spheres) Si atoms, (large gray sphere) alkali atom, and (large white spheres) Mo atoms.

donated to the substrate, but the absence of new states in the gap of the SiO_2 film suggests that this is transferred to the Mo metal.

Adsorption above the surface layer is not the only possibility. If the atom is sufficiently small with respect to the ring size [as for the case of Pd and Ag (see Chapters 6 and 5)] it can penetrate into the ring and bind at the SiO_2/Mo interface. Indeed, K^+ penetrates with a barrier of 0.84 eV below the silica layer (Figure 9.4) and binds at the interface between SiO_2 and Mo(112) by 1.40 eV, i.e., less strongly than on the surface (Table 9.1). This is opposite to the behavior of neutral Pd atoms which bind much more strongly at the interface. It is likely that the atomic size plays a role and that the smaller binding of K in the cavity formed by the Mo(112) surface and the SiO_2 film is due to steric effects.

To check this we have considered Na, which has an ionic radius about 30% smaller than K. First of all, also for Na there is clear evidence of the formation of an adsorbed cation, with the Na 3*s* level unoccupied and a full electron transferred to the substrate. Na^+ binds in the same position of K, at the center of the ring, but with shorter Na–O distances of 2.59 and 2.80 Å (Figure 9.2) due to the fact that the atom is now closer to the ring, 4.46 Å above the Mo surface. The adsorption energy of Na in this position, 1.80 eV, is still slightly larger than at the interface, 1.66 eV (Table 9.1), but now the two values are similar, while for K there is a marked preference for adsorption above the surface. We did not investigate in detail the barrier

Table 9.1: Adsorption energy E_a, shortest M–O distance d(M–O), work function Φ, and work function change $\Delta\Phi$ for Li, Na, and K atoms adsorbed on SiO_2/Mo(112) and for K adsorbed on MgO(2L)/Ag(100) and TiO_2/Pt(111).

	Site	E_a (eV)	z(M)[d] (Å)	d(M–O) (Å)	Φ (eV)	$\Delta\Phi$ (eV)
Li/SiO_2/Mo(112)[a]	Surface	2.11	4.34	2.06	3.40	−1.47
	Interface	2.42	1.57	–	4.52	−0.35
Na/SiO_2/Mo(112)[a]	Surface	1.80	4.46	2.59	3.21	−1.66
	Interface	1.66	2.05	–	4.37	−0.50
K/SiO_2/Mo(112)[a]	Surf., ring center	2.06	5.09	2.83	2.57	−2.30
	Surf., on top O	1.32	6.07	2.56	1.56	−3.31
	Interface	1.40	2.46	–	4.27	−0.60
K/MgO/Ag(100)[b]	On top O	0.43		2.56	1.68	−1.24
	On top Mg	0.30		–	1.12	−1.80
K/TiO_2	On top O	1.51		2.42	–	–
K/TiO_2/Pt(111)[c]	On top O	1.52		2.41	1.61	−4.05

[a] M/SiO_2/Mo(112): θ=0.125 and $\Phi_{SiO_2/Mo(112)}$=4.87 eV.
[b] K/MgO/Ag(100): θ=0.111 and $\Phi_{MgO/Ag(100)}$=2.92 eV.
[c] K/TiO_2/Pt(111): θ=0.25 and $\Phi_{TiO_2/Pt(111)}$=5.66 eV.
[d] Height of the alkali atom from the Mo layer.

for penetration, but this should be similar, probably smaller, than for K.

The last case considered is that of Li. Also in this case the deposition of Li atoms results in the formation of Li^+ cations but here the different size results also in a different bonding mode. In fact, the Li^+ ion interacts with two oxygen atoms of the silica ring (Figure 9.2), forming a stable complex bound by 2.11 eV which is 4.34 Å above the Mo top layer (Table 9.1). The silica ring is significantly distorted by the interaction with the Li adsorbate and the shortest Li–O distances are of 2.06–2.15 Å (Figure 9.2). The second minimum, below the silica layer, is actually the global minimum with a binding energy of 2.42 eV. In this case the diffusion barrier is rather small, 0.30 eV. Therefore, once deposited on the silica film, the Li atoms are expected to diffuse spontaneously to the interface even at relatively low temperature, and there to form a stable complex. This prediction has been found to be correct and the

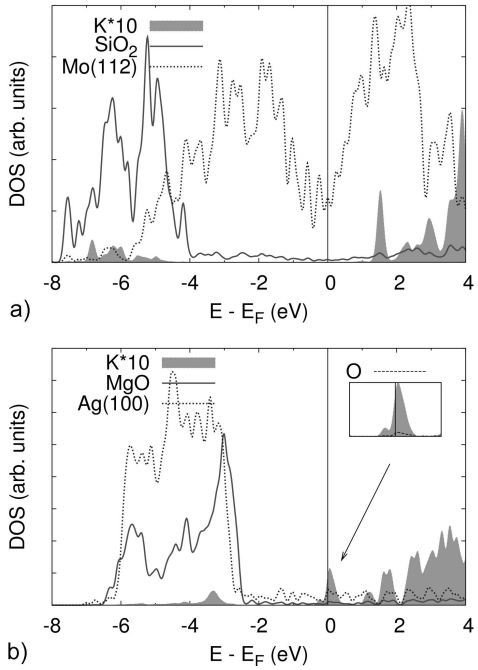

Figure 9.3: Projected density of states: (a) $K/SiO_2/Mo(112)$ (θ=0.125) and (b) K/MgO(2L)/Ag(100) (O top adsorption) (θ=0.111). The zero of energy corresponds to the position of the Fermi level E_F.

case of Li is described in more detail in the next chapter.

The different stability of alkali atoms adsorbed on the surface or at the interface of $SiO_2/Mo(112)$ is quite relevant for two reasons: first of all, the change in work function is not the same for the two adsorption sites (see below), and second we expect high diffusion barriers for the alkali atoms trapped at the Mo–SiO_2 interface.

No matter which is the preferred adsorption site, above or below the silica layer, the effect on the work function is pronounced (Table 9.1). For a coverage θ=0.125, corresponding to one alkali atom every eight Si atoms, the work function change induced by K is of -2.30 eV for adsorption above the surface, and of -0.60 eV for adsorption at the interface. As a result, Φ goes from 4.87 eV in $SiO_2/Mo(112)$ to 2.57 eV in $K/SiO_2/Mo(112)$ (K above the silica ring). Notice that for the less stable site where K is adsorbed on top of a bridging oxygen the longer distance from the Mo plane also leads to the strongest change in Φ, $\Delta\Phi$=-3.31 eV (Table 9.1). Clearly,

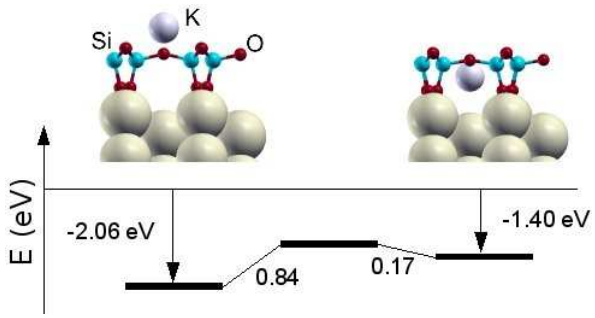

Figure 9.4: Energy profile for a K atom adsorbed above the surface (left) and at the interface (right) of a SiO_2/Mo(112) film. In the subsurface mimimum, K is 2.46 Å above the Mo surface. Na and Li bind in similar positions, with distances from the Mo surface of 2.05 and 1.57 Å, respectively.

$\Delta\Phi$ correlates with the height of the alkali atom from the metal layer. This is confirmed by the analysis of the results for Na and Li. The two ions are smaller, their distance from the metal surface is shorter than for K^+ when the same adsorption site is considered, leading to a smaller dipole. $\Delta\Phi$ for adsorption above the surface is therefore -1.66 eV for Na^+ and -1.47 eV for Li^+. This trend, i.e., a smaller $\Delta\Phi$ for the lighter alkali atoms, is also found for the bond at the interface, below the silica layer: $\Delta\Phi$ goes from -0.35 eV for Li (z=1.57 Å) to -0.50 eV for Na (z=2.05 Å) and -0.60 eV for K (z=2.46 Å). At the same adsorption site, and for the same coverage, $\Delta\Phi$ induced by a K atom adsorbed on Mo(112) is -1.35 eV, i.e., about twice as large. In fact, at the interface $\Delta\Phi$ is reduced by another effect: the alkali ion is in direct contact with both the metal and the oxide film and the ionic charge is partially screened. The correlation between $\Delta\Phi$ and z(M^+) is linear, but the slope is different for alkali metals adsorbed above or below the silica layer (Figure 9.5).

Not surprisingly, the effect of alkali metal adsorption on the work function is coverage dependent. On metal substrates, the $\Delta\Phi(\theta)$ curve has an almost universal behavior,[1,19] with a rapid decrease for low θ, a minimum in $\Delta\Phi(\theta)$ at a critical coverage, while at higher coverages $\Delta\Phi$ reaches the characteristic value of a full overlayer. The change in work function can be related to the charge transferred between the alkali adatom and the surface as:[20]

$$\Delta\Phi(\theta) = -N\Delta\mu \tag{9.1}$$

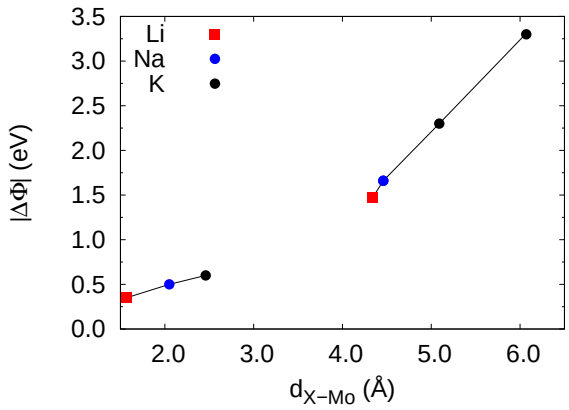

Figure 9.5: Work function change for Li, Na and K atoms adsorbed above or below the SiO_2/Mo(112) film as a function of the alkali–Mo distance.

where N is the number of adsorbates per unit area and $\Delta\mu$ is the change in the dipole moment per adsorbate. We have considered the change in Φ for K/ SiO_2/ Mo(112) (K above the surface and at the interface) for θ going from 0.083 to 0.5 (Figure 9.6); for comparison, we also considered K on the Mo(112) metal surface. K was placed in the position assumed at the SiO_2/Mo(112) interface and reoptimized. The $\Delta\Phi(\theta)$ curve for K above the silica layer shows the typical behavior described above, with a rapid initial decrease of Φ ($\Delta\Phi$ goes from -1.5 to -3.5 eV for $0.08 \leq \theta \leq 0.2$), due to the increasing number of adsorbed cations and a minimum around θ=0.25. This corresponds to $\approx 2\times10^{14}$ K atoms/cm^2. For higher coverages, the increase in N is compensated by a reduction in $\Delta\mu$ due to the increase of Coulomb repulsion between ionic adsorbates and a consequent reduction of the charge transfer. For θ=0.33 $\Delta\Phi$ becomes about -2.5 eV, a value which remains nearly constant even for larger coverages, up to θ=0.5. When K is at the interface, we notice the reduction of $\Delta\Phi$ previously described (see Table 9.1) and also a shift in the position of the minimum towards higher coverages, of $\approx 4\times10^{14}$ K atoms/cm^2. Also when K is adsorbed on Mo(112) the minimum of the $\Delta\Phi(\theta)$ curve is shifted to higher densities of adsorbates and, for a fixed coverage, the change in $\Delta\Phi$ is about one half of that induced by K above the silica surface. (Notice that here the coverage for K/Mo(112) is defined differently than in other studies of alkali ions on metals, see Ref.[1]; however, the minimum in the $\Delta\Phi(\theta)$ curve (Figure 9.6) corresponds to the same density of alkali atoms as for other systems like Na/Ni(100), i.e., $\approx 4\times10^{14}$ K atoms/cm^2.)

The smaller $\Delta\Phi$ is due to the fact that on the oxide film the alkali metal ions are more distant from the metal layer and the surface dipole is larger. The fact that the minimum of the curve occurs for higher densities of deposited alkali atoms is related to the different screening of the positive charge in the three systems. When K sits above the silica layer the net ionic charge is large since the rather unpolarizable oxide layer provides little screening; the screening is higher when K is directly in contact with the polarizable metal electrons, as in K/Mo(112), and largest when it is "encapsulated" into the cage formed by the metal layer below, the silica layer above, and the six interface O atoms around (see Figure 9.4). At the interface, in fact, the isolated charges are screened so efficiently that no minimum is found (Figure 9.6). Notice that for the highest possible coverage at the interface, one K ion per silica cage, i.e., θ=0.5, $\Delta\Phi$ is still smaller than for K above the film at the same coverage.

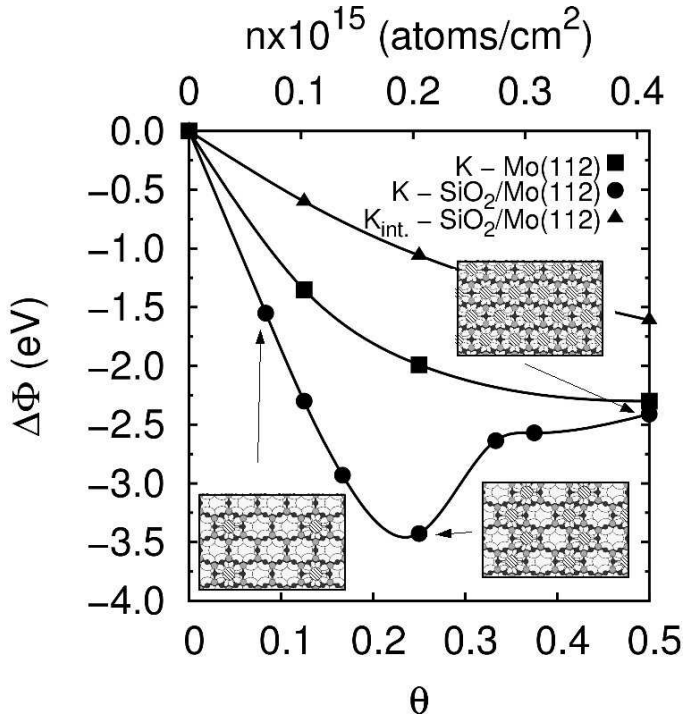

Figure 9.6: Work function change in K/Mo(112) and K/SiO_2/Mo(112) (K above the surface and at the interface) as a function of the K coverage.

These results show that the adsorption of alkali atoms on SiO_2/Mo(112) films

leads to a charge transfer from the adsorbate to the metal, hence to the formation of a dipole layer which lowers considerably the work function of the system. This is an important result since a smaller work function could result in modified properties of supported metal clusters, gold in particular, and eventually lead to a flow of charge from the metal/oxide substrate to the supported particle (see Chapter 11 pag. 165).

9.2.2 K on MgO/Ag(100)

We now move to the adsorption of K on MgO/Ag(100) films. This system has been discussed already[21] and here we expand the analysis to the case where a Ag atom is coadsorbed with K. On the terrace sites of bulk MgO, K adsorbs on top of O with a weak binding energy of 0.15 eV and a long surface distance, 2.89 Å.[13] The barrier for diffusion on the surface is so small that even at low temperature the K atoms are free to diffuse and become stabilized at more strongly binding sites like morphological defects. There is ample evidence that on polycrystalline MgO, K atoms bind to reverse corners.[13] What is important in this context is that alkali atoms deposited on MgO are not ionized. Upon adsorption the outer ns electron cloud is strongly polarized due to the interaction with the solid surface, but the spin density on the alkali atom is nearly 1. A similar effect has been recently observed experimetally for Li atoms adsorbed on the (100) surface of a thick MgO film.[22]

When K is adsorbed on a two–layer MgO/Ag(100) film there is a deep change in the adsorption properties.[21] The bonding on top of O, 0.43 eV, is a bit stronger than on MgO(100) and the K–O distance shrinks to 2.56 Å, typical for O–K^+ complexes[21] (Table 9.1). The adsorption is accompanied by a non–negligible surface relaxation: the O anion moves outwards by 0.4 Å and the Mg cation below it moves down by 0.3 Å. The K spin density is only 0.26, indicating the formation of a $K^{\delta+}$ species. This is consistent with the PDOS curves which show that the Fermi level crosses the K $4s$ level (Figure 9.3b) indicating the occurrence of an almost complete charge transfer from K to the MgO/Ag(100) substrate. Notice that the situation is slightly different from the SiO_2/Mo(112) case where the position of the empty $4s$ level is much higher in energy (complete charge transfer, Figure 9.3a). As a consequence of the formation of an adsorbed cation, a shift of the MgO/Ag(100) work function is expected and in fact the calculations show that Φ for K/MgO/Ag(100) is 1.68 eV (on top of O adsorption), i.e., 1.24 eV smaller than on the clean film. A slightly smaller shift is found when K is adsorbed on a Mg cation, where the bonding is weaker (Table 9.1). The work function change is fully consistent with the presence of $K^{\delta+}$ adsorbates on

the surface and with the prediction of Gurney's model.

The reduction of the work function induced by the adsorbed K ion can be used in principle to modify the properties of other adsorbates. Au atoms deposited on MgO/Ag(100) films spontaneously transform into Au^- anions, Chapter 3, while Ag atoms remain neutral.[23,24] The main reason is the different electron affinity of Ag (1.3 eV) and Au (2.3 eV). This means that while for Au_1/MgO/Ag(100) the Au $6s$ level falls below the Fermi level and becomes doubly occupied, on Ag_1 on MgO/Ag(100) the Ag $5s$ level remains at the Fermi level and is singly occupied. Thus, no charge transfer takes place.

We have considered the adsorption properties of Ag atoms on MgO/Ag(100) in the presence of coadsorbed K ions. The calculations have been done using a 4×4 supercell in order to minimize the adsorbate–adsorbate interaction; both atoms, K and Ag, have been adsorbed on top of oxide anions, and their distance is of about 8 Å (Figure 9.7). In the minimum structure the system exhibits a closed shell configuration, a sign that a profound change has occurred in the valence configuration of the two adatoms. The PDOS curves (Figure 9.7) clearly show that K $4s$ level is well above the Fermi level, and that a K^+ ion has formed, while the Ag $5s$ level is now below the Fermi level, with both α and β components occupied. Formally, the Ag atom has transformed into a Ag^- anionic species. This behavior, which differs substantially from that of isolated Ag adatoms on the same support, is due to two contributions, (1) the change in Φ induced by the coadsorbed alkali atom and (2) the cooperative effect of forming a layer of K^+ and Ag^- ionic species. The formation of the charged adatoms results in substantial polaronic distortions of the MgO layer (Figure 9.7): at the K adsorption site the O atom relaxes outward by 0.41 Å (d_{K-O}=2.49 Å); at the Ag adsorption site the O atoms relaxes inward by 0.15 (d_{Ag-O}=2.93 Å). These relaxations are fully consistent with the formation of a K^+–Ag^- pair. This shows that in principle it is possible to induce charge transfers which do not occur for the isolated species by coadsorption of alkali atoms. However, the thermal stability of this system is probably low as the Ag atoms can easily diffuse on the surface and form larger aggregates or bimetallic K/Ag clusters. Thus, if one wants to exploit this procedure to modify the surface properties, it is important to stabilize the adsorbed species by using the presence of defects or more strongly binding sites, like for instance the interface sites described above for the SiO_2/Mo(112) films (see next Chapter).

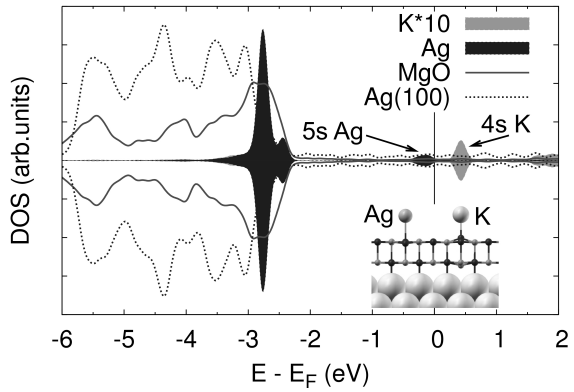

Figure 9.7: PDOS of $K_1/Ag_1/MgO/Ag(100)$. (Inset) A side view of K and Ag adatoms coadsorbed on MgO/Ag(100) films. The zero of energy corresponds to the position of the Fermi level E_F.

9.2.3 K on TiO_2/Pt(111)

The last case considered is that of K adsorption on a TiO_2 film formed on Pt(111). Experimental low–energy diffraction (LEED), scanning tunneling microscopy (STM), and photoemission data combined with first principles DFT calculations have shown that a rectangular titania nanophase grown on Pt(111) has the structure of a layer of lepidocrocite.[17] The oxide film interacts only very weakly with the metal single crystal surface, and the resulting Pt–titania interface distance is rather long. This is the reason why virtually no change in the work function of Pt(111) is observed upon deposition of the thin oxide film.

Adsorption of alkali atoms on titania is known to reduce the oxide.[6–11] This is shown by the formation of Ti^{3+} species with one unpaired electron localized in the $3d$ shell of the transition metal ion; the corresponding states are at about 0.8–1 eV below the conduction band. This is what occurs if we adsorb K on top of an oxygen atom of the unsupported lepidocrocite film (Figure 9.8); here the K coverage is 0.25. K is bound to the oxide by 1.5 eV (Table 9.1). The occurrence of a net charge transfer in K/TiO_2 is also consistent with the short K–O distance (Table 9.1). A spin density plot clearly shows the absence of spin density around K, which is now K^+; the spin is accumulated around the Ti ions and is delocalized because of the known tendency of pure DFT to give too low band gaps and delocalized electronic states.[25] The inclusion of self–interaction correction terms, e.g., by using hybrid functionals,[26] via

the DFT+U approach,[27] or the GW approximation,[28] results in a correct description of a localized electron on a single Ti ion. This limitation, however, is not important in the context of this work, i.e., for the study of the work function changes.

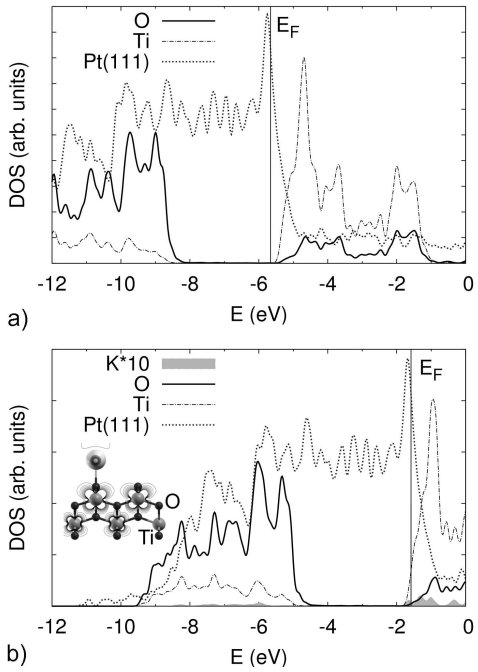

Figure 9.8: Projected density of states: (a) TiO_2/Pt(111) and (b) K/TiO_2/Pt(111) (θ=0.25) (O top adsorption). (Inset) spin density plot for K/TiO_2, lateral view. The zero of energy corresponds to the position of the vacuum level.

The situation is very similar when K is adsorbed on a TiO_2/Pt(111) film. Spin distribution, K binding energy, and K–O distance are virtually identical to those found for the unsupported layer, (Table 9.1). The analysis of the PDOS curves (Figure 9.8) shows that upon K deposition there is a Ti 3d state which is just below the Fermi energy and which corresponds to the formation of Ti^{3+} ions; as we mentioned before, this state is too close to the conduction band due to inherent limitations in the DFT treatment.[26] Therefore, contrary to the SiO_2/Mo(112) and MgO/Ag(100) cases, here the K 4s electron is transferred to the oxide, not to the metal support. The similarity of the electronic structures in K/TiO_2 and K/TiO_2/Pt(111) confirms the weak coupling of the Pt and titania wave functions. Despite the absence of direct

interaction, the charge transfer between K and TiO_2 has dramatic consequences on the work function of the TiO_2/Pt(111) system (Table 9.1 and Figure 9.8). Φ of pure Pt(111), 5.86 eV, is reduced by 0.2 eV only in TiO_2/Pt(111) (Table 9.1); the addition of K and the formation of a strong surface dipole in the oxide layer lowers Φ by more than 4 eV, so that Φ[K/TiO_2/Pt(111)] is now 1.6 eV (Table 9.1 and Figure 9.8). This is a very large change which has a purely electrostatic origin. In fact, if we move the K/TiO_2 film up and down with respect to the Pt(111) plane, Φ changes only very slightly. The reason is that an electron emitted from the metal surface has to pass through the dipole layer which lowers the cost of the extraction, in complete agreement with the classical Langmuir–Gurney model.[2,3] This effect is basically independent of the position of the dipole layer.

9.3 Summary

The results of DFT calculations have clearly shown the different behavior of nonreducible and reducible oxide thin films with respect to the deposition of low amounts of alkali metal atoms. In all cases the alkali atoms donate a full electron to the substrate. On SiO_2 and MgO thin films, where there are no trapping sites nor reducible cations, the electron is transferred to the metal substrate, with formation of an adsorbed alkali metal cation and a corresponding image charge into the metal support. On reducible oxide films, such as titania, the alkali atom donates one electron to the oxide, with consequent reduction of the Ti ions from Ti^{4+} to Ti^{3+}, not to the metal. In both cases, reducible or nonreducible oxides, the charge transfer creates a dipole moment which lowers the work function of the system. The effect is coverage dependent and is closely related to the adsorption position and to the height of the alkali metal atoms above the surface. This is clearly shown by two results. On SiO_2/Mo(112) two different adsorption modes can be identified, with the alkali atom adsorbed above the surface or bound to the interface. The two minima are separated by a barrier. While Li, which is small, prefers to adsorb at the interface, K, with a large ionic radius, prefers to bind above the silica layer. For Na the two sites are almost isoenergetic. The change in work function, $\Delta\Phi$, is always larger when the alkali atom sits above the silica film, at a longer distance from the metal layer, consistent with the fact that the resulting dipole is larger. When the alkali atom is adsorbed at the interface $\Delta\Phi$ is smaller because of the shorter distance from the metal and also because of a partial screening of the positive charge by the polar-

izable metal electrons. The role of the distance of the alkali atom from the surface is also well illustrated by the values of $\Delta\Phi$ as one goes from Li to Na and K for the same adsorption site: $\Delta\Phi$ is always largest for K and smallest for Li, consistent with their different ionic radii.

The change in work function induced by the adsorbed alkali metal atoms can be used in principle to modify the properties of the oxide films. In fact, the codeposition of metal atoms or clusters with high electron affinities and alkali metal atoms could result in a reverse charge transfer from the metal substrate to the supported cluster. This effect has been demonstrated here for the case of MgO/Ag(100). On this support Ag atoms remain neutral, at variance with the Au atoms which spontaneously transform into Au^- species (see Chapter 3). The adsorption of K has the effect to lower the work function, hence to move the Fermi level of the Ag(100) substrate to higher energies. When we codeposit Ag and K atoms on MgO/Ag(100) films, we observe the formation of Ag^- species and the occurrence of a charge transfer. This effect, however, can be difficult to reproduce experimentally because of the low thermal stability of these systems. The barriers for diffusion of Ag atoms on the oxide films are expected to be rather low, and aggregation and formation of KAg particles is possible. A way to prevent this is to directly adsorb the alkali atom at the interface. This could be done either by depositing the alkali metal atoms before to grow the oxide films or, as shown for the case of SiO_2/Mo(112) films, by spontaneous diffusion of the alkali atom into the pores of the structure. When this occurs, as for Li/SiO_2/Mo(112), one obtains a stable assembly of incorporated alkali metal cations. Unfortunately, the fact that the ion is completely surrounded by other metal or oxide atoms leads to a partial screening of the charge of the alkali cation and to a smaller change in work function. Nevertheless, deposition of alkali metal atoms can be a viable way to modify in a desired manner the electronic properties of ultrathin oxide films (see next Chapter).

Bibliography

[1] H. P. Bonzel, *Surf. Sci.* **8** (1987), p. 43.

[2] K. H. Kingdom and I. Langmuir, *Phys. Rev.* **21** (1923), p. 380.

[3] R. W. Gurney, *Phys. Rev.* **47** (1935), p. 479.

[4] A. Zangwill, *Physics at Surfaces* (Cambridge University Press, Cambridge, 1988).

[5] M. Kiskinova, G. Pirug, and H. P. Bonzel, *Surf. Sci.* **133** (1983), p. 321.

[6] K. Prabhakaran, D. Purdie, R. Casanova, C. A. Muryn, P. J. Hardman, P. L. Wincott, and G. Thornton, *Phys. Rev. B* **45** (1992), p. 6969.

[7] R. Heise and R. Courths, *Surf. Sci.* **331–333** (1995), p. 1460.

[8] A. W. Grant and C. T. Campbell, *Phys. Rev. B* **55** (1997), p. 1844.

[9] H. Onishi, T. Aruga, C. Egawa, and Y. Iwasawa, *Surf. Sci.* **199** (1988), p. 597.

[10] J. Nerlov, S. V. Christensen, S. Wichel, E. H. Pedersen, and P. J. Møller, *Surf. Sci.* **371** (1997), p. 321.

[11] T. Bredow, E. Aprà, M. Catti, and G. Pacchioni, *Surf. Sci.* **418** (1998), p. 150.

[12] S. Brazzelli, C. Di Valentin, G. Pacchioni, E. Giamello, and M. Chiesa, *J. Phys. Chem. B* **107** (2003), p. 8498.

[13] M. Chiesa, E. Giamello, C. Di Valentin, G. Pacchioni, Z. Sojka, and S. Van Doorsiaer, *J. Am. Chem. Soc.* **127** (2005), p. 16935.

[14] W. Zhao, G. Kerner, M. Asscher, X. M. Wilde, K. Al-Shamery, H. J. Freund, V. Staemmler, and M. Wiesbowska, *Phys. Rev. B* **62** (2000), p. 7527.

[15] S. Schintke and W.-D. Schneider, *J. Phys.: Condens. Matter* **16** (2004), p. R49.

[16] S. Schinkte, S. Messerli, M. Pivetta, F. Patthey, L. Libioulle, M. Stengel, A. De Vita, and W.–D. Schneider, *Phys. Rev. Lett.* **87** (2001), p. 276801.

[17] Y. Zhang, L. Giordano, G. Pacchioni, A. Vittadini, F. Sedona, P. Finetti, and G. Granozzi, *Surf. Sci.* **601** (2007), p. 3488.

[18] R. D. Shannon and C. T. Prewitt, *Acta Crystallogr., Sect. B: Struct. Crystallogr. Cryst. Chem.* **B25** (1969), p. 925.

[19] R. L. Gerlach and T. N. Rhodin, *Surf. Sci.* **19** (1970), p. 403.

[20] G. Pacchioni and P. S. Bagus, *Surf. Sci.* **286** (1993), p. 317.

[21] L. Giordano and G. Pacchioni, *Phys. Chem. Chem. Phys.* **8** (2006), p. 3335.

[22] J. C. Lian, E. Finazzi, C. Di Valentin, T. Risse, H.–J. Gao, G. Pacchioni, and H.–J. Freund, *Chem. hys. Lett.* **450** (2008), p. 308.

[23] G. Pacchioni, L. Giordano, and M. Baistrocchi, *Phys. Rev. Lett.* **94** (2005), p. 226104.

[24] L. Giordano, M. Baistrocchi, and G. Pacchioni, *Phys. Rev. B* **72** (2005), p. 115403.

[25] G. Pacchioni, F. Frigoli, D. Ricci, and J. A. Weil, *Phys. Rev. B* **63** (2001), p. 054102.

[26] C. Di Valentin, G. Pacchioni, and A. Selloni, *Phys. Rev. Lett.* **97** (2006), p. 166803.

[27] B. J. Morgan and G. W. Watson, *Surf. Sci.* **601** (2007), p. 21.

[28] S. Albrecht, L. Reining, R. Del Sole, and G. Onida, *Phys. Rev. Lett.* **80** (1998), p. 4510.

CHAPTER 10

Lithium incorporation into a silica thin film[†]

The main technological challenge in the use of alkali metals, for catalytic applications, is their protection from unwanted chemical reactions that would cause rapid degradation of their desired properties otherwise. For this purpose, the alkali species are usually embedded in a metal or oxide matrix, which inhibits contact to a reactive environment but also suppresses the intended effect on the work function. In the previous Chapter (Section 9.2.1 page 135), an elegant way has been proposed that combines the diverging requirements in the use of alkali metals. In this approach, the alkalis are placed at the interface between an ultrathin SiO_2 film and a Mo(112) crystal. In their interfacial binding position, the atoms are well–protected by the inert oxide layer above, but still close enough to the surface to lower the work function of the system. Furthermore, adsorption sites at the silica–Mo interface are accessible even after film preparation, as the porous nature of silica film enables the smaller alkali atoms, Li and Na, to diffuse through the top–layer.

In this Chapter, we provide more details on the Li interaction with the silica/Mo system, employing low–temperature scanning tunneling microscopy (STM) and density functional theory (DFT) as investigative tools. The spatial distribution of Li

[†]The results described in this Chapter have been reported in: J. Jerratsch, N. Nilius, H.-J. Freund, *U. Martinez*, L. Giordano, G. Pacchioni, H.-J. Freund, *Phys. Rev. B* Submitted

adsorbates at the metal–oxide interface is analyzed and explained in terms of the distinct screening response of the SiO_2/Mo(112) interface.

10.1 Computational and Experimental Details

Computational Details

The calculations has been performed with the VASP code (see section 2.1.1, page 25). The kinetic energy cutoff has been set to 400 eV. A vacuum of at least 10 Å separates the slabs and a dipole correction has been applied. The atoms within the supercell are relaxed until the atomic forces are less than 0.01 eV/Å. A (4×2) super cell with a composition of $Mo_{56}Si_8O_{20}$ is used to model the Li interaction with the oxide film. The cell can hold one to eight Li atoms, corresponding to 0.25 to 2 atoms per silica ring (throughout the Chapter, coverage refers to atoms per silica pore). In selected cases, also larger (6×4) cells are used to simulate the spatial distribution of the Li atoms and to generate STM images with the Tersoff–Hamann approach.[1] The work function of the metal/oxide system has been defined as the energy of the vacuum level, determined as the self–consistent potential in the vacuum with respect to the Fermi level of the metal.

Experimental Details

All measurements have been performed with a costume built, ultrahigh–vacuum STM operating at 10 K. Topographic and electronic sample information are obtained by constant–current imaging and differential conductance (dI/dV) spectroscopy using lock–in technique. The Li atoms are deposited from a commercial SAES getter onto the freshly prepared surface at 100 K.

10.2 Results and Discussion

10.2.1 Single Li adsorbate

Deposition of tiny Li amounts onto the silica film (below 0.05 atoms per silica pore) leads to the appearance of distinct adsorption structures in the STM. Two configurations can be distinguished, ring–like structures that coincide with the –Si–O– hexagons (Figure 10.1a) and X–shaped elements pointing in the Mo [110] direction

(Figure 10.1b). Larger ad–structures are always assembled from those elementary configurations, whereby particularly high imaging contrast is observed at assigned to a Li dimer, while five ring–like elements in neighboring –Si–O– hexagons cause the pattern in Figure 10.1c and d. Typical for all Li–induced ad–structures is that not the adatom itself but distinct building blocks of the silica film seem to be responsible for the topographic contrast. A similar behavior was observed after Pd and Ag deposition onto the oxide film and explained by the fact that the atoms occupy binding sites below the film at the metal–oxide interface (see Chapter 5). The distinct contrast in this case is triggered by a hybridization of the valence s–state of the adatom and the O $2p$ orbitals of the surface O atoms, which locally increases the unoccupied state density of the –Si–O– ring hosting the adsorbate. Similar adsorption patterns in the present experiment suggest that also Li is able to penetrate the top–most oxide layer and binds in interfacial sites as well.

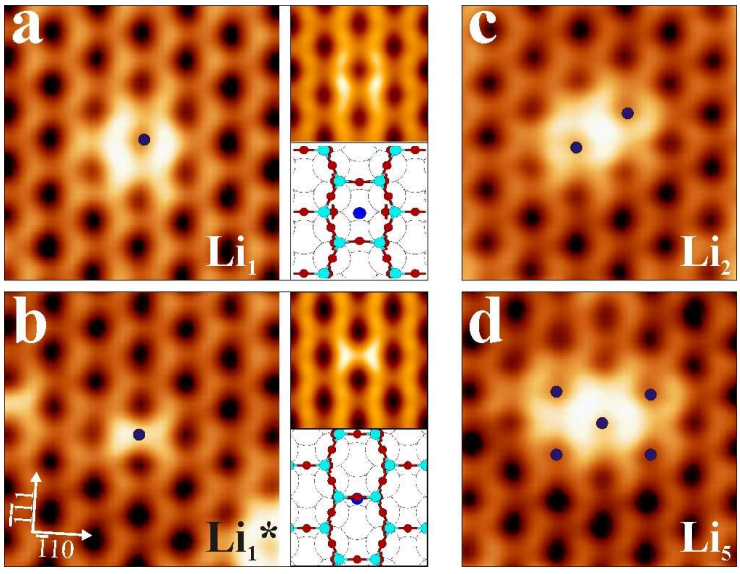

Figure 10.1: (a,b) Topographic (0.1 V, 3×3 nm^2) and simulated STM image (0.5 V, 1.8×1.6 nm^2) as well as structure model of a single Li atom bound to two different interface sites of silica/Mo(112). (c,d) STM images of two larger Li aggregates (0.1 V, 3×3 nm^2). The position of Li atoms at the interface is marked by dots.

Both, the ring– and X–shaped Li elements are only observed at small bias voltages, but transform into round protrusions at elevated positive sample bias (Fig-

ure 10.2). The contrast change of the Li features is accompanied by an increase of their apparent height by almost a factor of two. The threshold bias hereby depends on the geometric size of the ad–feature. Whereas an individual element turns bright at around +2.75 V, this value down–shifts to approximately +2.25 V for aggregates containing three or more elements (as the one shown in Figure 10.1d). The bias–dependent contrast of Li indicates the availability of new conductance channels for electron transport at higher positive bias. We will demonstrate below that those channels are related to the silica conduction band, which shifts to lower energy in vicinity of the Li atoms.

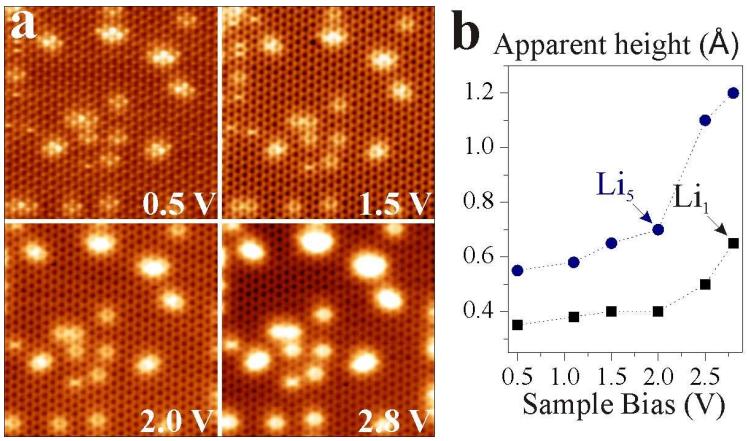

Figure 10.2: (a) Bias series of single Li atoms and small assemblies at the silica/Mo(112) interface (15×15 nm^2). (b) Evolution of the apparent Li height as a function of sample bias.

The adsorption behavior sketched above is corroborated by results of the DFT calculations on the Li–doped silica/Mo(112) film. Single Li atoms are able to penetrate the openings in the –Si–O– hexagons with a small activation barrier of 0.3 eV (Chapter 9). After passing the nano–hole, the Li adsorbs in two different hollow sites along the furrows of the Mo(112) surface (Figure 10.1a and c). In the site that is directly below a –Si–O– hexagon, the atom binds with 2.43 eV and donates almost a complete electron to the Mo support (Bader charge: $-0.88\ e$). The hence unfilled Li 2s orbital hybridizes with the Si 3s and O 2p contributions of the oxide conduction band, resulting in a local increase of the empty–state density in the silica ring above. This Li–induced enhancement of the oxide LDOS is now probed by tunneling electrons at positive bias and gives rise to the characteristic ring–like adsorp-

tion pattern (Figure 10.1a). Alternatively, the Li can occupy a Mo hollow site below [110]-oriented ring segments in the silica film. In this configuration, the Li mainly hybridizes with the Si–O–Si unit above, resulting in the X–shaped adsorption structure depicted in Figure 10.1b. The nearly identical Li binding energy (E_B=2.41 eV) with respect to the ring site explains the similar occupancy of both interfacial sites found in the STM measurements. Also below a Si–O–Si bridge, the Li donates its 2s electron to the Mo support and becomes cationic, as revealed by the Bader value of $-0.82\ e$. However, the smaller net charge and the shorter Li–metal distance (1.25 Å versus 1.57 Å) at this site result in a 20% reduction of the induced surface dipole with respect to the binding position below the silica ring.

For single Li atoms on silica/Mo(112), the adsorption characteristic derived from STM and DFT data is apparently in good agreement with the classical Langmuir–Gurney picture developed for metal supports.[2,3] The Li becomes cationic even in the interfacial binding sites, and preferentially occupies high–coordinated hollow sites along the Mo(112) furrows. The silica film above the Mo support seems to perturb this behavior only weakly. This situation will change however for higher Li loads as demonstrated in the next section.

10.2.2 High Li coverage

The deposition of higher Li quantities strongly perturbs the electronic structure of the silica film, as demonstrated by conductance spectroscopy and imaging with the STM (Figure 10.3). A first indication comes from the large bias–dependence of the contrast between Li–rich and Li–poor regions. Similar to the isolated Li species (Figure 10.2), Li–rich islands experience an apparent–height increase from 0.5 to 1.2 Å when ramping the voltage from $+0.5$ to $+2.5$ V. The same effect is visible in simulated STM images, indicating an electronic origin of the measured surface corrugation (Figure 10.5b). The fact that Li–rich stripes turn bright first indicates the local availability of new low–bias conductance channels in those regions. Conductance spectra taken on silica patches with different Li content provide direct evidence for this assumption (Figure 10.3a). The pristine film exhibits a smoothly increasing dI/dV curve, interrupted only by a small kink at $\sim$3.0 V that marks the onset of the silica conduction band. The kink arises because new states become suddenly available for tunneling into the empty silica states. Experimentally, the onset energy E_c is defined by the bias value, where either the slope of the dI/dV curve becomes maximal, or alternatively the dI/dV signal reaches 50% of the intensity above

the kink (see dashed lines in Figure 10.3a). The so estimated band onset amounts to 2.9 V for the pristine silica film. Together with a similar kink at −3.6 V in filled state spectra, this value adds up to a total gap size of 6.5 eV for the monolayer silica film. Not surprisingly, the gap is much smaller than in bulk SiO_2 (E_g ∼9 eV),[4] reflecting the reduced oxide thickness and the residual influence of the metal support.

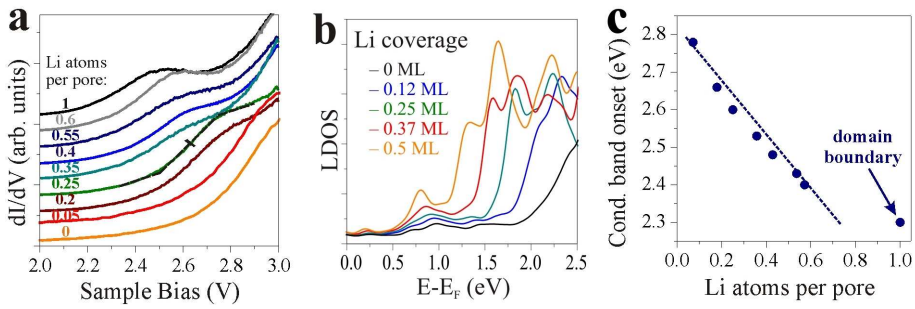

Figure 10.3: (a) Conductance spectra taken on silica/Mo(112) regions with different Li concentrations. The set–point for spectroscopy is adjusted to 2.9 V; all spectra are offset for clarity. (b) Calculated LDOS of silica/Mo(112) in the region of conduction band for various Li coverage. (c) Deduced conduction band onsets from (a) shown as a function of Li coverage.

With increasing Li coverage, this kink position experiences a gradual down–shift in energy, whereas the exponential growth of the dI/dV signal is recovered above the discontinuity (Figure 10.3a). Furthermore, the kink appears at lower absolute dI/dV intensities and considerably broadens with increasing Li load.[†] A more precise analysis suggests a monotonous down–shift of the silica conduction band from 2.9 to 2.4 eV as the coverage increases from zero to one Li atom per silica pore (Figure 10.3c). At Li–filled domain boundaries, the band onset moves down even further to approximately 2.3 V. A similar behavior is revealed for the calculated band onsets (Figure 10.3b). Absolute band positions as a function of the Li coverage slightly differs in experiment and theory due to the known deficiency of DFT to reproduce gap sizes of insulating materials.

[†]The spectral broadening reflects a certain averaging over oxide regions with different Li content.

10.2.3 Discussion – Topography of the Li ad–system

With increasing exposure, the characteristic ring– and X–shaped fingerprints of isolated Li adsorbates cannot be identified any more, because Li–induced features overlap to complex adsorption patterns on the surface. However, Li–rich and Li–poor areas remain distinguishable due to the increased topographic height of the former in STM images taken above 2.0 V (Figure 10.4).

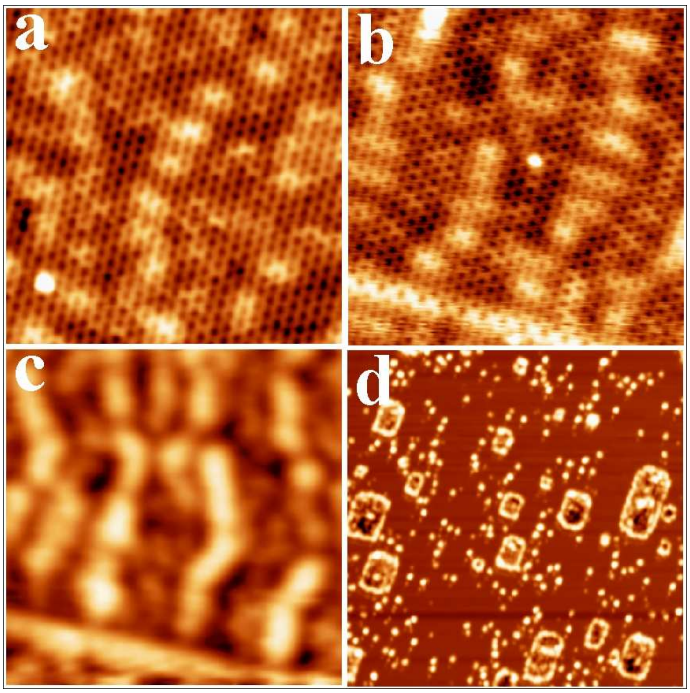

Figure 10.4: (a–c) STM topographic images of silica/Mo(112) taken for increasing Li exposures (15×15 nm^2). Bias voltages are 0.5 V in (a,b) and 2.5 V in (c). Atomic resolution is only obtained at low sample bias. The bright horizontal lines in (b,c) are Li–filled domain boundaries in the oxide film. (d) Sample surface after high Li exposure, when Li saturates the interface binding sites and forms small particles on top of the oxide film (3.5 V, 150×150 nm^2).

The formation of compact and long–range ordered Li islands at the interface between the silica film and Mo(112) is in sharp contrast to the usual adsorption behavior of alkalis on bare metal surfaces. There, the alkali ions often adopt open configurations in order to maximize their mutual distance and to reduce the Coulomb

repulsion.[5,6] For example, the development of (4×1) and (2×1) superstructures has been observed by LEED for the Li/Mo(112) system without oxide top layer.[7] On silica/Mo(112), on the other hand, Li assemblies already form at relatively low exposure, although the charged nature of the adsorbate is clearly demonstrated by the DFT calculations. The difference to bare metal surfaces can be traced back to the structural and electronic peculiarities of the dielectric oxide film that, in conjunction with the Mo crystal below, enables effective screening of the Li–Li interactions. The screening efficiency is manifested by the weak coverage–dependence of the Li binding energy derived from the DFT (Figure 10.5a). An increase of the nominal Li coverage from zero to one Li^+ per pore results in a weakening of the binding strength by marginal 3%. Only when a second Li is inserted into a nano–pore, the binding energy declines more steeply due to the increasing Coulomb repulsion between the ions. This finding is in good agreement with the STM results, which indicate that only one Li atom can penetrate a silica pore at the chosen experimental conditions. As incorporation of more Li is still favorable from a thermodynamic point of view, the saturation coverage seems to be related to a kinetic hindrance. Not surprisingly, the evolution of the Li binding energy on the bare Mo(112) surface[8] differs only moderately from the oxide–covered case, demonstrating the dominant screening contribution of the metal support.

The small initial coverage dependence of the Li binding energy is compatible with the observed formation of Li islands at the metal–oxide interface. The effect has been quantified by comparing the stability of three different Li configurations with θ=0.25 via DFT, namely of isolated Li ions with 10 Å separation, Li trimers occupying adjacent silica pores and Li rows along the Mo$[\bar{1}\bar{1}1]$–direction (Figure 10.5b). Hereby, the trimer configuration turns out to be lowest in energy, whereas the isolated Li ions and the row pattern are less stable by 0.08 eV and 0.21 eV, respectively. Although the energy differences are too small to conclude the thermodynamically preferred Li distribution at the interface, the results demonstrate the effective Li–Li screening on the length scale of one silica pore.

Although the formation of Li islands at the metal–oxide interface is not in contradiction with thermodynamics, the driving force for the assembly effect still needs to be analyzed. To shed light into this question, not only the interfacial binding energies but also the Li penetration process trough the silica top layer has to be considered. Island formation could be explained for example, when the Li penetration barrier would be lowered in the presence of pre–adsorbed Li^+ at the interface. Exactly this behavior is revealed by the DFT calculations. The initial penetration

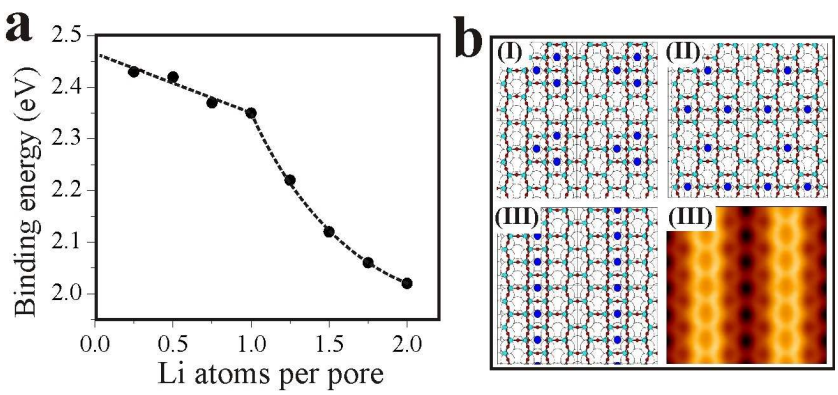

Figure 10.5: (a) Average binding energy of interfacial Li as a function of coverage. (b) Ball model for different Li configurations with identical coverage of 0.25 atoms per pore. The corresponding binding energies, computed with an enlarged (6×4) super cell, are depicted with bars in (a). The simulated STM image for configuration (III) (+2.0 V, 3.3×3.3 nm^2) demonstrates that Li–rich areas are indeed imaged with enhanced apparent height (0.5 Å), although the geometric corrugation is below 0.1 Å (lower right panel).

barrier for Li amounts to ∼0.3 eV, but decreases when neighboring adsorption sites are already occupied with an alkali species. In the limiting case of one Li atom penetrating an empty pore with six filled neighbors, the energy barrier drops to tiny 0.11 eV. This is related to small lattice distortions which favor Li penetration in the presence of other Li atoms at the interface This finding clearly indicates easier Li penetration in vicinity of pre–adsorbed ions and helps rationalizing the observed island formation at the interface.

It should be noted that the self–assembly of interfacial Li ions into $[\bar{1}\bar{1}1]$–oriented stripes is supported by the strong anisotropy in the Mo(112) diffusion barriers. While along the $[\bar{1}\bar{1}1]$–oriented Mo furrows, the Li diffusion is activated by only 0.09 eV, this value reaches 0.75 eV in the perpendicular direction.[9] In presence of the silica film, the diffusion barrier along the furrows both values increases by roughly a factor of three (0.27 eV). Nonetheless, transient Li diffusion remains possible along the furrows due to the thermal energy of the incoming atoms (800 K when leaving the SAES getter), while any movement between the furrows is strictly forbidden. After thermalization of the Li, the spatial distribution at the interface will be stabilized by the low temperatures of the experiment.

10.2.4 Discussion – Electronic properties

The most apparent consequence of the Li incorporation into silica/Mo(112) is the gradual redshift of silica band onsets with increasing Li load (Figure 10.3). This behavior is in perfect agreement with a work function reduction induced by cationic Li^+ ions, as predicted by the Langmuir–Gurney model.[2] The positive surface dipole formed between the interfacial Li^+ and their image charge in the metal results in a lowering of the vacuum energy of the system. As the oxide electronic states are mainly adjusted to the vacuum level, the band positions experience a similar downshift with increasing Li load. The reason for the direct proportionality between the work function and the band positions is the large gap value of silica, which prevents any charge transfer into the oxide film and hence a pinning of the energy levels. The Li coverage dependence of both, the work function and the silica band onsets, has been calculated by DFT and is depicted in Figure 10.6. For low Li concentrations, the work function decrease almost linearly with coverage according to $\delta\Phi/\delta\theta$=−1.3 eV/pore (θ=1 equals to one Li per pore). The slope gradually decreases for higher coverage, but remains positive even for θ >2 ($\delta\Phi/\delta\theta$=−0.65 eV/pore). The onset of the silica conduction band closely follows this work function decline as a function of θ, as also shown in Figure 10.6. Both observations suggest that the charge transfer out of the Li does not saturate even at the maximum coverage explored in this study and the alkali atoms remain cationic at the silica–Mo interface. In contrast, the universal work–function versus coverage curve is restored on the bare Mo(112) upon Li adsorption (Figure 10.6). Similar to the silica/Mo system, experiences an initial decline, but runs through a minimum at θ∼1 and increases again towards the bulk value of lithium at higher coverage. This difference reflects the role of the oxide film and in particular of the interfacial O atoms, which act as an additional sink for the Li 2s electrons and further screen the Li charge at the interface. Not surprisingly, the universal coverage dependence of Φ including the minimum reappears when the alkali atoms bind on–top of the silica film and not at the interface, as revealed for the much larger K atoms.[10]

Even for Li saturation coverage of two atoms per silica ring, the work function of the system is higher than the tabulated Li–bulk value of 2.9 eV[11] (which corresponds to $\delta\Phi$=−2.0 eV in Figure 10.6) and the Li is still cationic. Apparently, metallization of the alkali layer is prevented in this case by the limited number of atoms that fit into the interface region. Lithium bulk values for the work function are only expected, when all interface sites are saturated and Li starts nucleating above the

oxide surface. Such cluster formation is indeed experimentally observed at high Li exposure (Figure 10.4d), however the resulting work function is not accessible via tunneling spectroscopy anymore, because the influence of Li clusters on the silica band structure vanishes.

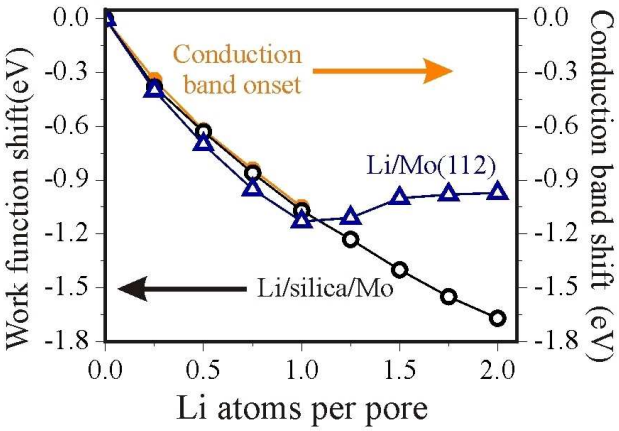

Figure 10.6: Change of the conduction band onset and the work function of SiO_2/Mo(112) and Mo(112) calculated as a function of Li coverage.

It should be noted that experimental shifts of the silica conduction band are roughly 50% smaller than the calculated values (see Figure 10.3). This discrepancy might be explained by two effects: (i) During spectroscopy, the tip induces a counter–field that reverses the Li–induced band shift and (ii) the interfacial Li coverage is strongly inhomogeneous and each measurement is subject to a certain averaging between Li–rich and Li–poor regions.

10.3 Summary

The adsorption behavior of Li on a silica thin film grown on Mo(112) has been characterized by low–temperature STM and DFT calculations. Due to the porous structure of the silica, Li atoms are able to penetrate the oxide layer and bind in two distinct configurations at the metal–oxide interface. Substrate–mediated interactions between the Li ions give rise to their self–assembly into elongated Li stripes at higher alkali exposure. Upon adsorption, the Li becomes cationic and forms a pos-

itive surface dipole, which in turn reduces the work function of the silica/Mo(112) film. The work function decrease has been deduced from the downshift of the silica conduction band, and reaches $\sim$0.5 eV (theoretical value 1.0 eV) when each silica pore hosts one Li ion.

The successful modification of the silica electronic structure by Li doping, in particular the tuning of its work function, opens various interesting applications. In contrast to the pristine film, Li–doped silica is attractive for the adsorption of electronegative species, as the reduced work function will promote charge transfer processes out of the film. By this means, anionic species might be stabilized on the oxide surface (see in particulat the next Chapter), being a promising starting point to fabricate systems with enhanced chemical activity. With respect to other techniques, the modification of the oxide properties is based on a "passive" approach, as the Li ions are neither directly involved nor consumed in the adsorption process. In principle, the tuning of electronic and chemical properties of oxide films via alkali doping is of universal character and can be applied to other systems as well. Although Li insertion into silica/Mo(112) is particularly easy due to the porous nature of the film, the technique can be extended to compact oxide materials, where the alkali atoms have to be introduced prior to film growth.

Bibliography

[1] J. Tersoff, D. R. Hamann, *Phys. Rev. Lett.* **50** (1983), p. 1998.

[2] I. Langmuir, K. H. Kingdon, *Science* **57** (1923), p. 58; I. Langmuir, *J. Am. Chem. Soc.* **54** (1932), p. 2798.

[3] R. W. Gurney, *Phys. Rev. Lett.* **47** (1935), p. 479.

[4] N. F. Mott, *J. Non–Cryst. Solids* **40** (1980), p. 1.

[5] J. Kliewer, R. Berndt, *Surf. Sci.* **477** (2001), p. 250.

[6] R. D. Diehl, R. McGrath, *Surf. Sci. Rep.* **23** (1996), p. 43.

[7] A. Fedorus, D. Kolthoff, V. Koval, I. Lyuksyutov, A. G. Naumovets, H. Pfnür, *Phys. Rev. B* **62** (2000), p. 2852.

[8] A. Kiejna, R. M. Nieminen, *Phys. Rev. B* **66** (2002), p. 085407.

[9] A. Kiejna and R. M. Nieminen, *Phys. Rev. B* **66** (2002), p. 085407.

[10] U. Martinez, L. Giordano, G. Pacchioni, *J. Chem. Phys.* **128** (2008), p. 164707.

[11] J. Hoelz and F. K. Schulte, *Work function of metals* (Springer, Berlin, 1979).

CHAPTER 11

Consequences of doping: induced charging[†]

The data presented on this final chapter are the results of the knowledge accumulated in the course ot the thesis. In the first part of the thesis (Chapter 3 and 4) it has been reported the possibility of charging gold atoms and iron clusters deposited on ultra–thin MgO films. The occurrence of this charge transfer is related to several factors like the high electron affinity of the adsorbed species, the modification of the metal work function induced by the oxide film, the penetration of the tails of the metal support into the insulating oxide layer, and the occurrence of a polaronic distortion in the film.

Charging and stabilization of adparticles do not occur spontaneously on every oxide film. As described in Chapter 5 and 6, Au atoms deposited on SiO_2/Mo(112) films remain neutral and are unable to bind to defect–free oxide patches. Charge transfer is prevented in this case by the negative surface dipole associated with the silica growth, which raises Φ and acts against an electron flow into gold (see also Section 1.3.3). Indeed in Chapter 9 we discussed the possibility to tune in a suitable way Φ by doping the system with electropositive species, e.g., alkali atoms. In particular the incorporations of Li atoms and the consequent change in the work

[†]The results described in this Chapter have been reported in: *U. Martinez*, J. Jerratsch, N. Nilius, L. Giordano, G. Pacchioni, H.-J. Freund, *Physical Review Letter* **103** 056801 (2009) and *U. Martinez*, L. Giordano and G. Pacchioni, *ChemPhysChem* Accepted

funtion of the system has been proven also experimetally, as reported in the Chapter 10. Finally in this chapter a joint theoretical–experimental study demonstrates that a Li–doped SiO_2/Mo(112) film is indeed able to anchor and charge Au atoms and particles even when no surface defects are present.

11.1 Computational and Experimental Details

Computational Details

The calculations has been performed with the VASP code (see section 2.1.1, page 25). The kinetic energy cutoff has been set to 400 eV. A vacuum of at least 10 Å separates the slabs and a dipole correction has been applied. The atoms within the supercell are relaxed until the atomic forces are less than 0.01 eV/Å. The Mo(112) metal substrate has been modeled by seven metal layers. Supercells of various sizes are constructed to model the interaction of Li and Au with the SiO_2/Mo(112) film. The largest (6×4) cell had hereby a composition of $Mo_{96}Si_{24}O_{60}$. The Li coverage, has been defined with respect to the Li atoms per silica ring. Therefore, a coverage θ=1 corresponds to a Li atom per pore or one Li each two Si atoms. The work function of metal and metal/oxide surfaces has been defined as the energy of the vacuum level (determined as the self–consistent potential in the vacuum) with respect to the Fermi level of the metal or of the metal/oxide interface. film. STM images are simulated using the Tersoff-Hamann approach.[1]

Experimental Details

The experiments are performed with a custom–build ultrahigh vacuum STM operated at 10 K. Electronic properties of the sample are detected with differential conductance (dI/dV) spectroscopy, providing a measure for the local density of states (LDOS). The silica film is prepared by depositing 1.2 monolayer Si in 1×10^{-7} mbar O_2 onto an oxygen precovered Mo(112) surface and annealing the sample to 1200 K. The Li atoms are introduced from a commercial Li dispenser at 100 K, while Au is deposited at 20 K from a gold–plated tungsten filament.

11.2 Results and Discussion

11.2.1 Theoretical prediction

Au atom adsorption on "clean" and Li–doped SiO_2/Mo(112)

Au atoms interact very weakly, mainly through dispersion forces, with the regular silica surface, with binding energies of the order of 0.1 eV. Only in the presence of point defects like silicon and oxygen dangling bonds[2] or substitutional impurities like a Ti atom[3] the film shows a pronounced chemical activity and binds gold atoms strongly. On the regular, defect free film the weak interaction of the gold atoms results also in a rapid diffusion and aggregation, with formation of gold nanoparticles in correspondence of line defects where eight–member rings, which can accomodate Au atoms and even very small Au clusters, are present (see Chapter 5 and 6).

When the Au atoms are deposited on a Li–doped SiO_2/Mo(112) film a completely different situation is found. At high Li coverage, θ=1, three possible adsorption sites have been identified: (1) the Au atom is adsorbed at the center of the ring, directly above the Li atom at a distance of 4.23 Å; (2) the Au atom is on–top of a bridging O atom protruding outside the surface; (3) the Au atom is on–top of a bridging O atom lying at the same height as the Si atoms of the film, Figure 11.1. In (1) the bonding for Au is weak, 0.34 eV, and a partial charge transfer, as measured by the Bader charge ($-0.55\ e$), occurs (the atom is still spin polarized). In position (2) the atom is also very weakly bound, 0.18 eV, and almost neutral, as shown by the Bader charge ($-0.26\ e$) and by the fact that the solution is spin polarized. However, when Au is in position (3) it becomes strongly bound, 1.33 eV, the ground state is non–magnetic, and the atom is negatively charged (Bader charge $-0.80\ e$). This latter state is thus a global minimum. When one starts the optimization from other starting points near this bridging O atom, e.g. on–top of a Si atom, one finds this structure. The occurrence of the charge transfer is further demonstrated by the PDOS curves where the $6s$ level is doubly occupied and well below the Fermi level, Figure 11.2b. No change occurs in the position of the Li atoms at the interface upon Au adsorption.

It is important to analyze the reasons for the occurrence of the charge transfer only in some specific adsorption sites and not on everywhere. This is connected to the strong polaronic distortion which helps to stabilize the charged state of the Au^- anion. In particular, in the preferred adsorption site, Figure 11.1 site (3), the O atom of the top layer relaxes downwards in direction of the Mo surface by about

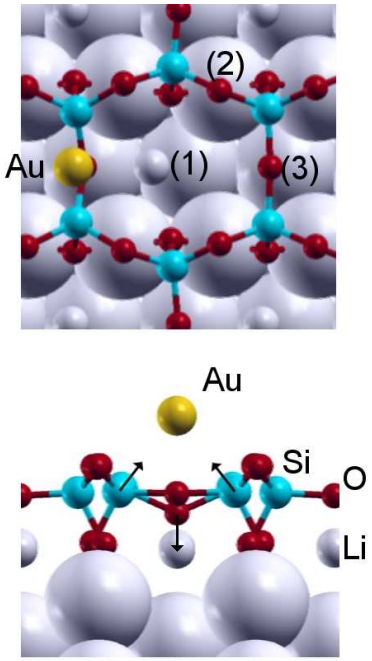

Figure 11.1: (Above) Structure model showing potential Au adsorption sites on SiO_2/Mo(112) doped with one Li^+ per pore: (1) above a nanopore filled with an interfacial Li atom, (2) on a Si–O–Si bridge on top of a Mo row, and (3) on the O atom of a $\bar{1}10$–oriented Si–O–Si bridge that suspends two Mo rows. (Below) Schematic representation of the polaronic distortion around the adsorbed Au atom on site (3).

0.85 Å, while the two adjacent Si atoms move towards the Au anion by about 0.1 Å, Figure 11.1. This relaxation strongly stabilizes the $6s$ level of Au, which becomes doubly occupied with formation of Au^-. In absence of the polaronic distortion, the charge transfer does not take place, showing that the change in work function alone is not sufficient to promote charge transfer.

To emphasize the importance of the polaronic distortion, we have considered Au atom adsorption on the non–doped SiO_2/Mo(112) film. We mentioned already that on this system Au forms a very weak bond and remains neutral, Figure 11.3a; of course, the surface is unperturbed by Au adsorption. However, if we start the geometry optimization from a distorted silica structure as found in Li/SiO_2/Mo(112), we obtain a local minimum with the same characteristics, Figure 11.3b: the Au atom

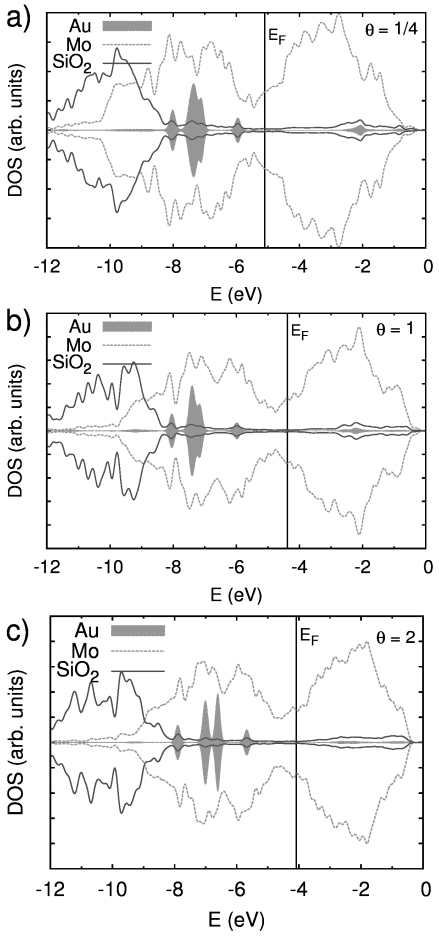

Figure 11.2: DOS curves for a Au atom adsorbed on $Li/SiO_2/Mo(112)$ at different Li coverages.

is charged (as shown by the PDOS plots, Figure 11.3b) but is slightly less stable (by about 0.1 eV) than neutral gold on the undistorted film. The two mimima are separated by a barrier, which is expected to be rather high given the cost to distort the silica structure (2.95 eV, computed as the difference in total energies between undistorted and distorted $SiO_2/Mo(112)$ film). The Au atom is then bound by 2.90 eV to this "distorted" structure, so that the final result is a slightly unbound system. This distortion is closely connected to the existence of a single oxide layer supported on

a metal, which allows atomic displacements that occur at much lower cost than in a normal oxide. Calculations performed on a silica bilayer structure show in fact that the addition of a Au^- anion results in two structures, one, more stable, where Au^- is weakly bound on–top of a Si atom and the silica network is almost undistorted, and second one which exhibits the same kind of lattice distortion observed on the SiO_2/Mo(112) films but which is much higher in energy.

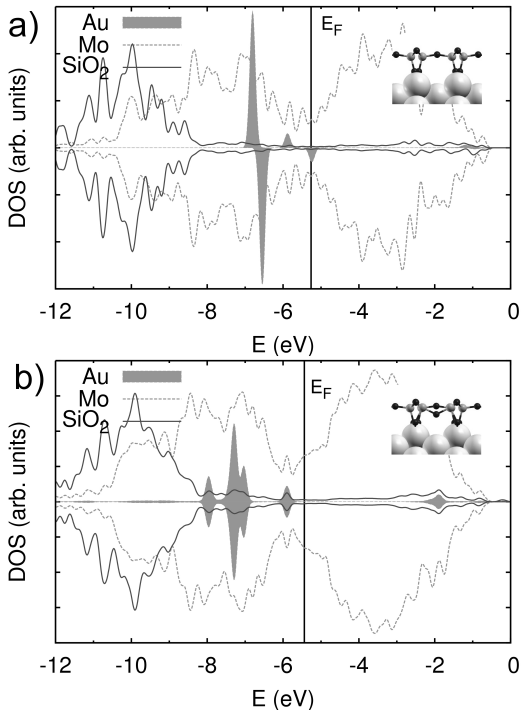

Figure 11.3: Effect of the polaronic distortion on the electronic structure of a supported Au atom. (a) DOS curves of a neutral Au atom adsorbed on an undistorted and undoped SiO_2/Mo(112) film; (b) DOS curves of a negatively charged Au atom adsorbed on a distorted and undoped SiO_2/Mo(112) film. Structure (b) is less stable by 0.1 eV.

The next question is whether the observed spontaneous charge transfer from Mo to supported Au occurs only for high Li–doping or can be found also at lower Li coverages. To this end, we have studied Au atom deposition on Li–doped SiO_2/Mo(112) for θ(Li)=2.0, 1.0, 0.75, 0.5, and 0.25. We also considered to what extent the occurrence of spontaneous charging depends on the distance of adsorbed Au from the in-

terface Li atom by performing two calculations for the same Li coverage, one where Au is near Li, and one where Au is far from Li.

Some clear trends emerge (Table 11.1): (i) the stability of the adsorbed Au^- anion is larger when the Li coverage is larger; the binding energy goes from 1.78 eV for θ(Li)=2.0 to < 0.5 eV for θ(Li)=0.25; (ii) for a fixed Li coverage the stability of Au^- is larger when the distance from the Li cations is shorter; (iii) for θ(Li)$\geq$0.5 the formation of the polaronic distortion occurs spontaneously (no barrier); (iv) for θ(Li)=0.25 the polaronic distortion is found only by starting from an ad–hoc distorted structure, which indicates the presence of a (probably small) barrier. In absence of this ad–hoc distortion, the calculations converge to a weakly bound neutral Au atom. This solution, however, is always higher in energy than the charge transfer state. Stated differently, at low Li coverage the polaronic distortion is a thermally activated process while at high Li coverage the polaron forms spontaneously.

Table 11.1: Properties of adsorbed Au atom on Li–SiO_2/Mo(112) as a function of Li coverage.

θ(Li)		E_{ad} (eV)	Bader charge (e)	r(Au–O) (Å)	r(Au–Si) (Å)	Δz(O) (Å)	$\varepsilon(6s)^a$ (eV)
0.25	near	0.48	−0.80	2.79	2.58	−0.84	−5.95
	far	0.11	−0.78	2.79	2.59	−0.89	−5.82
0.50	–	1.03	−0.81	2.81	2.57	−0.89	−5.99
0.75	–	1.21	−0.80	2.80	2.58	−0.87	−6.00
1.0	–	1.33	−0.80	2.77	2.59	−0.85	−5.97
2.0	–	1.78	−0.84	2.91	2.41	−0.25	−5.68

[a] The zero of energy correspond to the position of the vacuum level.

This discussion shows that the change in stability of anionic gold is a function of two major terms: the polaronic distortion of the oxide surface, and the position of the Fermi level of the Mo metal compared to the position of the Au 6s state. Going from θ(Li)=0.25 to θ(Li)=2.0, the position of the doubly occupied 6s level of the Au anion remains constant, about 6 eV below the vacuum level, Figure 11.2 and Table 11.1; the position of the Au 6s level is largely determined by the polaronic distortion which stabilizes it and lowers it in energy. This contribution is independent of Li coverage. On the other hand, the position of the Mo Fermi level depends on the Li coverage and is shifted to higher energies (lower work function) for higher Li coverage, Figure 11.2.

Au_2 adsorption on $Li/SiO_2/Mo(112)$

We move now to the adsorption of a gold dimer on Li–doped $SiO_2/Mo(112)$. The calculations are for the case θ(Li)=1.0. On the "clean" surface, the dimer interacts weakly and remains neutral. The question is wheather the bonding changes on the doped surface or not. Three different orientations have been found, one parallel to the surface, one perpendicular and a third with one Au atom on–top of a bridging O atom and the second Au atom protruding outside the surface, Table 11.2 and Figure 11.4. The three minima differ only slightly in geometry and in binding energy and the electronic structure is almost the same. Because of the closed shell nature of Au_2, the dimer remains neutral also on the Li–doped silica film. The Bader analysis does not show any extra charge on Au_2, Table 11.2, and the PDOS curves confirm that the cluster is neutral with the σ^* state above the Fermi level, Figure 11.5. Given the absence of charge transfer, it is not surprising that the bonding is weak and ranges from 0.12 to 0.36 eV, depending on the isomer, with no polaronic distortion of the substrate.

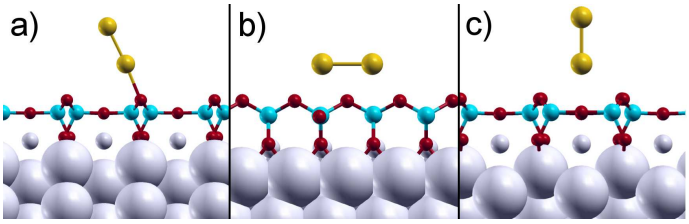

Figure 11.4: Structures of Au_2 isomers adsorbed on $Li/SiO_2/Mo(112)$ films. In all three cases the molecule remains neutral and weakly bound.

Table 11.2: Properties of adsorbed Au_2 on $Li/SiO_2/Mo(112)$.

Isomer	E_{ad} (eV)	Bader charge (e)	r(Au–Au)[a] (Å)
Figure 11.4a	0.36	−0.03	2.51
Figure 11.4b	0.14	−0.07	2.54
Figure 11.4c	0.12	−0.03	2.53

[a] r(Au–Au) in gas–phase Au_2 and Au_2^- is 2.54 and 2.69 Å, respectively

The situation is reminiscent of that of a Au_2 unit adsorbed on MgO/Ag(100)

ultrathin films.[4] Here too it has been observed that Au atoms become negatively charged, Au^- (see Chapter 3). The dimer, however, exhibits a different character. Two isomers have been identified, one normal to the surface, neutral, and one lying flat on the surface, charged and paramagnetic (Au_2^-). The vertical neutral dimer is slightly more stable according to DFT calculations, but STM experiments performed at very low temperature (<10 K) have been able to identify the co–existence of the two isomers. On the Li–doped silica films it seems that charged dimers do not form or, if they form, they correspond to metastable states.

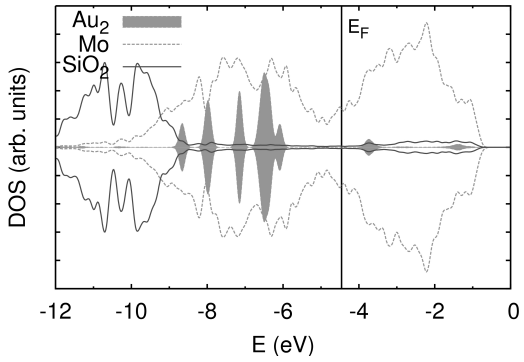

Figure 11.5: DOS curve for a gold dimer adsorbed on $Li/SiO_2/Mo(112)$ (most stable configuration).

The tendency of Au_2 to remain neutral is due to the closed shell nature of the system, and to the fact that the additional electron will occupy an anti–bonding state, with consequent weakening of the Au–Au bond. Only if the cost for this loss of bonding is compensated by other bonding mechanisms like a local distortion of the surface or by the interaction with an exposed cation of the oxide film a negatively charged gold dimer can be stabilized. Apparently, on $Li/SiO_2/Mo(112)$ this is not the case.

Au_n adsorption on $Li/SiO_2/Mo(112)$

We have considered the adsorption of Au_3 and Au_5 clusters on the clean and Li–doped $SiO_2/Mo(112)$ surfaces. On the undoped $SiO_2/Mo(112)$ films the result is that expected by other studies: Au_3 remains neutral and spin polarized (doublet ground state), is bent as in the gas–phase (156° on the surface, 146° in gas–phase),

and very weakly weakly bound, Figure 11.6a. This confirms the results obtained for Au atom and dimer and further shows the inert character of the undoped surface.

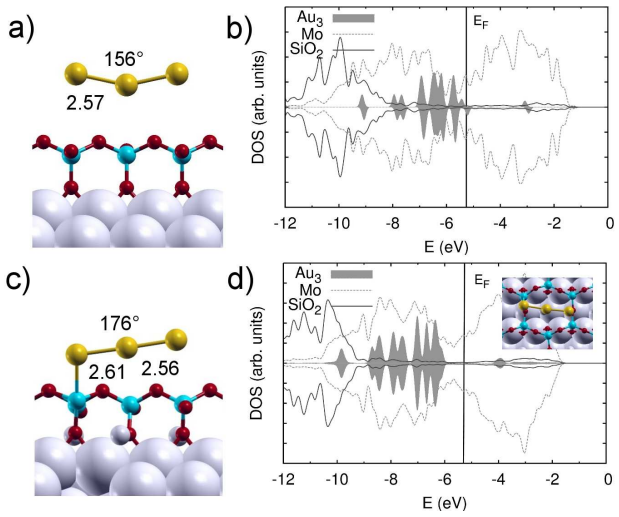

Figure 11.6: (a) Structure of Au_3 cluster adsorbed on SiO_2/Mo(112). The cluster remains neutral. E_{ad}=0.01 eV, magnetization =0.68 e, Bader charges $-0.11/-0.01/-0.11$ e; (b) DOS curves; (c) Structure of Au_3 cluster adsorbed on Li/SiO_2/Mo(112), θ(Li)=1.0. The cluster becomes charged. E_{ad}=1.23 eV, magnetization =0.0 e, Bader charges $-0.49/-0.02/-0.24$ e; (d) DOS curves.

On Li–doped SiO_2/Mo(112) (for θ(Li)=1.0), adsorbed Au_3 has a completely different nature. Two orientations of the Au_3 cluster have been considered, one nearly parallel to the surface with the central Au atom above the center of the ring and the other two Au atoms nearly on–top of bridging O atoms, see inset of Figure 11.6b, and a second one where Au_3 has all the three atoms above bridging oxygens of the silica surface. This latter structure is less stable and, after geometry optimization, the cluster axis is significantly bent with respect to the surface plane. On both orientations, the cluster is linear, i.e. it assumes the same structure of Au_3^- in gas–phase, and the bonding is strong, >1 eV. This is due to a net charging of the cluster, as shown by the PDOS curves and by the absence of magnetization, Figure 11.6d. The Au–Au distances, between 2.55 and 2.64 Å, are similar as in gas–phase Au_3^-. The surface undergoes a strong polaronic distortion similar to that described above for a Au atom, an effect which considerably contributes to stabilize the negatively

charged gold cluster.

The structure of Au_5 has been obtained from that of Au_3 by adding two Au atoms to the linear structure shown in Figure 11.6c and reoptimizing the geometry. In the final structure, Figure 11.7, Au_5 assumes a symmetric configuration with two Au atoms anchored to the surface and a triangular Au_3 unit which points out of the surface. The whole Au_5 structure is planar and the cluster plane is tilted by about 53° with respect to the surface normal, Figure 11.7. As for the Au atom and trimer, the silica film is distorted in correspondence of the Au adatoms. Au_5 is bound by 0.58 eV with respect to the best gas–phase Au_5 isomer, a planar trapezium formed by condensing three equilateral triangles.[5] The Bader analysis shows a charge of $-0.26\ e$ on each of the two anchoring Au atoms, and a smaller charge on the Au apical atom, Figure 11.7. The DOS curves confirm the diamagnetic nature of adsorbed Au_5, which is consistent with the occurrence of a charge transfer from the Li–doped silica film.

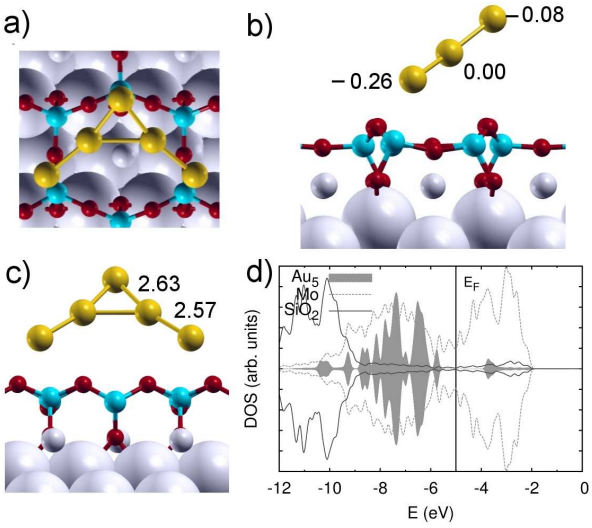

Figure 11.7: (a–c) Structure of Au_5 cluster adsorbed on $Li/SiO_2/Mo(112)$, θ(Li)=1.0. The cluster becomes charged. E_{ad}=0.58 eV with respect to the most stable gas–phase Au_5 isomer; magnetization = 0.0 e; Bader charges and selected distances are shown in (b) and (c), respectively. DOS curves are shown in (d).

11.2.2 Experimental observation

The theoretical prediction described in the previous Section has been also verified experimentally. The Li doping induces a dramatic change in the adsorption behavior of the silica/Mo film with respect to gold, as shown in Figure 11.8. Prior to Li incorporation, Au atoms are unable to bind to the defect–free film and rapidly diffuse on the surface until they become trapped at domain boundaries between two oxide patches (Figure 11.8a and see also Chapters 5 and 6). Along these line defects, the six–membered –Si–O– rings are replaced by eight–membered entities, whose diameter is sufficiently large to accommodate the Au. Those defect–bonded adatoms serve as nuclei for the growth of three–dimensional (3D) particles, decorating the domain boundaries, Figure 11.8a. This adsorption behavior completely changes after Li doping, when Au atoms and clusters also appear on the defect–free oxide terraces away from the domain boundaries, Figure 11.8b. At low Au exposure, mainly single adatoms with spherical shape and $\sim$0.8 Å height are detected, Figure 11.8c. The absence of starlike shapes in this case, being the fingerprint for an embedded species as demonstrated for Li and Pd (Chapters 5 and 10), suggests an Au atom location above the oxide surface. This conclusion is supported by the fact that single adatoms are found on top of the –Si–O– network and not above the nanopores. In most cases, the Au atoms and clusters attach to the Li–rich stripes with their lower work function, but occasionally bind to Li–poor regions as well, Figure 11.8b. With increasing Au coverage, 3D particles develop on the modified surface with an average density of 2.5×10^{12} cm^2. The deposits adopt mainly prolate shapes with a large height to diameter ratio of $\sim$0.3, but sometimes exhibit triangular and hexagonal base planes, Figures 11.8e and 11.8f. Whereas Au monomers do not show conductance peaks that would indicate tunneling into defined atomic orbitals, a number of dI/dV maxima are revealed for larger particles, suggesting the formation of quantum well states in the confined electronic system.

11.3 Summary

In this Chapter it was shown by a combined theoretical–experimental approach that the adsorption properties of silica/Mo(112) thin films can be tailored by modifying the work function of the system via doping. The work function decrease associated with the doping renders the silica film reactive and enables the stabilization of Au atoms and clusters on the originally inert oxide surface. The underlying adsorp-

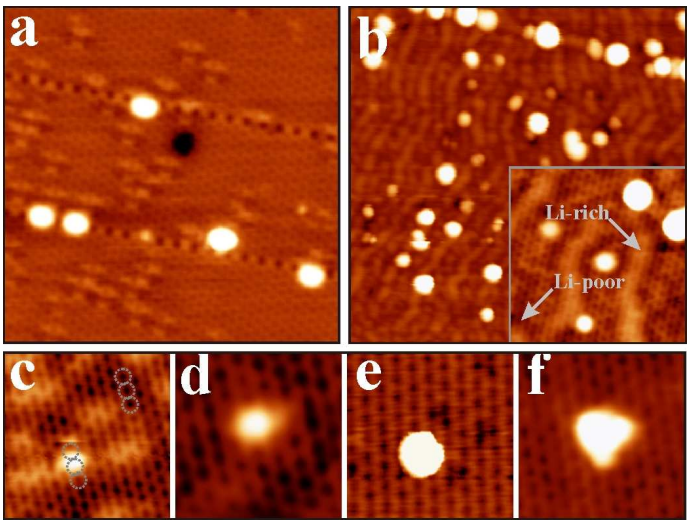

Figure 11.8: (a) Pristine (2.0 V, 20×20 nm^2) and (b) Li–doped silica film after deposition of 0.1 monolayer Au (2.0 V, 50×50 nm^2). Whereas Au attaches exclusively to domain boundaries for the undoped film, it binds to defect–free oxide patches after incorporation of 0.7 Li^+ ions per silica pore. The inset in (b) shows an oxide region with enhanced resolution (0.6 V, 11×11 nm^2). (c) Single Au atom on Li–doped silica. The adatom does not sit above a pore, but between two hexagonal rings as marked by the dashed circles. (d)–(f) Au clusters with increasing size stabilized on Li–doped silica. The Au growth follows the Vollmer–Weber regime and leads to the formation of 3D particles.

tion mechanism is related to a charge transfer from the Mo metal into the Au atoms, which initiates a polaronic distortion of the oxide lattice. The strongly bound Au^- species constitute the seeds for further cluster growth. This study demonstrates the possibility to anchor adsorbates on oxide thin films by controlling their charge state. While the present results are referred to silica films, the procedure might be applied to other oxide materials, providing a general method to design the properties of metal–oxide interfaces.

Bibliography

[1] J. Tersoff, D. R. Hamann, *Phys. Rev. Lett.* **50** (1983), p. 1998.

[2] U. Martinez, L. Giordano, G. Pacchioni, *J. Phys. Chem. B* **110** (2006), p. 17015.

[3] L. Giordano, A. Del Vitto, G. Pacchioni, *J. Chem. Phys.* **124** (2006), p. 034701.

[4] V. Simic–Milosevic, M. Heyde, N. Nilius, T. König, H.–P. Rust, M. Sterrer, T. Risse, H.–J. Freund, L. Giordano, G. Pacchioni, *J. Am. CHem. Soc.* **130** (2008), p. 7814.

[5] B. Assadollahzadeh, P. Schwerdtfeger, *J. Chem. Phys.* **131** (2009), p. 604306.

CHAPTER 12

Summary

When the thickness of an oxide film is below a nm (few atomic layers) the interaction with the metal substrate, together with structural and morphology changes, can lead to completely different chemistry with respect to thicker films and can lead to new and unprecedented phenomena. This thesis focuses on the study of the structure and properties of different ultrathin oxide films epitaxially grown on metal substrates and their interactions with adsorbed metal atoms and clusters. The study has been done in close collaboration with the experimental group of Prof. H. Freund at the Fritz–Haber–Institut in Berlin where metal atoms and clusters are generated, deposited on oxide surfaces, and characterized with various spectroscopic techniques.

In the first part of this thesis the possibility to control the charge state of metal atoms deposited on ultrathin MgO films is described. In particular, gold atoms or clusters deposited on 2–3 layers thick MgO films on Ag(100) and Mo(100) become negatively charged. The study of different observable properties has been possible to prove the anionic nature of gold adsorbates. The charge transfer from the substrate to the adsorbate is a very important effect which has dramatic consequences on the structure and shape of the supported clusters which form two-dimensional structures while on thicker films they form three–dimensional particles. It may be expected that the change in shape and in electronic nature will also result in a differ-

ent chemical reactivity, as recently suggested by DFT calculations. In collaboration with Professor F. Illas of the Universitat de Barcelona it has been also demonstrated the possibility to tune the magnetic properties of iron nanoclusters deposited on MgO/Fe(100) films through a charge transfer mechanism of a single spin component.

The second part of this work has been devoted to the study of ultrathin silica films on Mo(112) which show completely different characteristics with respect to MgO films. Due to the particular crystalline structure these films can be viewed as a first example of a two-dimensional molecular sieve, which could be used to selectively permit diffusion of metal atoms or small molecules to the metal substrate. On the SiO_2/Mo(112) thin films Au, Pd and Ag atoms exhibit very different behavior. Due to the weak interaction and to the easy diffusion, Au atoms aggregate to form nanoparticles already at low temperature along line defects. Pd interacts more strongly than Au with the Si or O atoms of the film and can easily penetrate into the film and become bound at the SiO_2/Mo interface directly in contact to the Mo metal. Ag atoms exhibit a similar behavior to Pd atoms but the activation energy for penetration is higher. The calculations supported by the experimental finding of the group in Berlin explain in detail the interaction mechanism that enables a reliable prediction of the penetration barriers for other atomic and molecular species. Analyzing Pd and Au atoms deposited on a second phase of the SiO_2/Mo(112) film (with an additional O–layer on the Mo surface) it has been possible to demonstrate the importance of structural details in determining the adsorption properties. In this case a combined theoretical and experimental study has been done by STM, infrared reflection adsorption spectroscopy, and CO adsorption. Moreover, it has been demonstrated that Pd atoms incorporated into the nanopores of the silica film are able to anchor various adatoms at the originally inert oxide surface showing the possibility to modify the local properties of the surface.

A significant effort has been done in the last part of the thesis trying to find a way to functionalize and to modify the global properties of silica films. In this context a well known procedure has been applied to tune the work function of a metal surface by deposing alkali atoms on ultrathin oxide films. DFT calculations clearly show that once that an alkali atom is deposited on oxide ultrathin films the charge transfer from the alkali atom to the substrate creates a dipole moment that lowers the work function of the system. The change in work function induced can be used to modify in a very efficent way the electronic properties of the oxide film. In fact, by spontaneous diffusion of the alkali atom into the pores of the silica film structure

[as experimentally demonstrated for the case of Li on SiO_2/Mo(112)], one obtains a stable assembly of incorporated alkali metal cations. The Li–doped silica system can be finally used to stabilize and activate Au atoms and clusters on the originally inert oxide surface. In particular, the adsorption mechanism is related to the charge transfer from the Mo metal into the Au atoms, which induces a polaronic distortion of the oxide lattice. The strongly bound Au^- species constitute the seed for further cluster growth. The experimental work of the group at the FHI clearly demonstrates these finding by means of scanning tunneling microscopy and scanning tunneling spectroscopy providing the final proof for a general method to design the properties of metal–oxide interface.

Finally, in collaborations with Professor Shluger at the University College London, we studied the different stabilities of color centers (oxygen vacancies) in MgO ultrathin films showing that also in this case, when particular conditions are fulfilled, a charge transfer mechanism from the metal substrate directly into the defect is possible.

Publications

1. J. Jerratsch, N. Nilius, H.-J. Freund, U. Martinez, L. Giordano, G. Pacchioni, H.-J. Freund *"Fabricating arrays of single iron atoms in a porous silica/Mo(112) film"*, Submitted;

2. J. Jerratsch, N. Nilius, D. Topwal, U. Martinez, L. Giordano, G. Pacchioni, *"Lithium incorporation into a silica thin film: Scanning tunneling microscopy and density functional theory"*, Submitted;

3. U. Martinez, L. Giordano and G. Pacchioni *"Mechanism of charging of Au atoms and nanoclusters on Li doped SiO_2/Mo(112) films"*, *ChemPhysChem* Accepted;

4. U. Martinez, G. Pacchioni *"Interaction of CO, CO_2 and CH_4 with periodic mesoporous organosilica: DFT calculations with dispersion corrections"*, *Microporous and Mesoporous Materials* in press.;

5. U. Martinez, J. Jerratsch, N. Nilius, L. Giordano, G. Pacchioni, H.-J. Freund *"Modifying the adsorption properties of silica thin films via work function control"*, *Physical Review Letter* **103** 056801 (2009);

6. U. Martinez, G. Pacchioni, F. Illas *"Enhanced magnetic moments of Fe clusters supported on MgO/Fe(001) ultrathin films"*, *The Journal of Chemical Physics* **130** 184711 (2009);

7. S. Ulrich, N. Nilius, H-J Freund, U. Martinez, L. Giordano, G. Pacchioni *"Realization of an atomic sieve: Silica on Mo(112)"*, *Surface Science* **603** 1145 (2009);

8. S. Ulrich, N. Nilius, H-J Freund, U. Martinez, L. Giordano and G. Pacchioni *"Modifying the Adsorption Characteristic of Inert Silica Films by Inserting Anchoring Sites"*, *Physical Review Letter* **102** 016102 (2009);

9. U. Martinez, L. Giordano and G. Pacchioni *"Tuning the work function of ultrathin oxide films on metals by adsorption of alkali atoms"*, *The Journal of Chemical Physics* **128** 164707 (2008);

10. S. Ulrich, N. Nilius, H-J Freund, U. Martinez, L. Giordano and G. Pacchioni *"Evidence for a size–selective adsorption mechanism on oxide surfaces: Pd and Au atoms on SiO_2/Mo(112)"*, *ChemPhysChem* **92** 1367 (2008);

11. S. Prada, U. Martinez, G. Pacchioni *"Work function changes induced by deposition of ultrathin dielectric films on metals: A theoretical analysis"*, *Physical Review B* **78** 235423 (2008);

12. L. Giordano, U. Martinez, G. Pacchioni, M. Watkins and A.L. Shluger *"F and F^+ Centers on MgO/Ag(100) or MgO/Mo(100) Ultrathin Films: Are They Stable?"*, *J. Phys. Chem. C* **112** 3857 (2008);

13. M. Baron, D. Stacchiola, S. Ulrich, N. Nilius, S. Shaikhutdinov, H.-J. Freund, U. Martinez, L. Giordano and G. Pacchioni *"Adsorption of Au and Pd Atoms on Thin SiO_2 Films: the Role of Atomic Structure"*, *J. Phys. Chem. C* **112** 3405 (2008);

14. L. Giordano, U. Martinez, S. Sicolo, G. Pacchioni, *"Observable consequences of formation of Au anions from deposition of Au atoms on ultra-thin oxide films"*, *J. Chem. Phys.* **127** 144713 (2007);

15. M. Sterrer, T. Risse, U. Martinez, L. Giordano, M. Heyde, H-P Rust, G. Pacchioni and H-J Freund *"Control of the charge state of metal atoms on thin MgO films"*, *Physical Review Letter* **98** 096107 (2007);